Norwegian University of
Science and Technology

Atomic force microscopy and variable angle spectroscopic ellipsometry of oxidising GaAs substrates for intermediate band solar cells

Anne Holst-Dyrnes

Master of Science in Physics and Mathematics
Submission date: June 2018
Supervisor: Turid Worren Reenaas, IFY
Co-supervisor: Thomas Brakstad, IFY

Norwegian University of Science and Technology
Department of Physics

Preface

This Master's Thesis was carried out as a part of the Master of Science degree in Applied Physics and Mathematics at the Norwegian University of Science and Technology (NTNU) during the spring semester of 2018. The thesis is a continuation of my Specialization Project in Physics (TFY4510) at NTNU, as presented in my report titled "Surface characterization of GaAs substrates". This thesis was written at the Department of Physics in Trondheim, Norway.

First, I'd like to thank my supervisor, Associate Professor Turid Reenaas at the Department of Physics, for her help and guidance during my work with this thesis. A thesis such as this one, which relies heavily on experimental work, is unpredictable in nature, and Turid has guided me steadily through unforeseen changes and hurdles during this semester.
I'd also like to thank my co-supervisor, Thomas Brakstad, who has been in charge of doing the ellipsometry measurements for this work. He has guided me steadily through the ellipsometry modelling and theory, and answered any questions I might have quickly and clearly.
A thanks also to Dr. Mohana Rajpalke, for preparing samples for the work, for participating in a few of the experiments, and giving me helpful tips and suggestions for using AFM.

I would also like to thank Kvilebu Crew, for lunch, for help, for tips, and for support.

Finally, I would like to thank my family; mum, dad, Linn, Tigergutt, and Jon, for supporting me through my years at NTNU and abroad. I did not force them to proofread this thesis, although I am sure they would have, had I asked.

Anne Holst-Dyrnes
Trondheim, Norway
June 2018

Abstract

Intermediate band solar cells (IBSCs) have a theoretical potential of being 50% more efficient than the single band gap first generation solar cells. One way of determining which material compositions and solar cell structures that will produce the most efficient IBSC is to perform simulations of various solar cell structures to test their performance. For this, knowledge of the opto-eletronic material properties of each layer of the solar cell is needed. Variable angle spectroscopic ellipsometry (VASE) is a suitable characterization technique for determining optical properties of layered structures. VASE does, however, have some limitations, and provides more accurate results if it has input on i.e. layer thicknesses and surface roughness from other characterization techniques. Atomic force microscopy (AFM) is a suitable complimentary technique for determining surface roughness. This thesis is a continuation of previous work done by me on GaAs substrate characterization. The focus of this thesis has been to study the GaAs surface as it oxidises, with emphasis on surface roughness and native oxide thickness.

In this study, two GaAs substrates had their native oxides removed by thermal desorption, and were then re-oxidised by exposing the samples to air. One of the samples, the "buffer sample", had a 300 nm GaAs buffer layer grown by MBE on the surface before being exposed to air, while the other sample, the "substrate sample", received no treatment beyond the removal of the oxide before being exposed to air. Both samples were then studied regularly with atomic force microscopy and variable angle spectroscopic ellipsometry, and the buffer sample was also studied with optical profilometry. The goal for the experiments was to determine how the surface roughness and native oxide layer thickness evolves over time, and use this to develop a good optical model for a GaAs sample with native oxide and surface roughness.

The AFM images of the substrate sample revealed approximately $4.5 \cdot 10^8$ pits/cm^2 on the sample surface, and the pits were several tens of nanometers deep. The imaged geometry of the pits on the surface seemed to be affected by the geometry of the AFM probe tip, indicating that the probe was unable to detect the true depth and shape of the pits. The AFM obtained surface roughness could therefore be an underestimation of the true value. The roughness varied between 1.3-2.0 nm in the 15 weeks after exposing the sample to air. Due to the large variation of the roughness measurements, as well as unexpected drift and distortion of the images, the AFM results were deemed unreliable, and are to be considered rough estimates. From the VASE measurements, several optical models were built and fitted to the measurements, in order to find the model with the best fit, and from that model obtain the oxide layer thickness. Ideally, the AFM results would have be used as input for the VASE model to make the model more accurate. However, due to the uncertainty of the AFM results, they were not used as input for the VASE model, and no precise estimation of the oxide layer thickness was obtained. The oxide layer is believed to be at least 1 nm thick after 12 weeks of exposing the sample to air.

The AFM images of the buffer sample showed a very smooth surface, with a terrace structure. The height difference between neighbouring terraces was on average approximately 0.28 nm, which is half the lattice constant for GaAs. These terraces likely stem from GaAs forming in layers of half unit cells, probably during growth of the buffer layer. The surface roughness for the buffer sample was measured by AFM to be around 0.35 nm in the first few days after exposure to air. The roughness then decreased to around 0.30 nm in the following weeks. The surface roughness was measured with optical profilometry to be 0.36-0.39 nm, 9 weeks after

exposure to air. From the VASE measurements, several optical models were built and fitted to the measurements, in order to find the model with the best fit, and from that model obtain the native oxide layer thickness. Supplementing the VASE model with the AFM results, the oxide layer thickness was estimated to be around 0.8 nm after one hour of exposure to air, 1.9 nm after 2 weeks, and 2.2 nm after 4 weeks.

Sammendrag

Mellombåndsolceller har en teoretisk potensiell virkningsgrad som er 50% høyrere enn den øvre teoretiske grensen for dagens kommersielle solceller. De beste materialsammensetningene og strukturene for gode mellombåndsolceller har enda ikke blitt funnet, og en måte å finne frem til de mest lovende mellombåndsolcellene er å gjøre simuleringer av ulike strukturer for å se hvordan de ulike sammensetningene påvirker solcellens ytelse. For å kunne gjøre simuleringer av solceller trenger man kunnskap om de optoelektroniske materialegenskapene for hvert lag av solcellen. Spektroskopisk ellipsometri (SE) er en passende karakteriseringsteknikk for å bestemme de optiske egenskapene til lagvise strukturer. Ellipsometri har imidlertid noen begrensninger, og det er dermed hensiktsmessig å supplementere ellipsometrimålingene med informasjon om eksempelvis overflateruhet eller tykkelser på materiallag fra andre karakteriseringsteknikker. Atomær kraft-mikroskopi (AFM) er en passende komplementær teknikk til ellipsometri for å finne overflateruhet. Denne oppgaven er en fortsettelse av tidligere arbeid gjort av meg på GaAs-substrater. Fokuset i denne oppgaven har vært på overflaten av GaAs-substrater, med vekt på overflateruhet og oksidtykkelse.

I denne masteroppgaven har to GaAs-substrater fått sine oksidlag fjernet ved termisk desorpsjon, og deretter blitt re-oksidert ved å eksponere prøvene for luft. En av prøvene, ”bufferprøven”, fikk et 300 nm bufferlag av GaAs grodd med MBE på overflaten før den ble eksponert for luft. Den andre prøven, ”substratprøven”, ble ikke videre behandlet etter at oksidlaget var fjernet, og prøven ble eksponert for luft. Det ble gjort regelmessige målinger med AFM og SE på begge prøvene, og det ble også gjort målinger med optisk profilometri på bufferprøven. Målet med oppgaven var å bestemme hvordan overflateruheten og tykkelsen på oksidlaget utviklet seg over tid, og bruke dette til å bygge en god optisk modell for en prøve av GaAs med oksid og overflateruhet.

AFM-bildene av substratprøven viste omtrent $4.5 \cdot 10^8$ groper/cm^2, og gropene hadde dybde på noen titalls nanometer. Undersøkelser av gropene tydet på at gropenes avbildede form var påvirket av formen på tippen til AFM-proben, og ga indikasjon på at proben ikke var i stand til å nå helt ned til bunnen av gropene. De målte verdiene for overflateruhet var derfor antakeligvis lavere enn de reelle verdiene. Overflateruheten på substratprøven ble målt til å være 1.3-2.0 nm på ulike tidspunkter i ukene etter at prøven ble eksponert for luft. Problemer med uventet drift og forvrengninger av AFM-bildene gjør at vi ikke kan stole på de målte verdiene for ruhet fra AFM på substratprøven, og de må anses som grove estimater. Fra SE-målingene ble det laget flere optiske modeller. Modellene ble tilpasset målingene for å finne den mest passende modellen, for så å kunne estimere tykkelsen på oksidlaget fra denne modellen. Ideelt sett ville resultatene fra AFM blitt brukt som supplement til SE-målingene for å forbedre den optiske modellen, men siden AFM resultatene var såpass usikre ble disse ikke brukt som supplement til SE-modellen. Det ble dermed ikke gjort noe nøyaktig estimat av oksidtykkelsen på substratprøven, men det antas at tykkelsen er minst 1 nm etter 12 uker med eksponering for luft.

AFM-bildene av bufferprøven viste en svært flat overflate med terrasselignende strukturer. Den gjennomsnittlige høydeforskjellen mellom naboterrasser var omtrent 0.28 nm, som er halvparten av gitterkonstanten for GaAs. Disse terrassene er antatt å stamme fra GaAs som har dannet seg lagvis av halve enhetsceller på substratets overflate, antakeligvis funder dannelsen av bufferlaget. Ruheten målt med AFM for bufferprøven var ca. 0.35 nm de første dagene, og

avtok til ca 0.30 nm i de påfølgende ukene. Det optiske profilometeret målte en overflateruhet på 0.36-0.39 nm, 9 uker etter bufferprøven ble eksponert for luft. Fra SE-målingene ble det laget flere optiske modeller. Modellene ble tilpasset målingene for å finne den mest passende modellen, for så å kunne estimere tykkelsen på oksidlaget fra denne modellen. Ved å kombinere resultatene fra SE-målingene med AFM resultatene ble oksidtykkelsen på bufferprøven estimert til å være 0.8 nm én time etter eksponering for luft, 1.9 nm etter to uker, og 2.2 nm etter fire uker.

Table of Contents

1 Introduction **1**
1.1 Background . . . 1
1.2 Problem formulation . . . 5
1.3 Structure of the thesis . . . 6

2 Basic Theory **7**
2.1 Atomic force microscopy . . . 7
2.1.1 Theory . . . 7
2.1.2 AFM artefacts and image processing . . . 9
2.1.3 Estimation of uncertainty . . . 14
2.2 Variable angle spectroscopic ellipsometry . . . 15
2.2.1 Theory . . . 15
2.2.2 Modelling and data fitting . . . 17
2.3 X-ray photoelectron spectroscopy . . . 19
2.4 Optical profilometry . . . 22

3 Experimental Method and Details **23**
3.1 Experimental details of the characterization methods . . . 23
3.1.1 Atomic force microscopy . . . 23
3.1.2 Variable angle spectroscopic ellipsometry . . . 24
3.1.3 Optical profilometer . . . 25
3.2 Re-oxidation experiments . . . 25
3.2.1 Substrate sample . . . 26
3.2.2 Buffer sample . . . 27
3.3 Sample overview . . . 28
3.4 AFM image processing . . . 29
3.5 VASE modelling . . . 29

4 Results **31**
4.1 AFM drift and distortion . . . 31
4.2 AFM tip-related artefacts and challenges . . . 33
4.3 Substrate sample . . . 36
4.3.1 AFM . . . 36
4.3.2 VASE . . . 41

4.4 Buffer sample 45
4.4.1 AFM 45
4.4.2 Optical profilometer 52
4.4.3 VASE 53
4.5 Comparison of AFM instruments 57

5 Discussion 61
5.1 AFM drift and distortion 61
5.2 AFM tip-related artefacts and challenges 62
5.3 Substrate sample 62
5.3.1 AFM 62
5.3.2 VASE 66
5.4 Buffer sample 71
5.4.1 AFM 71
5.4.2 Optical profiler 73
5.4.3 VASE 74
5.5 Comparison of AFM instruments 76

6 Conclusions and Further Work 77
6.1 Conclusions 77
6.2 Further work 80

A AFM image processing 85

B VASE modelling 89

Chapter 1

Introduction

Reducing the use of fossil fuel energy sources is an important step towards reducing the CO_2 emissions to the atmosphere. An alternative to the carbon-based energy sources oil, coal, and gas, are the renewable energy sources. Most renewable energy sources ultimately come from the sun, such as wind power, hydropower, solar thermal power, and solar cells. Solar cells are especially interesting, as they convert solar radiation directly into electricity, have long lifetimes, and require little maintenance. The cost of solar cells has decreased significantly over the last decades, making it an increasingly attractive energy source. The efficiency of solar cells has also increased over the years, but there is still room to grow.

1.1 Background

A solar cell produces electricity by absorption of solar radiation. A solar cell is made of a semiconducting material, and characteristic for semiconductors are their energy band gaps. Incident photons on the solar cell that have a lower energy than this band gap are not absorbed in the semiconductor, but transmitted through the material. Incident photons with energy equal to or larger than the band gap of the semiconductor are absorbed by exciting an electron from the valence band to the conduction band. The first generation solar cells are crystalline semiconductors. These are single band gap materials, and are therefore limited to a maximum theoretical efficiency, called the Shockley-Queisser limit, a limit that varies with the band gap. The efficiency limit is $\eta \approx 33\%$ for band gaps of $E_g \approx 1.4$ eV, which is approximately the band gap of GaAs [1], [2].

A possible way of increasing the efficiency limit of a solar cell is to make a device with multiple band gaps, in order to absorb a wider range of the solar radiation. One option is the multi-junction solar cell, where multiple semiconductors with various band gaps are grown layer by layer to form a single structure with multiple separate band gaps. The challenge with this approach is that the materials used for the fabrication of such a solar cell must be closely lattice-matched, in order to avoid defects in the solar cell, as defects are a significant loss mechanism. A different option would be to make a solar cell where one introduces an intermediate energy band between the valence and conduction band, effectively giving the material three band gaps. This is called an intermediate band solar cell (IBSC), and is one of the so-called *third generation solar cells*. An illustration of the principle of the IBSC is shown in Figure 1.1.

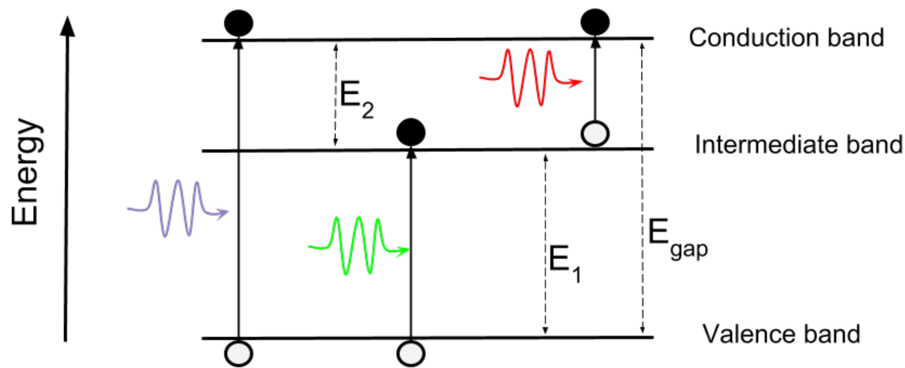

Figure 1.1: Schematic of the principle of an intermediate band solar cell. Electrons can be excited across the full band gap E_{gap}, as well as both to and from the intermediate band, E_1 and E_2. This allows the solar cell to absorb more of the incoming solar radiation than if there was only one energy band gap.

Figure 1.2 illustrates how the three generations of solar cells will compare to one another in the future, in terms of projected cost and efficiency. The first generation crystalline solar cells have a modest conversion efficiency, and are relatively expensive. The second generation solar cells are cheaper to manufacture than the first generation solar cells, but this affects the quality of the solar cells, and yields a lower conversion efficiency. The third generation solar cells aim to keep the manufacturing costs down, while also exceeding the Shockley-Queisser limit, which limits the first and second generation solar cells, since they are both based on single band gap semiconductors.

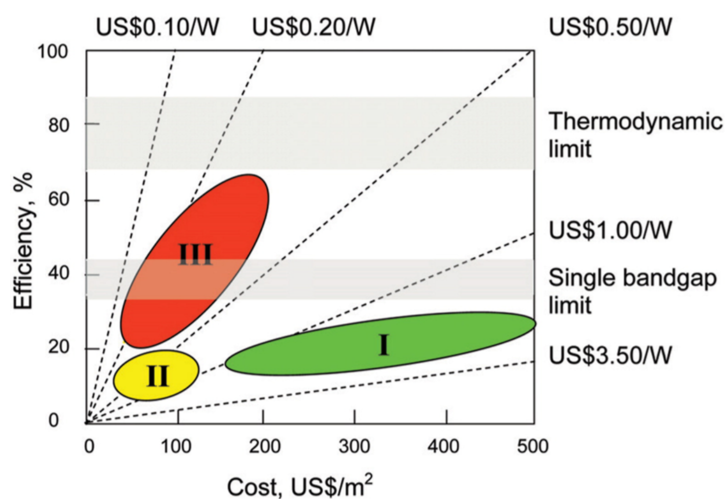

Figure 1.2: The three solar cell generations (I, II and III) are defined by their potential efficiency and cost. First generation solar cells are relatively expensive with a modest conversion efficiency, second generation solar cells are cheaper than the first generation, at the expense of conversion efficiency, and the third generation solar cells aim to reduce the manufacturing costs while exceeding the Shockley-Queisser limit that limits the first and second generation solar cells. Figure taken from [3].

The IBSCs have a theoretical efficiency limit of around 50 % higher than a conventional single band gap solar cell [4]. IBSCs have been researched for only a few decades, and the optimal materials and fabrication methods are still to be identified. One possible configuration of an IBSC utilizes quantum dots in order to create an intermediate energy band in the band gap. An illustration of such a quantum dot intermediate band solar cell (QD-IBSC) is shown in Figure 1.3. For more information about QD-IBSCs, see Ref. [5].

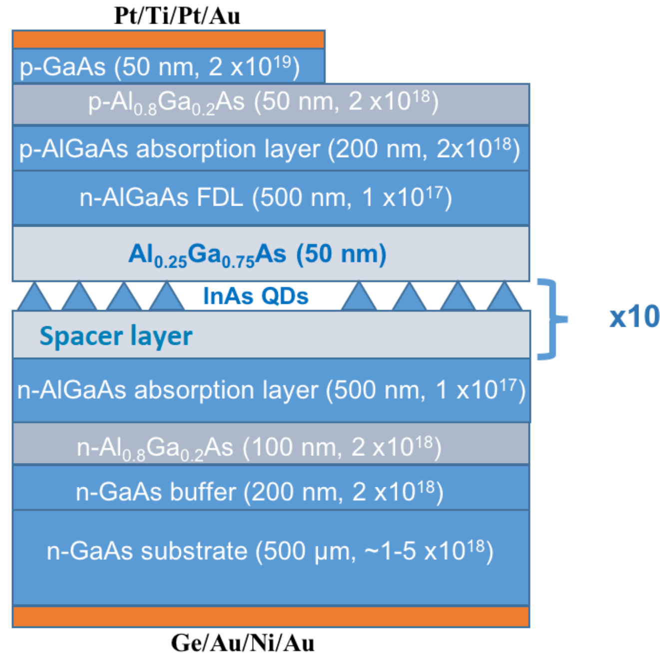

Figure 1.3: Schematic of an intermediate band solar cell. The key features in this figure are the QD and spacer layers. The structure includes 10 layers of QDs and between each QD layer is a spacer layer. Figure by Mohana Rajpalke.

We still do not know what the optimal QD-IBSC consists of. The performance of the QD-IBSC depends on the various properties of the quantum dot and spacer layers, i.e. the quantum dot size, density, and composition of the dots and spacer layers. One way of of determining which material compositions and solar cell structures that will produce the most efficient QD-IBSC is to perform simulations of various QD-IBSC structures, to virtually test the performance of the solar cell. For this, we need good optical models for the potential solar cell structures, and this requires knowledge of the opto-eletronic material properties of each layer of the solar cell. Variable angle spectroscopic ellipsometry (VASE) is a charcterization method that gives insight into the optical properties of layered structures, making VASE a fitting characterization method for this task.

Earlier work at NTNU on using VASE to characterize QD-IBSCs has been done by one of my supervisor's previous master students, Maja Bjerke Drøyli, described in her master's thesis, Ref. [6]. Drøyli used VASE in an attempt to model a full solar cell structure, such as the one illustrated in Figure 1.3. This proved to be a very difficult task, as the structure includes multiple layers of various thickness that have varying doping type and concentrations, as well as material compositions and layers containing QDs. Drøyli decided to instead look at a simplified structure, and make a new attempt at modelling. One of these simplified structures is shown in Figure 1.4. This structure had the quantum dots on the surface of the structure, and the materials were undoped.

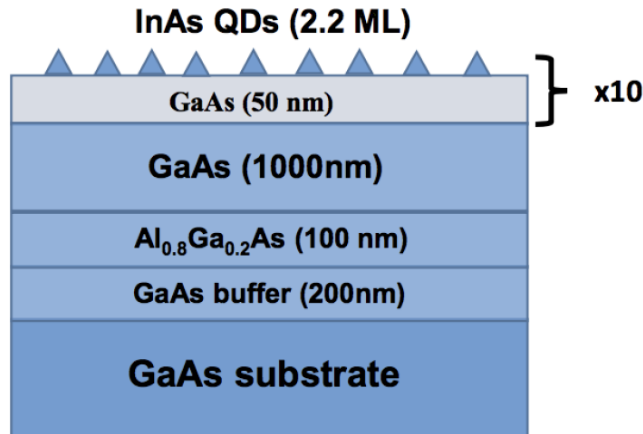

Figure 1.4: Schematic of a simplified solar cell structure, as investigated by Maja Drøyli in her Master thesis, Ref. [6]. The quantum dots are on the surface of the structure, and the layers are undoped. Figure by Mohana Rajpalke.

One of the findings of Maja Drøyli's thesis, Ref. [6], was that it was very difficult to separate the effect of the quantum dots from the effects of surface roughness and oxide on the sample surface. This caused problems when trying to accurately model the quantum dots on the sample surface, as the effects of surface roughness and oxide gave an undetermined contribution to the measured data. A solution to this problem would be to measure the surface roughness and native oxide composition and layer thickness using other characterization methods, and include these measured values in the model for the structure, thereby obtaining a more reliable optical model from the VASE measurements.

In the fall of 2017 I started work on my Specialization Project in Physics, Ref. [7], under the supervision of Associate Professor Turid Reenaas, and the intention was that I would continue the work done by Maja Drøyli in her master's thesis. As even the simplified structure shown in Figure 1.4 had proven quite difficult to model, we decided to further simplify the task and only examine undoped GaAs substrates. My specialization project work, Ref. [7], focused on VASE simulations of surface roughness and oxide on GaAs substrates, and this master's thesis is a continuation and further development of the work done in my specialization project.

1.2 Problem formulation

This study has been focused on determining the oxide layer thickness and surface roughness of re-oxidising GaAs substrates. Two GaAs wafers had their native oxides removed by thermal desorption in an MBE machine, and were then re-oxidised by exposure to air. One of the samples had a 300 nm GaAs buffer layer grown by MBE before being exposed to air. The other sample did not receive any further treatment beyond the thermal desorption before being exposed to air. This preparation of the two samples ensured that we had two ”extreme” cases, so to speak; we expected the sample without the buffer to be quite rough, and the one with the GaAs buffer we expected be very smooth, supposedly atomically flat after the buffer growth. After the samples were exposed to air we expected them to re-oxidise, and the oxide layers were expected to consist of Ga oxide and As oxide.

Atomic force microscopy (AFM) was used to obtain high resolution topographic images of the sample surfaces, and determine the surface roughness in the minutes, days, and weeks after the samples had been exposed to air. Towards the end of the thesis work, an optical profilometer also became available for use, and some measurements using this instrument were performed on one of the samples. Measurements using variable angle spectroscopic ellipsometry (VASE) were also done in the minutes, days, and weeks after samples were exposed to air, and the ellipsometry software was then used to create optical models for the samples. By fitting the various models to the measured data, we could determine which models fit the measurements best, and from there determine how the oxide layer thickness developed over time. Towards the end of the thesis work, we were also able to do some X-ray photoelectron spectroscopy (XPS) on one of the samples, and gain insight into the elemental composition of the oxide layer, as well as measure the thickness of it. However, the results of the XPS measurements arrived quite late in my thesis work, and will therefore not be included in this thesis. As XPS was intended to be a significant part of the work, the theory on XPS will be included in this thesis. The AFM measurements were performed by me, with some help in the beginning from postdoctoral researcher Mohana Rajpalke. Mohana Rajpalke was also responsible for the thermal desorption of the oxide in the MBE machine of the two samples used in this work. The VASE measurements were performed by my co-supervisor, PhD candidate Thomas Brakstad. The optical profilometry, as well as the data modelling for the VASE measurements and image processing and analysis of the AFM images were all done by me.

1.3 Structure of the thesis

This thesis is organized in 6 chapters:

Chapter 2: *Basic theory.* Covers the basic theory of atomic force microscopy (AFM), variable angle spectroscopic ellipsometry (VASE), X-ray photoelectron spectroscopy (XPS), and optical profilometry, which are the characterization methods used in this work.

Chapter 3: *Experimental Method and Details.* Describes the experimental details of the characterization techniques AFM, optical profilometry, and VASE, as well as the method of the main experiments of this thesis. AFM image processing and VASE data analysis is also covered in this chapter.

Chapter 4: *Results.* Presents the results from the measurements with AFM, optical profilometry, and VASE.

Chapter 5: *Discussion.* Presents the discussion and interpretation of the results from Chapter 4.

Chapter 6: *Conclusions and Further Work.* The conclusions are presented along with recommendations for further work.

Chapter 2

Basic Theory

In this chapter, the basic theory of the characterization methods used in this thesis will be presented. They are atomic force microscopy (AFM), variable angle spectroscopic ellipsometry (VASE), X-ray photoelectron spectroscopy (XPS), and optical profilometry. AFM will be presented in terms of basic principles, and image processing and scanning artefacts will also be covered. Next, the basic principles of VASE will be presented, along with some theory on the data modelling of the obtained VASE measurements. Finally, the basic principles of XPS and optical profilometry will be presented. As this thesis is a continuation of my project work, this chapter is based on and further developed from the theory chapter of my project report, Ref. [7].

2.1 Atomic force microscopy

2.1.1 Theory

This section is largely based on Ref. [8].
Atomic force microscopy (AFM) can be used to obtain high-resolution topographic images of a sample surface. The instrument makes use of a cantilever with a very sharp tip in close proximity to, or touching the sample surface. As the tip approaches the sample, forces between the tip and the surface cause a deflection of the cantilever. Should the tip encounter a convex feature on the surface, it will deflect away from the sample. Correspondingly, if the cantilever encounters a concave feature in the surface, it will deflect towards the sample. The deflection of the cantilever is monitored with a laser. As the cantilever deflection changes, so does the path of the laser light, and this is measured by a position sensitive photon detector (PSPD). The setup is illustrated in Figure 2.1. The topography of a sample is obtained by scanning the surface in a raster-like pattern with the cantilever, as shown in Figure 2.2, and translating the detected laser deflection into a topographical image, hereafter referred to as an AFM image.

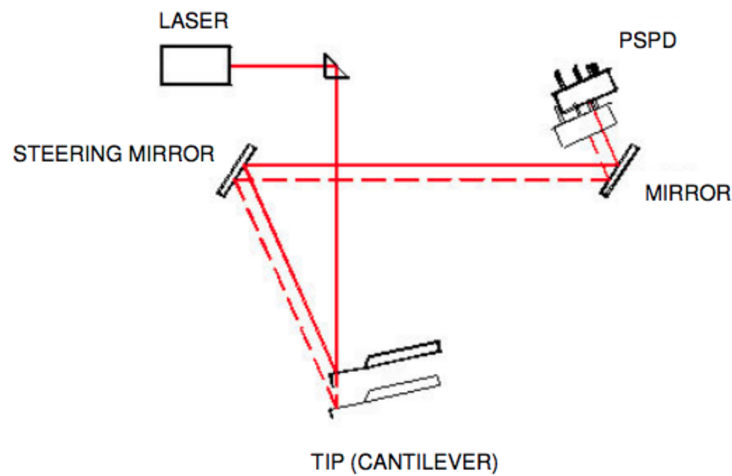

Figure 2.1: Illustration of principle behind AFM. The setup includes a laser, cantilever, steering mirror, stationary mirror, and position sensitive photo detector (PSPD). The solid red line shows the path of the laser beam, and the dashed line illustrates how the path of the laser beam is changed by the deflection of the cantilever. Figure taken from [9].

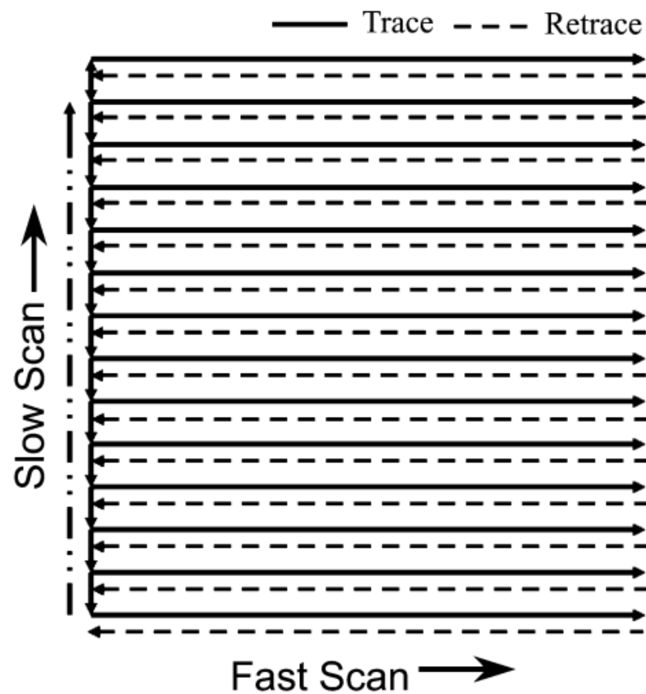

Figure 2.2: Schematic of the AFM probe motion during imaging. The probe scans forwards (indicated as Trace) and back (indicated as Retrace) in the fast-scan direction, then moves a step in the slow-scan direction, and so on. The image is composed of data collected from either a trace or retrace scan. Figure taken from [10].

2.1.2 AFM artefacts and image processing

During AFM scanning, some artefacts may appear in the resulting image. It is important to recognize and properly compensate for or remove these image artefacts in order to obtain the true surface topography.

Tip-related artefacts

The AFM image is a convolution of the probe tip and the sample surface. Therefore, the resolution of the surface topography is directly tied to the radius of the tip. A wide tip will cause any convex feature to appear wider than they actually are, and any concave feature will appear shallower than they actually are, see Figure 2.3. If the shape and size of the tip are known, it is possible to remove the probe's geometric effect on the image by a process known as deconvolution. However, as the geometry of the tip is generally not simple, and can vary from probe to probe despite being provided by the same manufacturer, deconvolution might prove difficult.

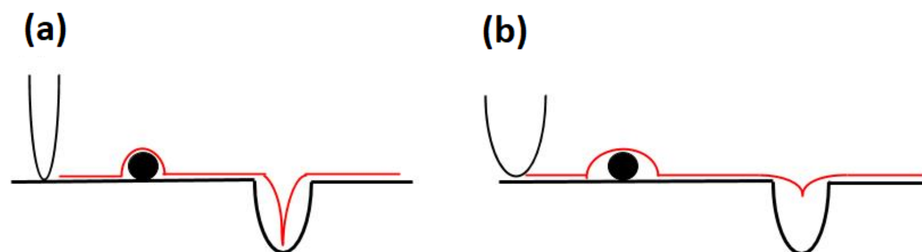

Figure 2.3: Illustration of how AFM resolution depends on the radius of the cantilever tip. A wider tip causes convex features to look wider, and concave features to look shallower.

If the tip has been contaminated or broken, this will also largely affect the resulting AFM image. Figure 2.4 shows two AFM images of the same area of a biaxially oriented polypropylene film sample surface. The image in Figure 2.4a is obtained using a fresh tip, meaning that the tip is free of contamination, hence the topographic image should closely resemble the actual surface topography. The image in Figure 2.4b is a scan of the same area of the sample, but the tip has now been intentionally contaminated. Assuming you have some idea of what the surface should look like, the effect of a contaminated tip is easily identified, as it causes a noticeable blurring of the image [11].

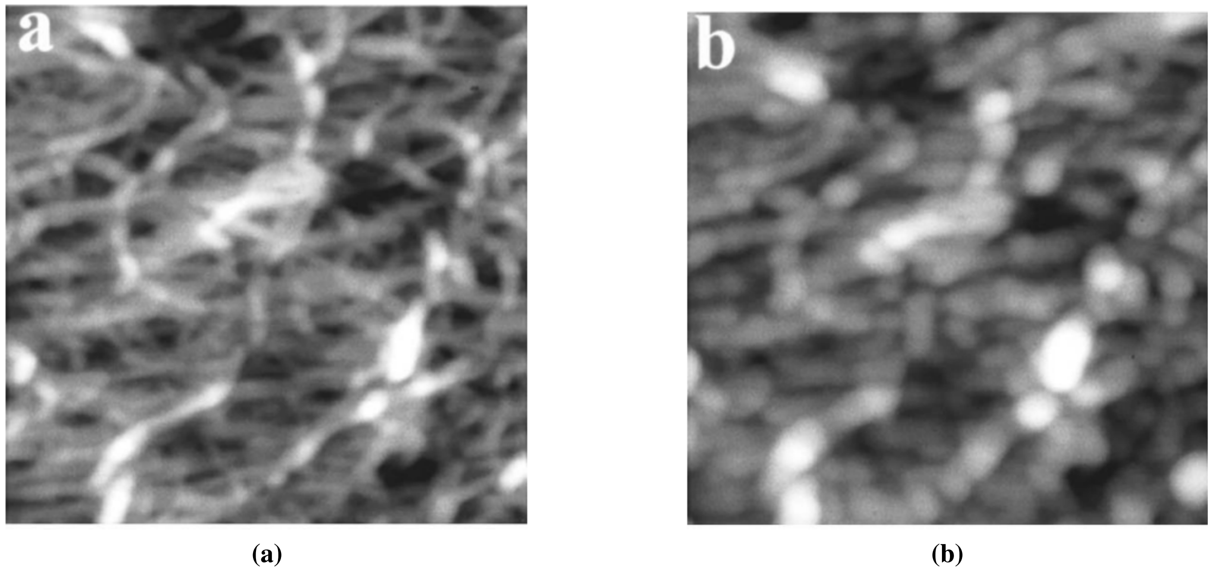

(a) (b)

Figure 2.4: Illustration of the effect of a contaminated tip. (a)AFM image obtained by scanning a biaxially oriented polypropylene film surface with a fresh tip. (b) AFM image obtained of the same area after the tip was contaminated. Images taken from [11].

Figure 2.5a illustrates a depression in a sample surface being scanned by a chipped triangular tip. As the tip moves along the flat upper part of the sample, or the bottom of the depression, contact between tip and sample is solely at the apex of the tip. However, as the tip moves down and up the sides of the depression, contact between the sample and the tip is not at the apex, but rather at the sides of the tip. The AFM image is reconstructed based on the assumption that the interaction between the tip and sample is solely at the apex, and the imperfection in the tip results in a false reconstruction of the sample topography, as seen in Figure 2.5b [12].

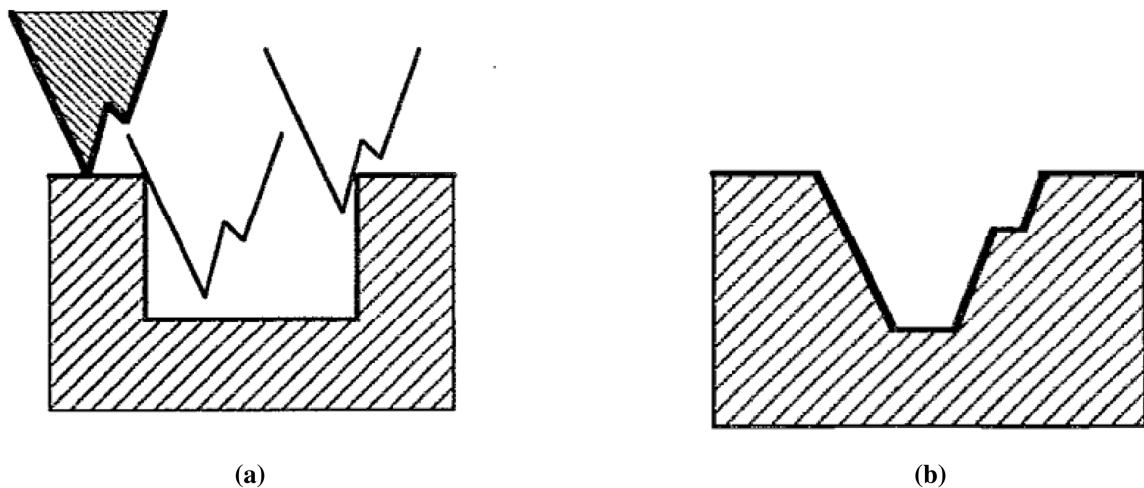

Figure 2.5: Illustration of the effect of a broken tip. (a) The real surface topography and the broken tip. (b) The resulting surface topography as interpreted by the AFM due to the broken tip. Figure taken from [12].

Drift

Drift may appear as a stretching or smearing of the AFM image, and may be caused by a number of things. One type of drift is thermal drift, caused by a difference in temperature between the sample and the sample holder. As the tip is very small, and has a small heat capacity, it is very sensitive to changes in temperature. Light from the laser, or touching of the sample can be enough to change the temperature of the tip, and thereby change the relative position of the tip. The best way to avoid or minimize this issue is to allow the system to reach thermal equilibrium before starting the scanning [13]. Changes in air flow in and out of the scanner/probe area might affect the image, and in an open loop system there will also always be some drift, due to the intrinsic drift of the piezo scanner. Possible solutions are to increase the scan rate, as the drift is time dependent, or change the scan direction so it aligns with the drift, and thereby reduce the influence of the drift [14]. Another type of drift may stem from the mounting of the sample. Usually, when mounting the sample on the AFM sample holder, adhesive tape is used to keep the sample in place during scanning. The tape may perform some relaxation after the initial mechanical stress of mounting the sample, and this may appear on the AFM images as a drift. A possible way to combat this issue is to mount the sample with the adhesive tape, and then leave the sample on the holder for a time before scanning, so that the tape stabilizes. Another solution is to not use tape at all, but simply put the sample onto the holder without fastening it. Users must be aware that the tip and sample are touching, and this may cause the sample to move if it is not heavy enough to withstand the tip being dragged across the surface.

Hysteresis

Differences in material properties and dimensions of the piezoelectric elements in the scanner cause each scanner to respond differently to an applied voltage. This response is conveniently measured in terms of sensitivity, a ratio of piezo movement to piezo voltage (i.e., how far the piezo extends or contracts per applied volt). This relationship is not linear, as the piezo scanners exhibit more sensitivity (i.e., more movement per volt) at the end of a scan line than at the beginning. This causes the forward and reverse scan directions to behave differently and display *hysteresis* between the two scan directions [15]. The non-linear relationship between

applied voltage and position is shown in Figure 2.6.

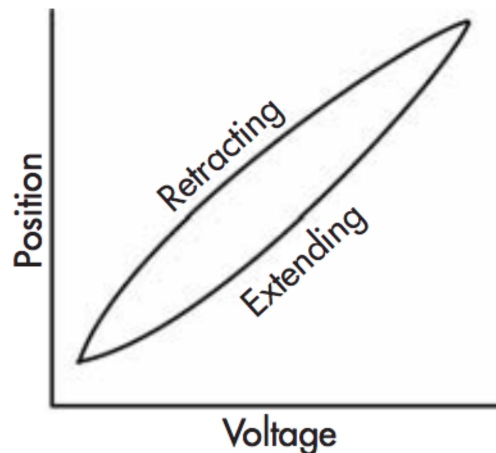

Figure 2.6: Effect of non-linearity and hysteresis. Figure taken from [15].

Figure 2.7 shows an example of how hysteresis affects an AFM image. Comparing the top half and bottom half of the images, as well as the trace to the retrace, there is a clear difference in the spacing and size of the pits. This is due to scanner hysteresis.

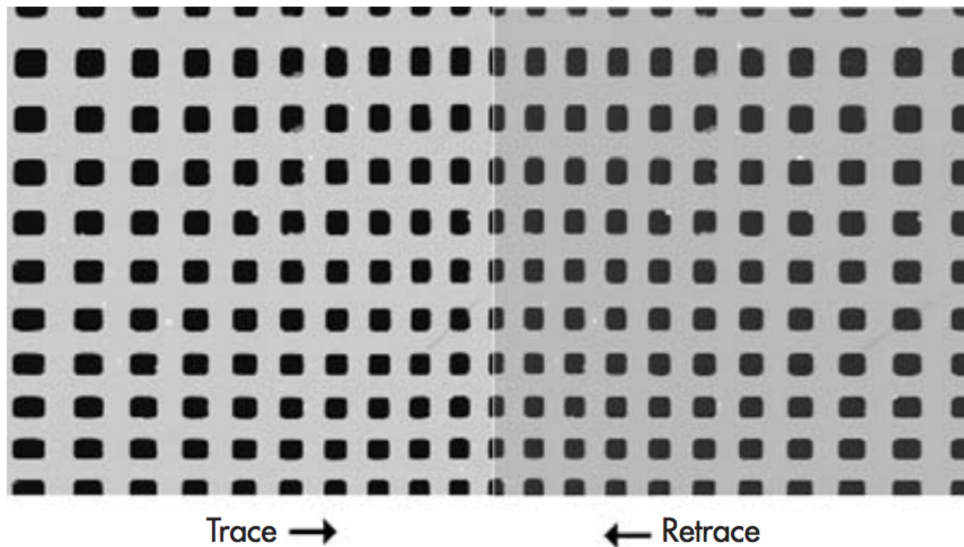

Figure 2.7: Image shows 100 µm x 100 µm scans in the forward (trace) and reverse (retrace) directions of a two-dimensional 10 µm pitch grating without linearity correction. Both scans are in the down direction. Notice the differences in the spacing, size, and shape of the pits between the bottom and the top of each image. The effect of the hysteresis loop on each scan direction is demonstrated. Image taken from [15].

Creep

Scanner creep occurs when a large offset voltage is applied to the scanner. The scanner moves the majority of the offset distance quickly, and then slows down to move the remaining distance. However, the scanner starts scanning again before the entire offset distance has been covered, so the scanner is still slowly moving towards the offset position as the scanning starts. This

causes a disturbance in the image, as shown in Figure 2.8. Creep appears in the image as an elongation or stretching of features in the direction of the offset for a short period of time after the offset. Creep may also occur when using the ”Frame down” or ”Frame up” commands in software used for AFM instruments [15]. Scanner creep settles out by the end of the scan, but can be avoided by restarting the scan if creep is observed.

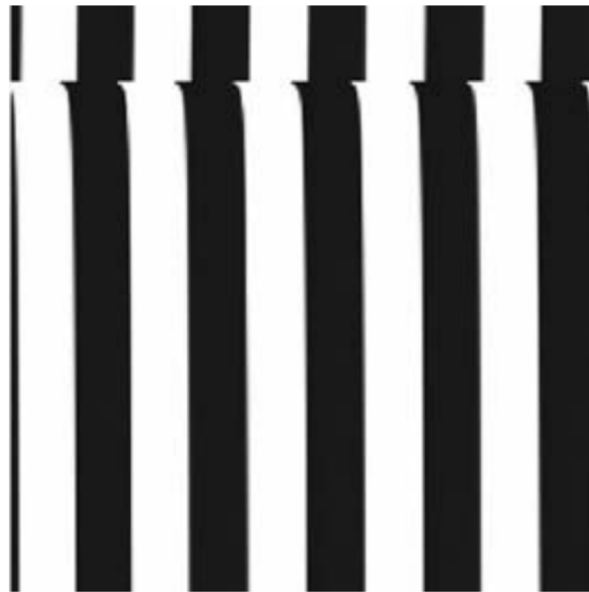

Figure 2.8: The image shows an example of creep. The tip was scanning from top to bottom and an offset of 10µm was performed near the beginning of the scan. The slight bending of the lines that occurs directly after performing the offset is due to creep. The creep settles out by the end of the scan. Image taken from [15].

Bow

Due to the scanner being attached at one end and moving the tip or sample at the other, the free end might not move in a level plane. This may result in a 2nd or 3rd order curvature from the ideal level plane. Figure 2.9 illustrates the trajectory of the scanner in such a case [15], [16]. Bow is most prominent in large scans, as the effect increases with scan size. It is possible to remove this curvature with the help of image processing software.

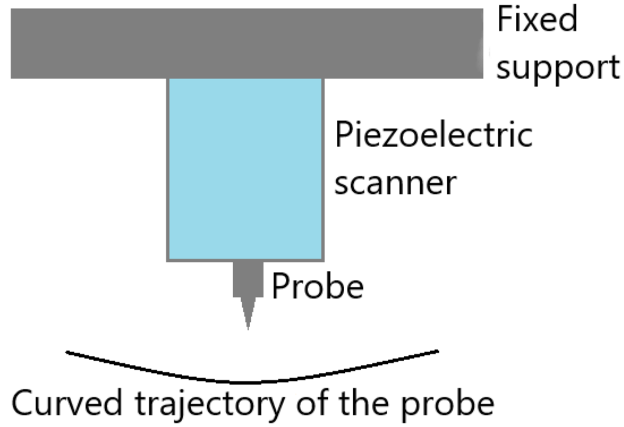

Figure 2.9: Illustration of the curved trajectory of the scanner. Figure adapted from [16].

2.1.3 Estimation of uncertainty

All the above-mentioned scanner and image artefacts may affect the numerical values we obtain from the AFM images. In the interest of finding the most representative value for the surface roughness, multiple consecutive AFM images should be obtained each time a sample is measured. If there are images that deviate significantly from the rest of the set of images, these may be subject to artefacts, and can be filtered out of the set of images. This helps insure more certain results. From the sets of AFM images, a simple estimation of values and their uncertainties can be calculated according to the following equations:

$$x_{avg} = \frac{1}{N}\sum_{n=1}^{N} x_n \qquad \Delta x = \frac{x_{max} - x_{min}}{2}$$

$$\Delta x_{avg} = \frac{\Delta x}{\sqrt{N}} \qquad x_m = x_{avg} \pm \Delta x_{avg}$$

Here, x_n are the measured values, N is the number of measurements, x_{avg} is the average value for the measurements, Δx is the uncertainty of a measurement, and Δx_{avg} is the uncertainty of the mean. x_{max} and x_{min} are the maximum and minimum values for x in the set of measurements. Finally, x_m is the reported measured value, containing both the average value and the uncertainty in the mean.

2.2 Variable angle spectroscopic ellipsometry

2.2.1 Theory

This section is largely based on Ref. [17]. Variable angle spectroscopic ellipsometry (VASE), sometimes referred to only as spectroscopic ellipsometry (SE), is a characterization technique that measures the polarization state of an electromagnetic wave that has been reflected off or transmitted through a sample, see Figure 2.10. VASE is most commonly used for determining the optical constants refractive index n and extinction coefficient k, or the equivalent complex dielectric function values ε_1 and ε_2.

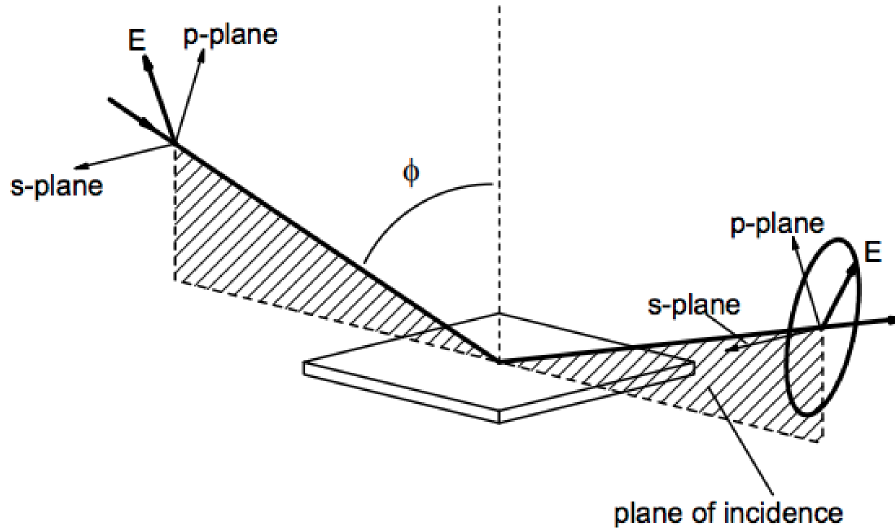

Figure 2.10: Illustration of principle of variable angle spectroscopic ellipsometry. ϕ is the angle of incidence, the p-direction lies in the plane of incidence, and the s-direction is perpendicular to the p-direction. Together, the p-, s-, and direction of propagation form a right handed Cartesian coordinate system. Figure taken from [17].

The ellipsometry measurements do not give n and k directly as their output, but rather the quantities ψ and Δ. Assuming the light is reflected at a plane interface between two isotropic materials, we define a complex ratio ρ by the following relation

$$\rho = \tan(\psi)e^{i\Delta} \tag{2.1}$$

From ψ and Δ, the pseudo optical constants $\langle n\rangle$ and $\langle k\rangle$, or pseudo dielectric function $\langle\varepsilon\rangle$, may be determined:

$$\langle\varepsilon\rangle = \langle\varepsilon_1\rangle + i\langle\varepsilon_2\rangle = \langle\tilde{n}\rangle^2 = (\langle n\rangle + i\langle k\rangle)^2 = \sin(\phi)^2 \cdot \left[1 + \tan(\phi)^2\left(\frac{1-\rho}{1+\rho}\right)^2\right], \tag{2.2}$$

where ϕ is the angle of incidence [18].

The pseudo dielectric function obtained from a measurement is a combination of all the dielectric functions of all the layers of the measured sample. A large part of doing ellipsometry is decomposing the pseudo dielectric function in order to obtain the contribution from each of the layers of the sample.

The samples used in this work are GaAs substrates. GaAs is a direct band-gap, III-V semiconductor with zinc-blende crystal structure. The band structure of GaAs is shown in Figure 2.11. The arrows in Figure 2.11 indicate some of the points where the valence and conduction bands are parallel, which corresponds to the points where the joint density of states gives a large contribution to the imaginary part of the dielectric function, ε_2. We call these the *critical points*, and any features of ε_2 (i.e. peaks) in an ellipsometry plot will occur at the energies of the critical points.

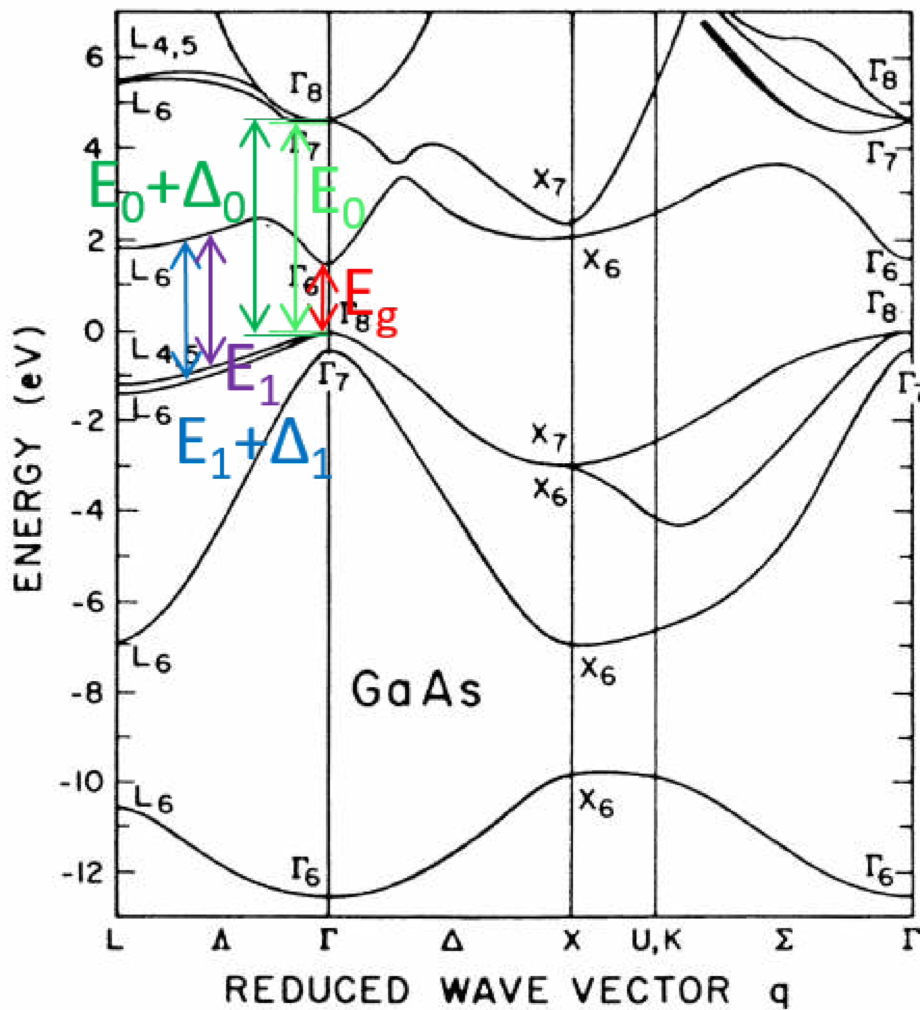

Figure 2.11: Band diagram of GaAs. The arrows point to parallel bands, corresponding to critical points. Figure adapted from [6].

2.2.2 Modelling and data fitting

As an ellipsometry measurement only provides the quantities ψ and Δ as a function of wavelength, modelling and data fitting is an important part of VASE. In order to determine the properties of interest, such as surface roughness or layer thicknesses, one must perform a model-based analysis of the measurements. The VASE analysis software used in this thesis is called CompleteEASE, and is by J.A. Woollam Co., Inc. The general approach to doing a model-based VASE analysis in CompleteEASE is described as follows in the CompleteEASE data analysis manual [18]:

1. SE data is measured on the sample.
2. A layered optical model is built which represents the nominal structure of the sample. This model is used to ”generate” SE data.
3. Model fit parameters are defined, and then automatically adjusted by the software to improve the agreement between the measured and the model-generated SE data. This is known as ”fitting” the data.
4. The results of the fit are evaluated. If the results are not acceptable, the optical model and/or defined fit parameters are modified, and the data is fit again.

Figure 2.12 illustrates the basic approach to SE data analysis.

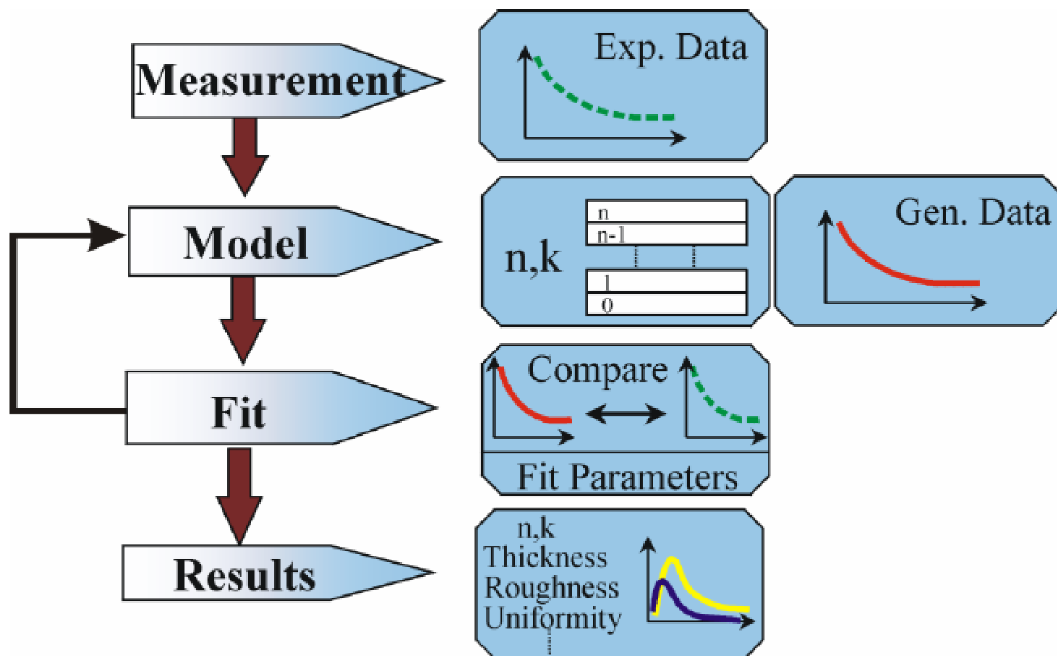

Figure 2.12: SE data analysis flowchart. Figure taken from [18].

A model may include several unknown quantities, such as multiple material layers of unknown thicknesses, surface oxides, or surface roughness. The mean square error, MSE, is very useful in quantifying how well the model fits with the experimental data. The MSE is defined as follows;

$$MSE = \sqrt{\frac{1}{3n-m}\sum_{i=1}^{n}\left[\left(N_{E_i}-N_{G_i}\right)^2+\left(C_{E_i}-C_{G_i}\right)^2+\left(S_{E_i}-S_{G_i}\right)^2\right]} \times 1000, \quad (2.3)$$

where n is the number of wavelengths, m is the number of fit parameters, $N = \cos 2\psi$, $C = \sin 2\psi \cos \Delta$, and $S = \sin 2\psi \sin \Delta$. An ideal fit would imply an MSE of around 1. As there are multiple ways to model a certain structure, the MSE can be a useful guide to finding the best model. However, the MSE is not useful if the model is nonphysical. Therefore, when using the VASE analysis software CompleteEASE, it is important to understand how the software models certain structures. Figure 2.13 shows how a substrate with either an oxide layer, surface roughness, or both is modelled by the software. As we can see from Figure 2.13a and Figure 2.13c, the surface roughness is in effect a separate layer which is composed of 50% whatever material is underneath, and 50% void.

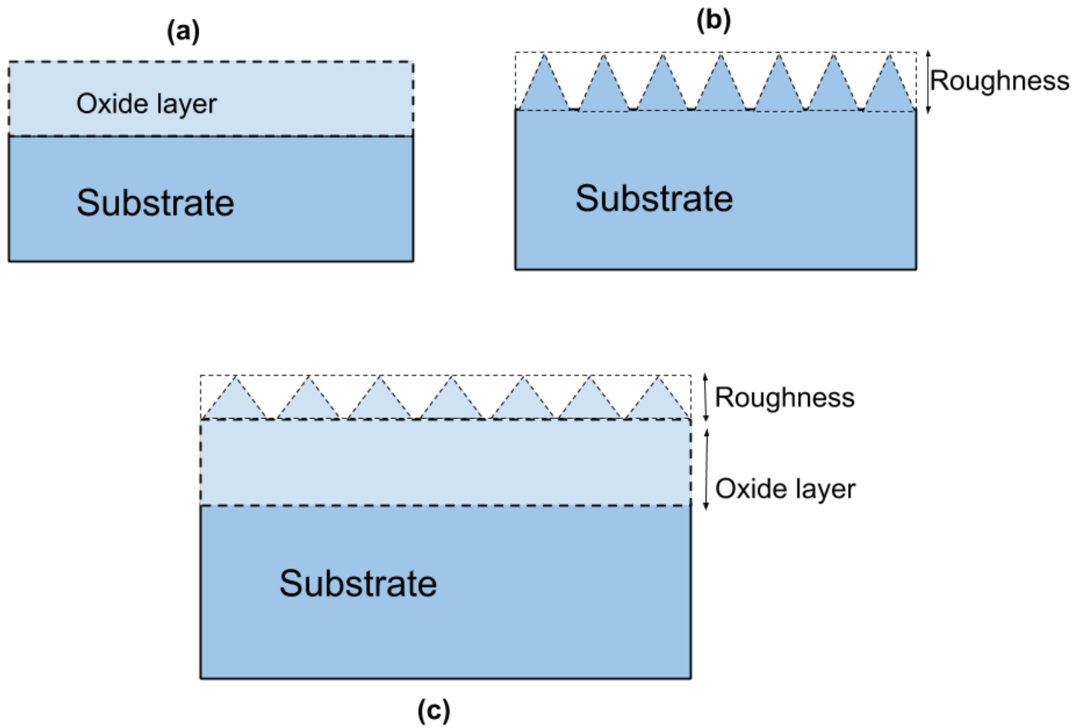

Figure 2.13: Schematic of how the VASE software CompleteEASE models a substrate with an oxide layer (a), a substrate with surface roughness (b), and a substrate with both an oxide layer and surface roughness (c). White part on the top layer of (b) and (c) is void.

In this work, we are trying to model the oxide layer thickness, and the real and imaginary part of the refractive index. The ellipsometer, however, only measures ψ and Δ. The ellipsometer therefore measures over a range of incident angles in order to obtain more data for the modelling. This is the ”variable angle” part of VASE. The ellipsometry software has its limitations, as it tries to make the best fit possible between the model an measured values, and does not take into account the fact that the model should have a physical interpretation. Some of the parameters also correlate, and the vast number of adjustable parameters allows the software to

fit a model very well to a measurement, even if the resulting model turns out to be nonphysical (i.e. negative thicknesses, nonphysical dispersion, etc.). Limiting the number of fit parameters by supplying additional information from other characterization methods is desired, as it makes the results more reliable.

2.3 X-ray photoelectron spectroscopy

This section is largely based on Ref. [19] and Ref. [20]. X-ray photoelectron spectroscopy (XPS) is a useful technique for determining the elemental composition of a material surface, as well as the chemical binding state of these elements. The material is bombarded with X-ray photons, which induce emission of core electrons of the atoms in the material, see Figure 2.14. The electrons that are emitted will have a kinetic energy

$$E_{kin} = E_{photon} - E_{binding} - \phi. \tag{2.4}$$

where E_{photon} is the energy of the X-ray photon, $E_{binding}$ is the binding energy of the electron level, and ϕ is the work function of the spectrometer. The work function accounts for the energy loss as the electron leaves the sample and is absorbed by the detector, and is a constant. The elements in the sample are identified by calculating the binding energies $E_{binding}$, which are characteristic for the elements in the sample. The resultant spectrum from an XPS measurement is the number of photoelectrons per energy interval (presented as counts or counts per second), as a function of kinetic energy or binding energy. According to Ref. [21], the inelastic mean free path λ of GaAs is around 20 Å. This means that only electrons that are emitted within a few λ of the surface will be able to escape the material without loss of energy, and be detected as peaks in the spectrum. This makes XPS a surface sensitive technique.

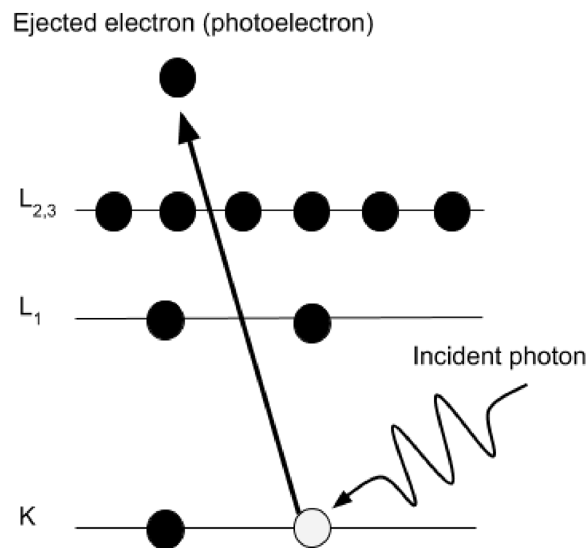

Figure 2.14: Principle of XPS. A core electron is ejected from the atom by interaction with a photon. By knowing the energy of the photoelectron and the photon, the binding energy of the electron can be calculated, which is characteristic for the material of the sample.

Figure 2.15 shows a schematic of a modern XPS instrument. The sample is bombarded with X-rays, and photoelectrons are emitted. The photoelectrons are then focused through an electron lens, transferred to the electron energy analyzer, and separated according to their kinetic energy. The photoelectrons are then detected with the help of i.e. electron multipliers [22]. The entire system is operated in ultra-high vacuum (UHV) in order to avoid collisions between photoelectrons and surrounding particles.

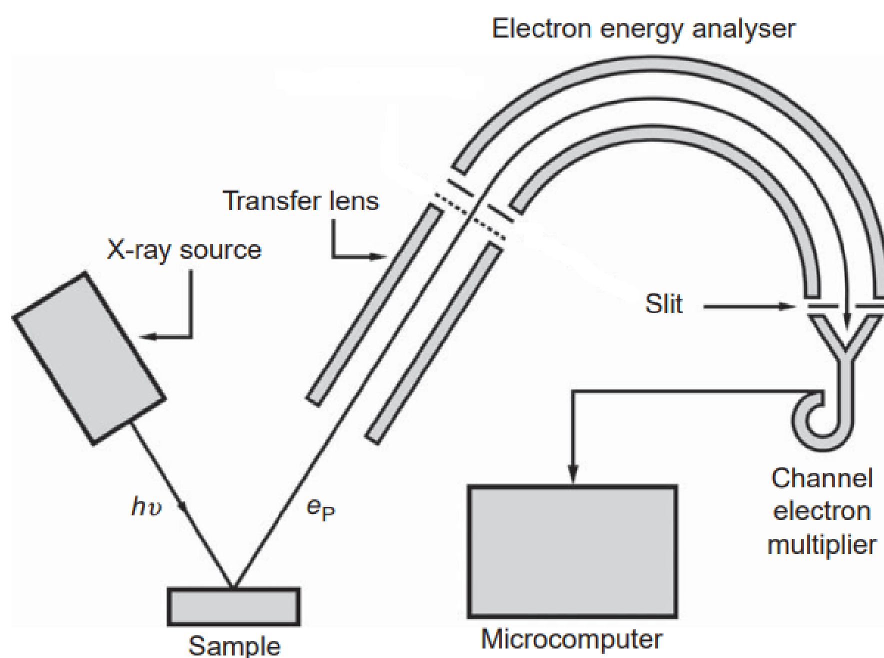

Figure 2.15: Schematic of XPS measurement system. The sample is hit with X-rays that induce an ejection of photoelectrons. The photoelectrons are transferred to the electron energy analyzer through the electron lens, and detected with the help of an electron multiplier. Figure adapted from [22].

A powerful analysis technique in XPS is the Angle Resolved XPS (ARXPS), which allows for more detailed surface characterization. Figure 2.16 shows a material B with a thin overlayer A. If electrons are detected at an angle θ to the normal, the information depth is reduced by an amount equal to $\cos\theta$ [20]. In other words, at normal emission of electrons, we get some signal from both material A and B. If we then increase the emission angle by tilting the surface from horizontal towards the vertical direction, the signal from B decreases as the information depth decreases. Meanwhile, the signal from A gets stronger. This illustrates the dependence of signal intensity on $\cos\theta$, and is the basic principle of ARXPS.

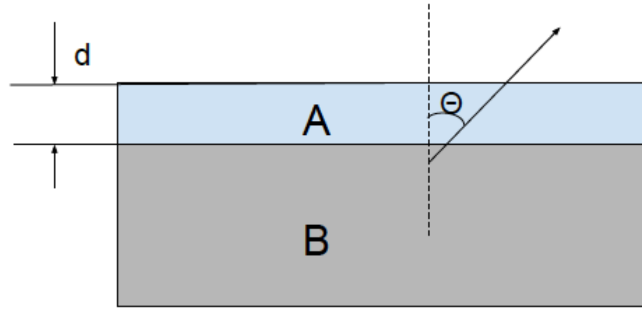

Figure 2.16: Oxide layer A of thickness d on a substrate B. information depth of ARXPS depends on the emission angle θ of the electrons. Figure adapted from [23].

It is possible to estimate the thickness of an oxide layer on a substrate with ARXPS. The following method is described in Ref. [20], with some supplement from Ref. [23]:

Consider a substrate B with an oxide layer A of thickness d, see Figure 2.16. The thickness d can be estimated as

$$d = \lambda \cos\theta \cdot \ln \left[1 + \left(\frac{I_A}{I_B} \right) \Big/ \left(\frac{I_A^\infty}{I_B^\infty} \right) \right], \tag{2.5}$$

where λ is the electron inelastic mean free path, θ is the angle of electron emission relative to the sample normal, and I is the signal intensity from a certain material. If one assumes that $\lambda_A \approx \lambda_B$, and the signal is from the same core level of a certain element in the overlayer or the base, this equation can be simplified [23]:

$$\frac{I_A^\infty}{I_B^\infty} = \frac{\rho_A F_A}{\rho_B F_B}, \tag{2.6}$$

where ρ is the density of the material, and F is the formula weight of the material.

This method has been applied in [23], where it was used to estimate the layer thickness of a native oxide on a GaAs substrate. A fresh GaAs surface exposed to air will react with oxygen as follows:

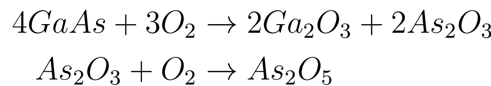

$$4GaAs + 3O_2 \rightarrow 2Ga_2O_3 + 2As_2O_3$$
$$As_2O_3 + O_2 \rightarrow As_2O_5$$

Because As_2O_3 and As_2O_5 are volatile, we expect the oxide layer will be mostly Ga_2O_3. Using the intensity ratio of either the Ga 3d or As 3d core levels from the GaAs substrate, and the Ga_2O_3 from the oxide layer, one can calculate the oxide layer thickness. From Ref. [21], we use $\lambda_{Ga3d} \approx 2.86$ nm and $\theta = 50°$, and equation 2.5 is rewritten

$$d = 1.84 \cdot \ln \left[1 + 2.34 \cdot \frac{I_{Ga_2O_3}}{I_{GaAs}} \right]. \tag{2.7}$$

As a reminder to the reader, the theory on XPS is included in this thesis because XPS was intended to be a significant part of the thesis work. However, due to unavailability of the XPS

instrument, the results of the XPS measurements arrived very late in my thesis work, and will therefore not be included in this thesis.

2.4 Optical profilometry

This section is based on Ref. [24]. The optical profilometer, sometimes also referred to as an optical profiler, relies on the principles of interferometry. The basics of an interferometer is shown in Figure 2.17. An interferometer is an optical device that uses a beam splitter to divide a beam from a single light source into two beams. One beam is sent along the reference arm to a reference mirror and reflected back, the other is sent along the test arm to the sample and reflected back from the surface. The beams recombine at the beam splitter, and the difference in optical path lengths for the beams, the optical path difference (OPD), creates an interference pattern. The interference pattern is then imaged onto a CCD camera. As the reference mirror is of known (and, ideally, perfect) flatness, the OPD is caused by the height variations on the sample surface. The interference fringes can therefore be used to measure the surface topography of a sample with very high precision.

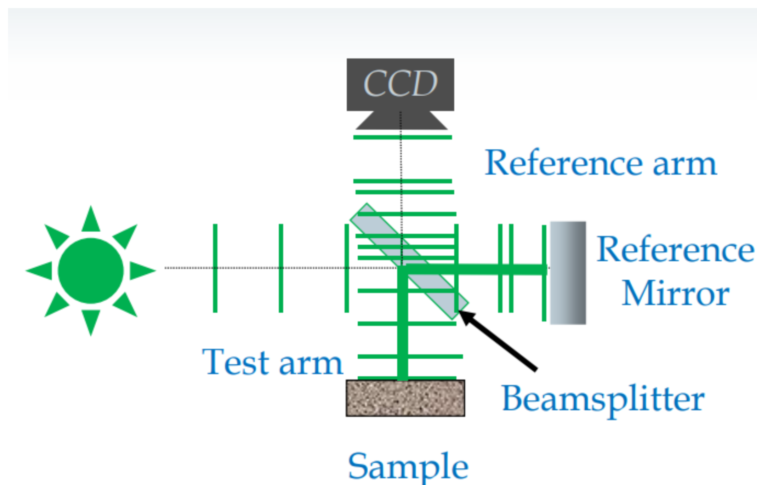

Figure 2.17: Schematic of an interferometer. A single light source is divided into two beams by a beam splitter. The optical path difference (OPD) is the difference in optical lengths travelled by the beams in the reference and test arms. The beams recombine at the beam splitter after being reflected off the reference mirror and sample. An interference pattern is formed due to the OPD, and the interference pattern is then imaged onto the CCD camera. Figure taken from [24].

For very smooth surfaces, so called phase-shifting interferometry (PSI) will give the best resolution. The method relies on controlled phase shifts, usually imparted by mechanically moving the reference mirror. The interference pattern is analyzed pixel by pixel, and converted into a height map for the surface. For more details on the principles of PSI, see Ref. [25].

Chapter 3

Experimental Method and Details

In this chapter, the experimental details for the characterization methods, AFM, optical profilometry, and VASE will be presented. Following is the outline and method of the main experiments, the re-oxidation experiments. Finally, an overview of the samples in the re-oxidation experiments, AFM image processing, and VASE data modelling will be presented.

3.1 Experimental details of the characterization methods

3.1.1 Atomic force microscopy

The AFM mainly used in this thesis work is a Bruker Multimode 8. The probe is a ScanAsyst Air probe from Bruker, made of silicon nitride. Figure 3.1 shows an image of the ScanAsyst tip. The tip has a nominal radius of 2 nm, a maximum radius of 12 nm, and tip height of 2.5-8 µm [26]. The software for the AFM measurements is NanoScope, and the AFM was operated in Bruker's PeakForce Tapping mode [27], as that was the standard for the instrument. Processing of the AFM images were done using the software Gwyddion [28]. The Bruker AFM is the main AFM instrument for this thesis. Unless otherwise specified, all references to AFM and the images presented in the following chapters refer to the Bruker AFM.

Additionally, a Cypher AFM instrument from Asylum Research (part of Oxford Instruments) was used to do some measurements for comparison to the Bruker AFM images. The tip used for the Cypher is a PPP-NCH tip from Nanosensors. The tip is made from highly doped silicon, and has a typical tip radius 7 nm, and tip height between 10-15 µm [29]. The tip is triangular in shape, similar to the ScanAsyst tip shown in Figure 3.1. The AFM was operated in tapping mode.

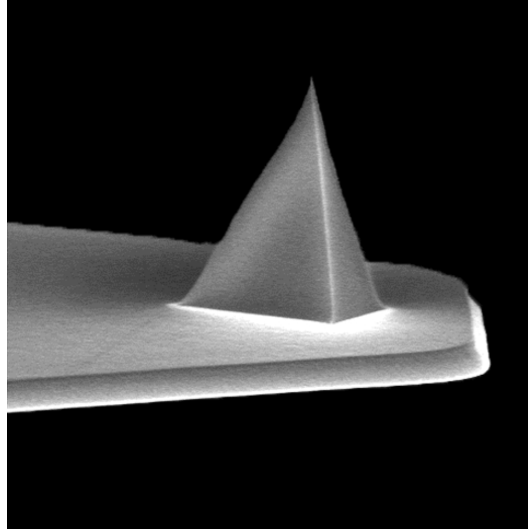

Figure 3.1: Image of the ScanAsyst Air tip used for the Bruker Multimode AFM instrument. The tip is triangular in shape, with a nominal radius of 2 nm, and a maximum radius of 12 nm. Tip height is 2.5-8 µm.

3.1.2 Variable angle spectroscopic ellipsometry

The ellipsometer used in this thesis work is an RC2 Model XI by J. A. Woollam Co., Inc., see Figure 3.2. The wavelength range of the ellipsometer is 210-1690 nm [30], corresponding to approximately 0.7-5.9 eV.

Figure 3.2: Experimental setup of the RC2 ellipsometer with 1) light source, 2) source optics, 3) vertical sample mount, 4) receiver optics and 5) goniometer arm for variable angle measurements. Figure taken from [6], originally adapted from [31].

The software used for both VASE measurements and analysis is CompleteEASE by J. A. Woollam Co., Inc.. CompleteEASE comes with a library of samples that have already been

measured, and the models presented in this thesis are built using the samples found in the CompleteEASE library.

3.1.3 Optical profilometer

The optical profilometer used in this thesis is a Contour GT-K 3D optical microscope from Bruker. The software used for the instrument and for analysis is Vision64. The instrument was operated in PSI mode, and the images obtained are from using the 50x zoom objective. In order to do a scan with the profilometer, the sample stage must be tilted to bring out the right number of interference fringes on the sample. Due to this, the tilt must be removed from the resulting scan, but beyond this there was no image processing.

3.2 Re-oxidation experiments

The main experiments of this thesis were the re-oxidation experiments. These experiments explore how a GaAs surface re-oxidises after having its native oxide removed by thermal desorption, and then being exposed to air. We were interested in several aspects of the re-oxidation:

- How quickly the oxide reappears on the surface after exposing the sample to air.
- How fast the oxide layer grows.
- If and how the surface roughness depends on the growth of the oxide.
- If and how the surface roughness and growth of the oxide depend on how the surface was treated prior to being exposed to air.

Two samples were prepared, one quarter of a 2-inch wafer for each of the two experiments. Both samples were undoped, single-side polished GaAs wafers delivered by WaferTech LLC, and both samples had their native oxides removed in an MBE machine by heating the samples at 630°C for 10 minutes while rotating. The As over-pressure was at $5 \cdot 10^{-6}$ Torr. One of the samples was removed from the growth chamber after the thermal treatment, and set to cool down in the buffer chamber. We will call this sample the *substrate sample*. The other sample had a 300 nm GaAs buffer layer grown by MBE at 590°C after the removal of the oxide, before being transferred to the buffer chamber to cool. This will be referred to as the *buffer sample*. Both samples were cut into several pieces, in order to measure the samples in parallel with both AFM and VASE. One of the substrate sample pieces was measured with both AFM and VASE. Figure 3.3 shows a schematic of the samples in the re-oxidation experiments.

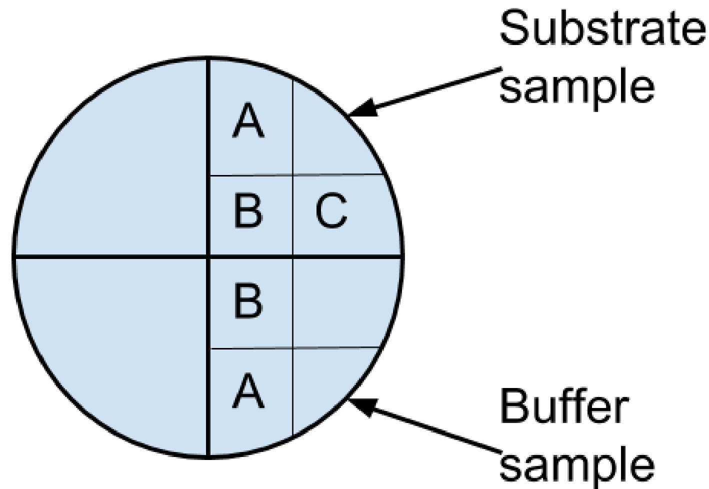

Figure 3.3: Schematic of the samples in the re-oxidation experiments. Two samples were prepared, one quarter of a 2-inch wafer for each of the two experiments. Both samples had their native oxides removed by thermal desorption in an MBE machine. One sample, the substrate sample, received no further treatment before being cleaved into several pieces and exposed to air. Substrate sample A and C were taken to the AFM, substrate sample B was taken to the ellipsometer. The other sample, the buffer sample, had a 300 nm GaAs buffer layer grown by MBE before being cleaved into several pieces and exposed to air. Buffer sample A was taken to the AFM, buffer sample B was taken to the ellipsometer.

3.2.1 Substrate sample

After the substrate sample had cooled down, it was removed from the buffer chamber, cleaved into several pieces, and put into sample boxes. In order to keep the sample from oxidising during removal from the MBE machine and transport to the characterization laboratories, we created a nitrogen atmosphere inside a large plastic bag to work in during transfer and cleaving of the sample. One piece, now named substrate sample A, was taken to the AFM, while another piece, substrate sample B, was taken to the ellipsometer.

AFM

While doing AFM, we kept track of how long substrate sample A had been exposed to air. Our goal was to scan the sample continuously for the first few hours after exposure to air, but due to some difficulties with the AFM instrument substrate sample A was exposed to air for about one hour before we were able to start imaging. Because of this, we returned the next day with another piece of the substrate sample, substrate sample C, and did the measurements again. Substrate sample C had been kept in nitrogen since being removed from the MBE machine, and had not started oxidising. We were therefore able to obtain AFM images for the first hour of exposure to air. Follow up scans were done after approximately three weeks and five weeks, and then sporadically after that. Ideally, we would have done follow up scans once a week after removing the sample from the MBE machine, but as I was not yet authorized to operate the AFM alone when we started this experiment, a few weeks passed by without measurements. Substrate sample B was also scanned once using the AFM. In total, AFM measurements were performed on three different samples in this experiment. Due to this, and to the fact that I was inexperienced with the AFM, not enough care was taken to make sure roughly the same area

was scanned each time. During the first five weeks, the samples were also mounted on and removed from their sample holders before and after each lab session, adding to the realization that the same area was not scanned each time. Not scanning the same area each time could mean the results are subject to local variations on the sample surfaces. However, imaging different locations every time could give an indication on the uniformity of the sample surface.

Substrate sample C was also examined using a second AFM instrument, the Cypher AFM, after the sample had been exposed to air for 15 weeks.

VASE

In parallel to the AFM measurements, ellipsometry measurements were performed on substrate sample B. The ellipsometry measurements were done continuously for the first 20 minutes after exposing the sample to air, then every five minutes for the next 90 minutes, and then every 10-30 minutes for the next hour. Follow up measurements were done after 24 hours, one week, five weeks, ten weeks and twelve weeks. The beam of the ellipsometer is of comparable size to the sample, and the sample has a specific way of being mounted on the ellipsometer, meaning we can be fairly certain that the same area was measured each time. The fact that the beam and sample are of comparable sizes will also make the VASE measurements less sensitive to local variations on the sample surface. The ellipsometer was set to measure over a range of incident angles ϕ between $55°$ and $75°$, and we will use the results obtained at $65°$ for the modelling.

3.2.2 Buffer sample

The buffer sample was prepared the same day as the substrate sample, and was then kept in the buffer chamber of the MBE machine for about two months before being removed. During removal, a nitrogen atmosphere was created inside a large plastic bag covering the opening of the MBE machine, in order to prevent the sample from oxidising. The sample was cleaved into several pieces, and put into sample boxes filled with nitrogen. Buffer sample A was taken to the AFM, and buffer sample B was taken to the ellipsometer.

AFM

The goal was to scan buffer sample A continuously for the first few hours after exposure to air, but due to a problem with the AFM, no scans were obtained during the first two days. The sample remained in the sample box during these two days, in which we had created a nitrogen atmosphere. However, as we cannot assume the sample box is completely airtight, some oxidation probably occurred during those two days. On day three we were able to do AFM, and follow-up scans were done once a week for the next eight weeks. In an effort to scan approximately the same area every time, the sample was fastened to the sample holder using double sided tape on the first day of scanning, and was not removed from the sample holder during the entire experiment. I also made sure to try to place the sample holder on the sample stage identically each time, using the perimeter of the sample stage as a guide. Buffer sample A was also examined using the Cypher AFM, after the sample had been exposed to air for 7 weeks.

VASE

In parallel to the AFM measurements, ellipsometry measurements were performed on buffer sample B. The ellipsometry measurements were done continuously for the first 20 minutes after

exposing the sample to air, then every five minutes for the next hour, and then every half hour for the next 90 minutes. Follow up measurements were done after 26 hours, 2 weeks, and 4 weeks. As the beam of the ellipsometer is of comparable size to the sample, and the sample has a specific way of being mounted, we can be fairly certain that the same area was measured each time, and the measurements are not subject to local variations on the sample surface. The ellipsometer was set to measure over a range of incident angles ϕ between $55°$ and $75°$, and we will use the results obtained at $65°$ for the modelling.

Optical profiler
Buffer sample A and B were also examined using the optical profiler. The measurements were performed after the samples had been exposed to air for 9 weeks. We wanted to see if the profiler could corroborate the results from the AFM, and to see if there were any differences between the AFM sample and the VASE sample. The scan size of the optical profiler is also significantly larger than for the AFM, meaning we would also obtain information about the uniformity of the samples. Due to the instrument becoming available quite late in my thesis work, measurements were only done once, and not continuously as with AFM and VASE. The images obtained from the profiler did not need any processing, apart from removing the tilt caused by the tilt of the sample stage. This was done in the profiler software, Vision64.

3.3 Sample overview

Table 3.1 gives an overview of which characterization techniques were applied to which samples in the re-oxidation experiments.

Table 3.1: Overview of the samples in the re-oxidation experiments, and what characterization techniques each sample was measured with. X indicates that the piece was measured using that characterization method.

Name	Piece	AFM	VASE	Optical profilometer	Comment
Substrate sample	**A**	X			Sample dropped on floor after 5 weeks, not measured again.
	B	X	X		Measured using both AFM and VASE
	C	X			
Buffer sample	**A**	X		X	
	B		X	X	

3.4 AFM image processing

The AFM images were processed using some basic image operations in Gwyddion:

1. Align rows using median (Operation 1)
2. Correct horizontal scars (Operation 2)
3. Shift minimum data value to zero (Operation 3)
4. Remove polynomial background, horizontal and vertical, nth degree (Operation 4)
5. Stretch colour range to part of data (Operation 5)

Which image operations were applied depended on the size and features of the scan. Usually, the scan area was 1 μm^2. In this case, operations 1, 2 and 3 were applied to the image, along with operation 5 if there were any stray extreme values that were appropriate to exclude. In addition to the 1 μm^2 scans, some 5 µm x 5 µm and 50 µm x 50 µm scans were also done. In these cases there was a noticeable bow in the image, and operation 4 was applied after doing operations 1 and 2. Theoretically, removal of a 2nd or 3rd degree polynomial background in the horizontal direction should have levelled the data to our satisfaction. However, in order to get the flatness that we were expecting, the background had to be a 9th degree polynomial. AFM images at various stages of the image processing to illustrate the effect of each of the operations can be found in Appendix A. Gwyddion was also used to read out statistical quantities like RMS roughness, average values, standard deviations, as well as do blind tip estimations, deconvolution and reconstruction of the surface, mask data, and do line profiles.

3.5 VASE modelling

The model based analysis of the VASE data was done in the software CompleteEASE. We know that the samples are GaAs substrates with native oxide layers and some surface roughness. There are two main methods for modelling the surface roughness in particular; either using the CompleteEASE built-in roughness function, or modelling the roughness as an Effective Medium Approximation (EMA) layer. The built-in roughness function in CompleteEASE models the roughness as an EMA layer of 50% void and 50% of the underlying material. The EMA layer function on the other hand, allows the user to specify the elemental composition of the EMA layer, and the percentage of each component. Modelling the roughness with the built-in roughness function produces the exact same MSE as the EMA layer of 50% void and 50% underlying material, but the layer thicknesses deduced from the two models are not the same. This is shown in the end of Appendix B. How the built-in roughness function interacts with the underlying layer is not clear to me, so I will use the EMA layer to model surface roughness. Figure 3.4 shows a screenshot of the user interface for model building in CompleteEASE, along with a representation of the model. The model illustrated is a GaAs substrate with an EMA layer of 50% GaAs oxide and 50% void.
As previously mentioned, CompleteEASE comes with a library of already measures samples that can be used in modelling. The three library samples used to model the samples in the re-oxidation experiments were the GaAs sample, GaAs oxide sample, and the void material. The GaAs sample is measured by University of Nebraska, Lincoln (UNL), who are known to make

good and trustworthy models of a great variety of materials [6]. The GaAs oxide sample is based on measurements done by S. Zollner, see Ref. [32]. The void material is not a measured sample, but is defined to have optical constants of n=1 and k=0 [18].

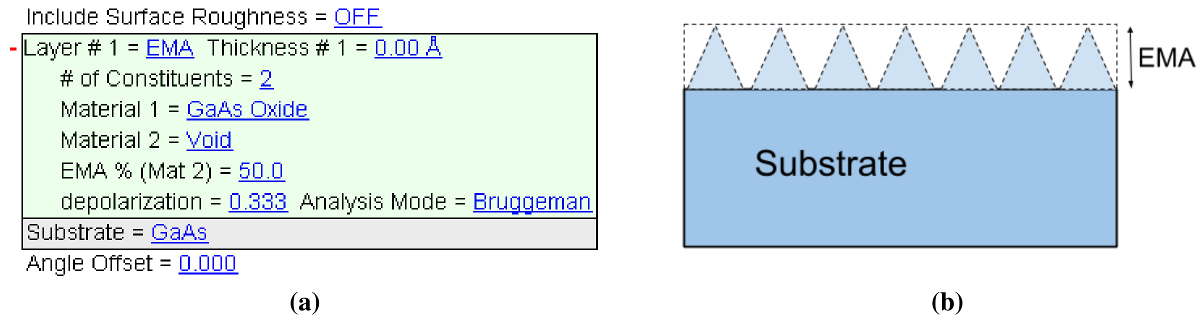

Figure 3.4: (a) User interface for model building in CompleteEASE. This is a model with a GaAs substrate, and an EMA layer consisting of 50% GaAs oxide and 50% void. The surface built-in roughness function is turned off, since we use the EMA layer to model the surface roughness. We have also specified the EMA layer to consist of something else than the underlying material, which is one of the differences between using the EMA layer function and the built-in roughness function. The materials used in the model are taken from the CompleteEASE library. (b) Illustration of the model in (a).

Multiple models including GaAs substrates, oxide layers, EMA layers, and surface roughness were tested in this work. The data sets from the measurements were fitted to each attempted model, to try and find the model that best suited the data as well being the best representation of the physics of the sample. There are a vast number of fit parameters available in CompleteEASE, and generally an increase in fit parameters makes the results less reliable, although it probably produces a better fit. In this thesis, we have limited the fit parameters to layer thickness, surface roughness, and angle offset. Below is a list of the attempted models. This list of models and their corresponding MSE, along with illustrations of some of the models can be found in Appendix B.

1. **Model 1:** GaAs substrate with an EMA overlayer composed of 50% GaAs and 50% void.
2. **Model 2:** GaAs substrate with an EMA overlayer composed of 50% GaAs oxide and 50% void.
3. **Model 3:** GaAs substrate with an EMA overlayer composed of 34% GaAs, 33% GaAs oxide, and 33% void.
4. **Model 4:** GaAs substrate with an EMA overlayer with various percentages for GaAs, GaAs oxide and void. Best model found was 50% GaAs, 10% GaAs oxide, and 40% void.
5. **Model 5:** GaAs substrate with a GaAs oxide overlayer and the built-in roughness function turned on.
6. **Model 6:** GaAs substrate with a GaAs oxide overlayer and an EMA layer on top of that, consisting of 50% GaAs oxide and 50% void.
7. **Model 7:** GaAs substrate with a GaAs oxide overlayer.

Chapter 4

Results

In this chapter, the results of the re-oxidation experiments are presented. There were some unexpected drifts and distortions of the AFM images that may have had an effect on the numerical values obtained from these images. In addition, tip-related artefacts may also have affected the numerical values. Therefore, these will be presented first, and then discussed in the beginning of the next chapter. Thereafter, the results from AFM and VASE for the substrate sample will be presented. Next, the results from AFM, optical profilometry and VASE for the buffer sample will be presented. The AFM results will be presented in terms of AFM images and the measured RMS surface roughness. For all of the AFM measurements, there were multiple images obtained from each laboratory session. Hence, when presenting the results of a set of AFM measurements, values for surface roughness will be given as an average accompanied by an uncertainty (calculated according to the description in Section 2.1.3), along with a representative image for that set of scans. The VASE results are presented as plots of the imaginary part of the pseudo dielectric function, $\langle \varepsilon_2 \rangle$. Despite the VASE measurements being made at multiple angles of incidence, the plots only show the data measured and modelled at $65°$ angle of incidence, as it makes them easier to read. Plots of the evolution of layer thicknesses over time will also be presented. Finally, a small comparative study on the two AFM instruments was also done, and the results will be presented at the end of this chapter.

4.1 AFM drift and distortion

Figure 4.1 shows six images obtained from about one hour of scanning, five weeks after substrate sample B was exposed to air. Comparing the consecutive images, we see that features drift down and to the left in the image, indicating that we are imaging a slightly different area each time. Considering the line labelled with the number 1 in the images, we can also detect some stretch and distortion in the image. If we compare Figure 4.1a to Figure 4.1b, we see that the line is at different angles with the horizontal in the two images. A more thorough analysis using Gwyddion confirms that the angle with the horizontal of the line changes slightly from image to image. The change is not constant, and appears to be random. Although not visible in the images, further analysis using Gwyddion also indicates that when the scan goes from top to bottom, the image is stretched more in the bottom half than in the top half. The same trend is found in the images scanning bottom-up; the stretch becomes more pronounced in the top half of the image compared to the bottom half. In other words, the distortion gets worse during scanning of an image, and resets when a new scan starts.

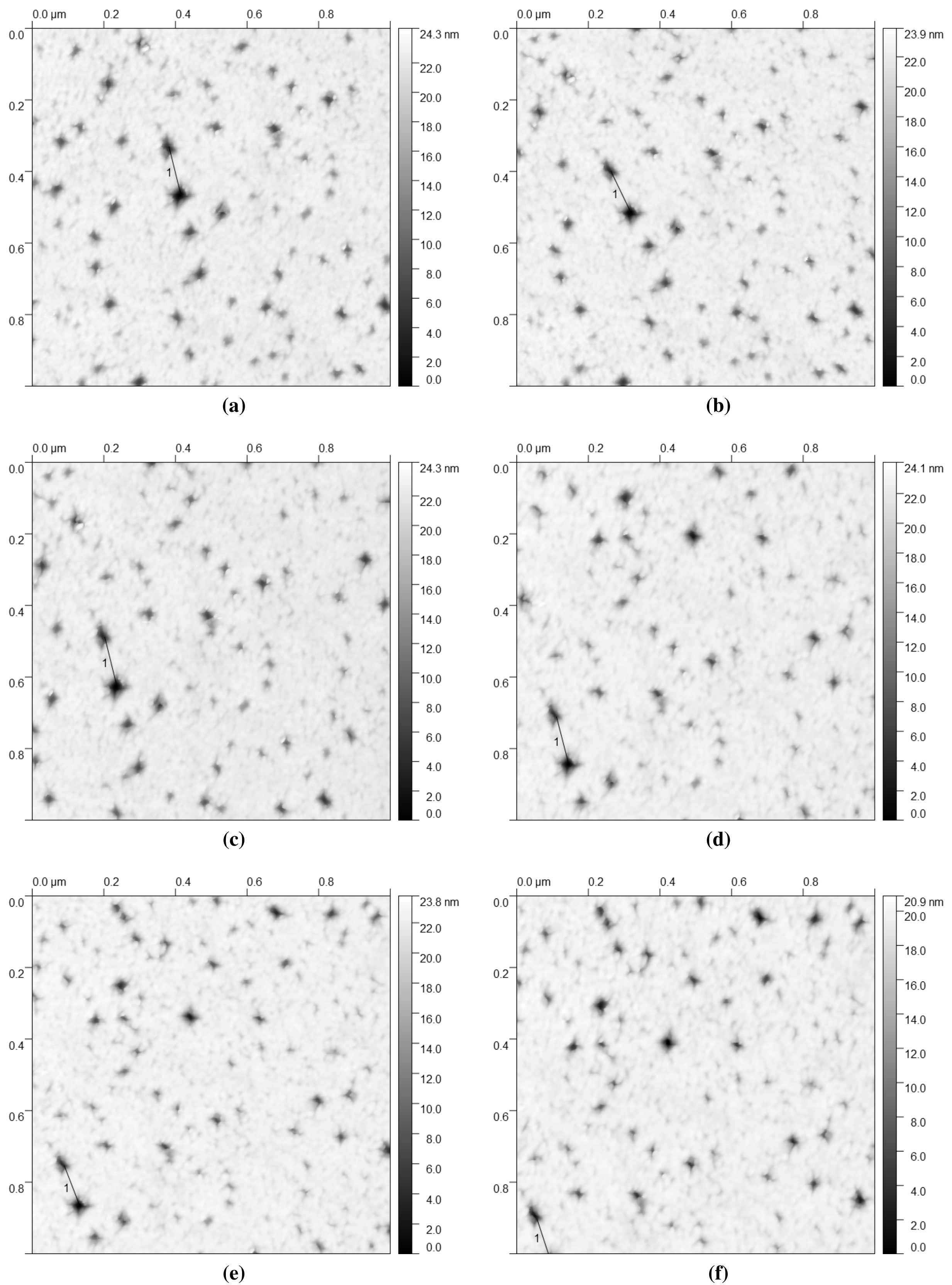

Figure 4.1: Consecutive 1 µm x 1 µm AFM images of substrate sample B from five weeks after the sample was exposed to air. Two pits are connected with a line, labelled with the number 1. Tracking this line reveals a significant drift in the images from (a) to (f). There is also a variation in the orientation of the line, indicating stretching of the images. Note also the variation in the grey scale.

The surface roughness obtained from each of the images in Figure 4.1 are presented in Table 4.1. As we can see, the values for surface roughness vary noticeably.

Table 4.1: RMS surface roughness for the AFM images of substrate sample B shown in Figure 4.1, obtained from one hour of continuous scanning, five weeks after the sample was exposed to air.

Figure 4.1	**RMS roughness,** r_s
(a)	1.96 nm
(b)	1.83 nm
(c)	1.86 nm
(d)	1.74 nm
(e)	1.73 nm
(f)	1.65 nm

A calculation of the average and uncertainty according to the method described in Section 2.1.3, yields a surface roughness for this set of scans of $r_s = 1.79 \pm 0.06$ nm.

4.2 AFM tip-related artefacts and challenges

As shown in Section 2.1.2, the resolution of the surface topography of the sample is directly tied to the geometry of the probe. It is therefore interesting to know how the tip geometry compares to the features on the sample surfaces. In the case of the substrate sample, the surface exhibited a number of deep pits, see Figure 4.2a and Figure 4.3a. By use of the line profile function in Gwyddion, a study was done on the width and depth of some of the pits on the substrate sample. Figure 4.2a shows the substrate sample on the first day of exposure to air, marked with the lines of the line profiles shown in Figure 4.2b. Figure 4.3a shows the substrate sample after 14 weeks of exposure to air, marked with the lines of the line profiles shown in Figure 4.3b. Two pits in both the AFM images of Figure 4.2 and Figure 4.3 have been studied, and there are three line profiles for each pit, oriented at $0°$, $90°$, and $45°$ with respect to the horizontal. The reason for doing line profiles at three orientations for the same pit is to get a representative image of the geometry of the pit. If we were to do line profiles at only one orientation, the shape of the pit could be affected by the geometry of the tip, and all pits would likely seem to have the same shape. The tips used in this study are ScanAsyst Air probes, and have a nominal radius of 2 nm, a maximum radius of 12 nm, and tip height between 2.5-8 µm [27].

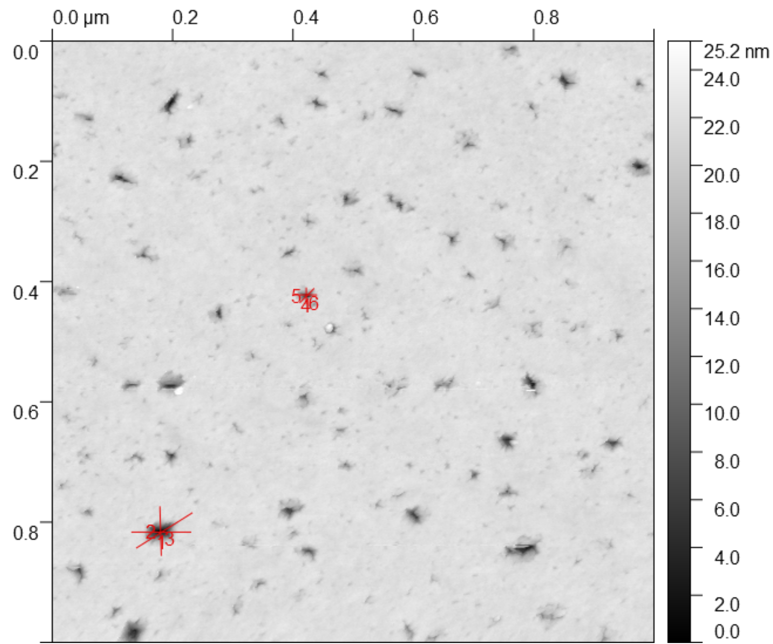

(a)

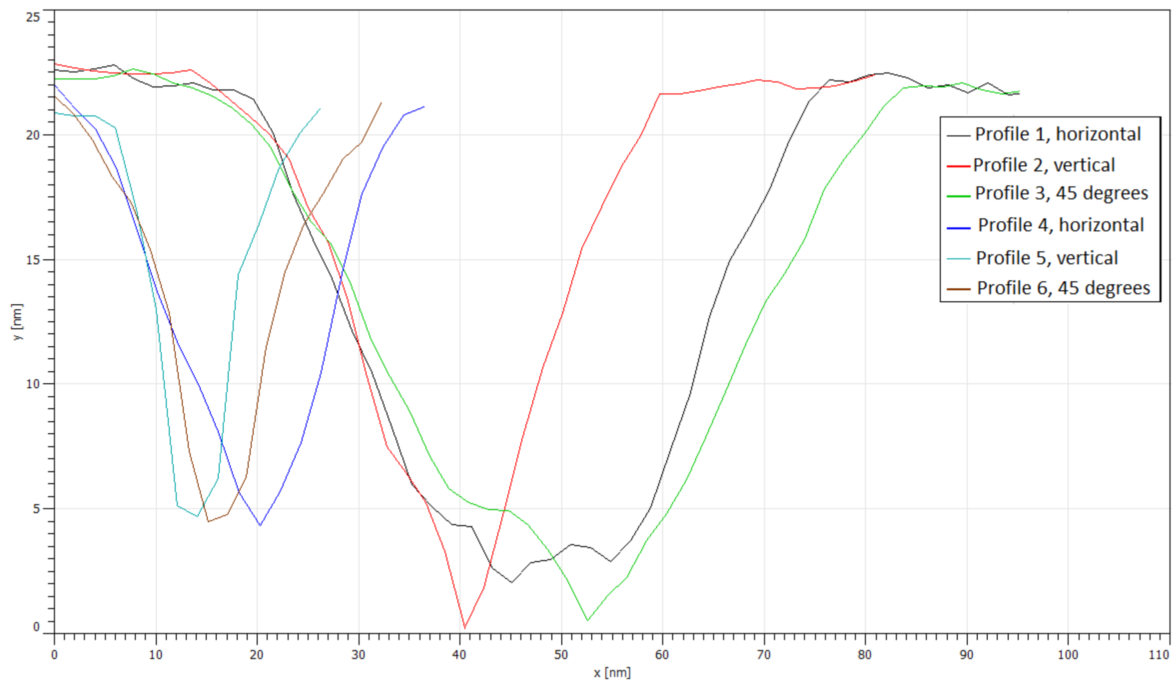

(b)

Figure 4.2: (a) 1 µm x 1 µm AFM image of substrate sample C, one day after exposure to air, with line profiles of features marked in the image. Profiles 1-3 are in the bottom left, and profiles 4-6 are in the centre. (b) The line profiles of the lines marked in (a), three profiles for each pit, with three different orientations. The y-axis indicates the height of the features in the image, and the x-axis indicates the length of the lines shown in (a).

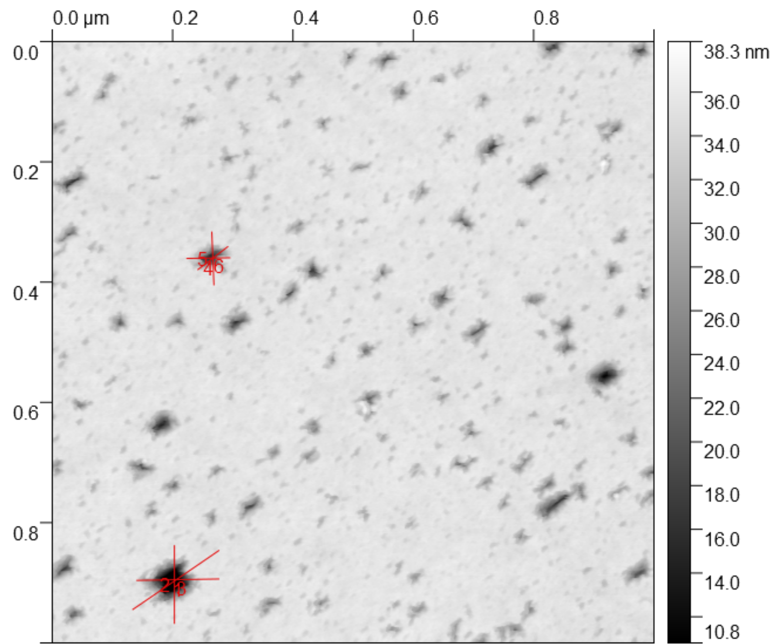

(a)

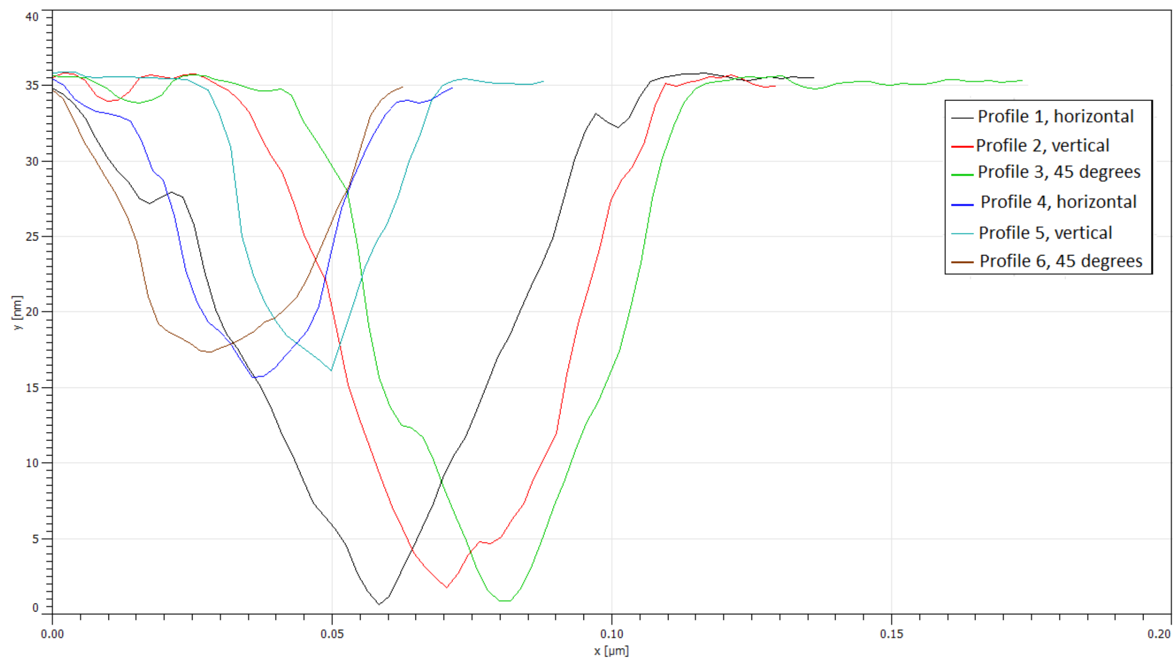

(b)

Figure 4.3: (a) 1 µm x 1 µm AFM image of substrate sample C, 14 weeks after exposure to air, with line profiles of features marked in the image. Profiles 1-3 are in the bottom left, and profiles 4-6 are in the centre. Height scale has been adjusted to give the image better contrast. (b) The line profiles of the lines marked in (a), three profiles for each pit, with three different orientations. The y-axis indicates the height of the features in the image, and the x-axis indicates the length of the lines shown in (a).

4.3 Substrate sample

4.3.1 AFM

Figure 4.4 shows six consecutive AFM images obtained right after substrate sample C was exposed to air. One scan takes about 9 minutes to complete, so this set of AFM images was obtained over the first hour of exposure to air for substrate sample C. Table 4.2 shows corresponding values for surface roughness for the images in Figure 4.4. As seen in Table 4.2, the surface roughness of substrate sample C increases noticeably during the first hour of exposure to air. From Figure 4.4, we see that there is also a small drift in the image, however, the drift is not as pronounced here as seen in Figure 4.1. We also see what appears to be deep pits all over the image.

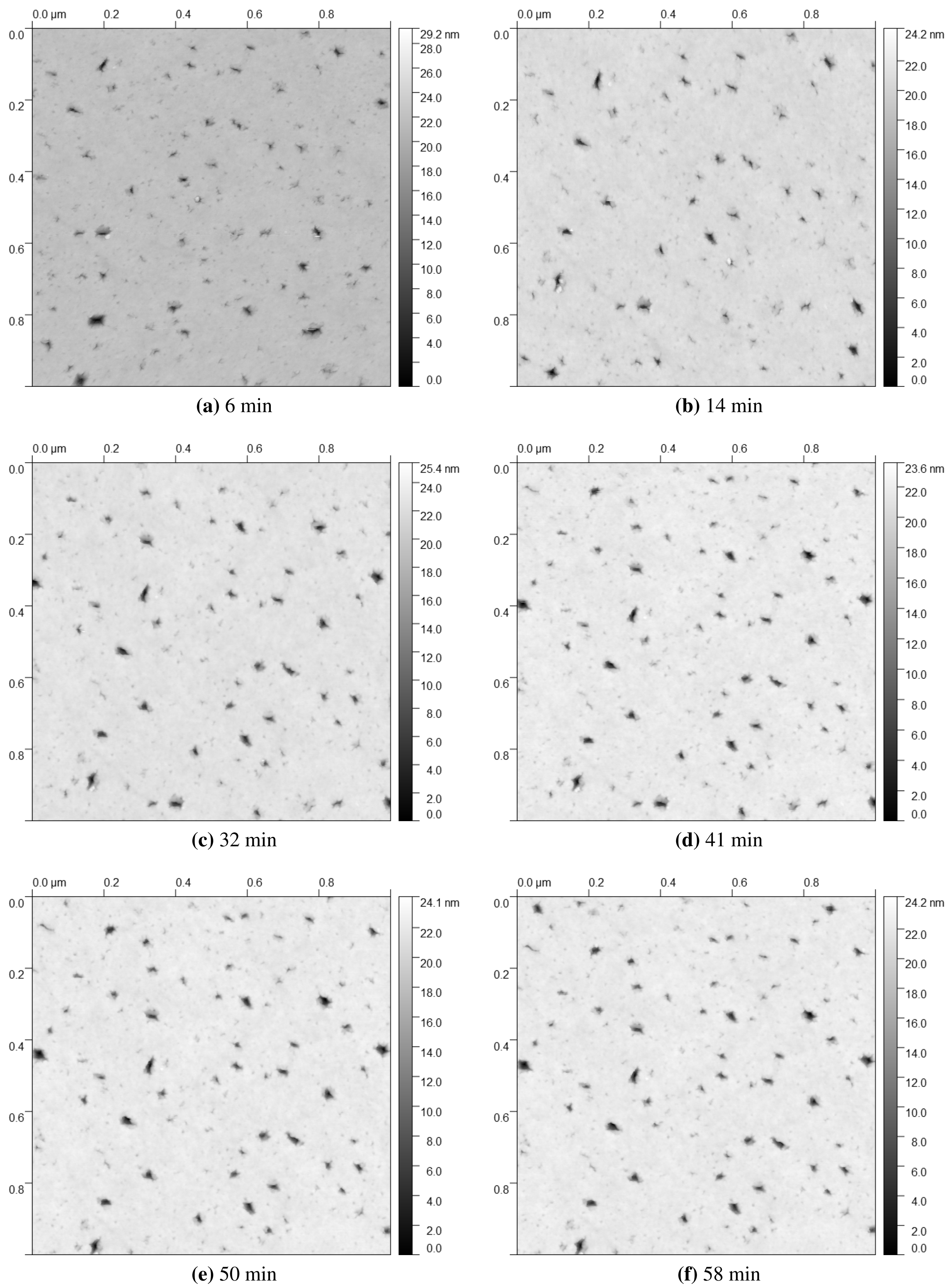

(a) 6 min

(b) 14 min

(c) 32 min

(d) 41 min

(e) 50 min

(f) 58 min

Figure 4.4: Consecutive 1 µm x 1 µm AFM images of substrate sample C taken for the first hour after exposure to air. The minutes under each image specify how long the sample had been exposed to air when that scan started. One scan takes approximately 9 minutes. One image was not saved during scanning, causing the gap in time between (b) and (c).

Table 4.2: RMS surface roughness from the images in Figure 4.4 of substrate sample C obtained for the first hour after exposure to air.

Figure 4.4	**Time after exposure to air**	**RMS surface roughness,** r_s
(a)	6 min	1.29 nm
(b)	14 min	1.24 nm
(c)	32 min	1.51 nm
(d)	41 min	1.57 nm
(e)	50 min	1.60 nm
(f)	58 min	1.61 nm

Figure 4.5 shows images of the substrate sample obtained in the weeks following the exposure of the substrate sample to air. Since multiple scans were done each time the samples were measured, the images in 4.5 are representative images from each of the sets of images obtained. Table 4.3 shows the corresponding values for surface roughness for the images in Figure 4.5. The values for surface roughness are calculated from the sets of AFM images according to the method described in Section 2.1.3. Figure 4.5 shows the same deep pits on the substrate surface as seen in Figure 4.4, with variation from image to image in number and size of the pits, and the height scale of the images. A quick count indicates around 45 pits per μm^2 on average. Table 4.3 indicates large differences in the surface roughness between the three samples that were measured, most noticeably the measurement in week 6 for substrate sample B.

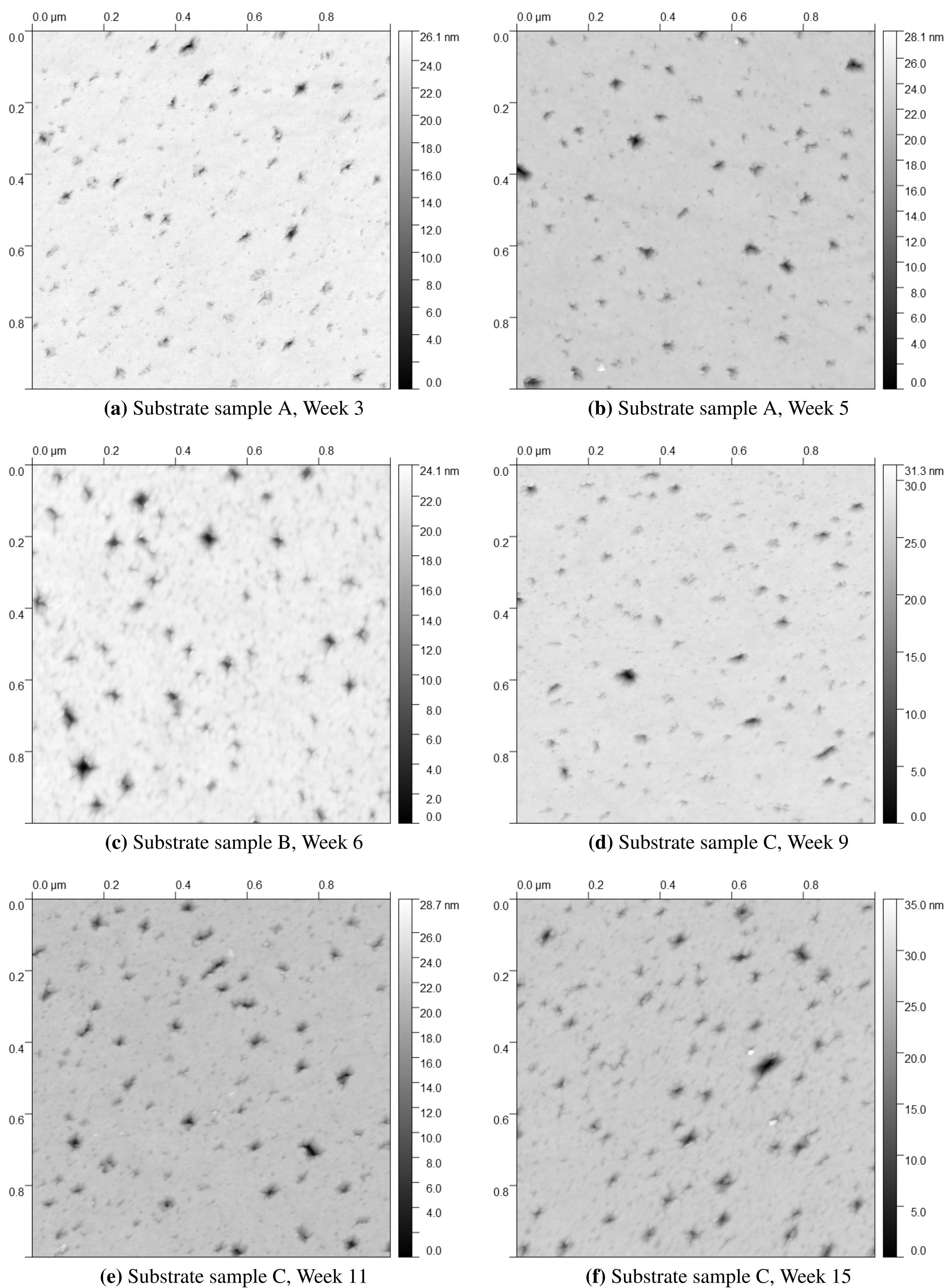

(a) Substrate sample A, Week 3

(b) Substrate sample A, Week 5

(c) Substrate sample B, Week 6

(d) Substrate sample C, Week 9

(e) Substrate sample C, Week 11

(f) Substrate sample C, Week 15

Figure 4.5: 1 µm x 1 µm AFM images of the substrate sample obtained in the weeks after exposure to air. Note that these are images from three different samples, and note the variation in the grey scale.

Table 4.3: RMS surface roughness for scans of the substrate sample obtained in the weeks after exposure to air. Values are calculated from the set of images obtained from each laboratory session. Values correspond to the images in Figure 4.5.

Sample	Figure 4.5	RMS surface roughness, r_s
Substrate A	(a) Week 3	1.41 ± 0.06 nm
Substrate A	(b) Week 5	1.17 ± 0.09 nm
Substrate B	(c) Week 6	1.79 ± 0.06 nm
Substrate C	(d) Week 9	1.46 ± 0.05 nm
Substrate C	(e) Week 11	1.57 ± 0.04 nm
Substrate C	(f) Week 15	1.98 ± 0.06 nm

Figure 4.6 shows a 50 μm x 50 μm image of substrate sample C, 9 weeks after exposure to air. The pits are still visible on the surface as tiny black dots. The vertical range (grey scale) for this image is significantly lower than for the 1 μm^2 AFM images seen in Figure 4.4 and Figure 4.5. The RMS surface roughness for the AFM image in Figure 4.6 is 0.44 nm, also significantly lower than for the 1 μm^2 images of the substrate sample.

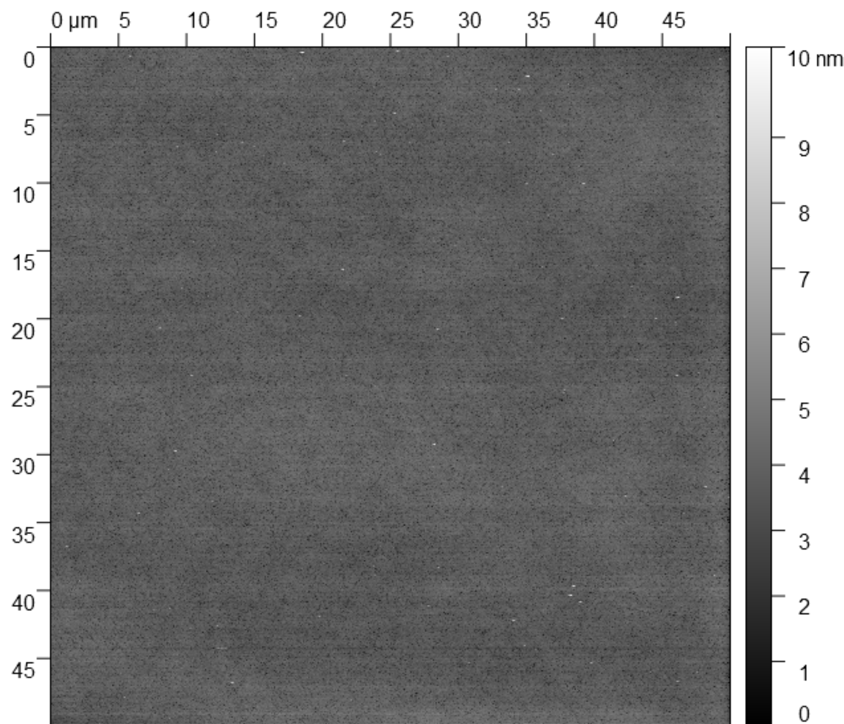

Figure 4.6: 50 μm x 50 μm AFM image of substrate sample C from 9 weeks after exposure to air. The vertical range for this image is 10.4 nm, which is significantly lower than the 25-30 nm vertical ranges for the 1 μm^2 AFM images of the substrate sample. The RMS surface roughness for this image is 0.44 nm. This indicates that increasing the scan area lowers the vertical range, and the surface roughness.

4.3.2 VASE

Figure 4.7 shows the measured and modelled imaginary part of the pseudo dielectric function, $\langle \varepsilon_2 \rangle$, for substrate sample B for the first 240 minutes after exposure to air. The plot also includes $\langle \varepsilon_2 \rangle$ for GaAs for comparison. This plot was obtained by using Model 1 (see Section 3.5), a model that includes a GaAs substrate, and an EMA overlayer composed of 50% GaAs and 50% void. The model was chosen due to it's MSE being the lowest of the attempted models, see Appendix B. The MSE for this model for this data set was 2.572. Figure 4.8 shows $\langle \varepsilon_2 \rangle$ for the two layers in Model 1, the GaAs substrate and the EMA layer. Figure 4.9 shows the evolution of the EMA layer thickness as a function of time for the first 240 minutes after substrate sample B was exposed to air. The thickness is calculated by fitting Model 1 to the data set of measurements.

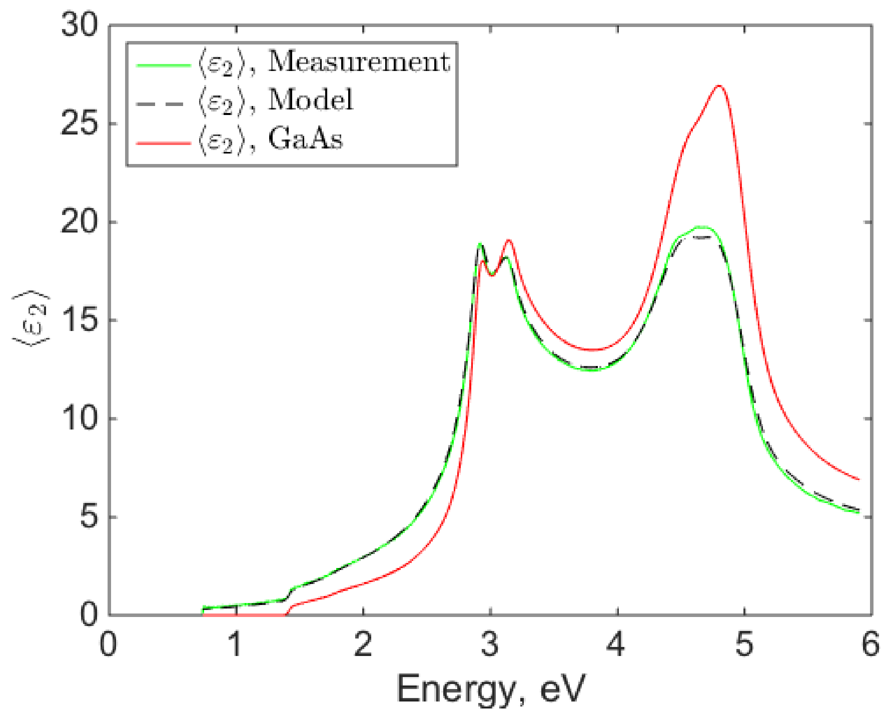

Figure 4.7: Imaginary part of the pseudo dielectric function, $\langle \varepsilon_2 \rangle$, at 65° angle of incidence for substrate sample B, for the first 240 minutes after exposure to air. Green line is the measured $\langle \varepsilon_2 \rangle$, the black dashed line is the modelled $\langle \varepsilon_2 \rangle$, and the red line is $\langle \varepsilon_2 \rangle$ for GaAs, plotted for comparison. The model consists of a GaAs substrate with an EMA overlayer of 50% GaAs and 50% void. X-axis denotes the energy of the incident light in eV, and y-axis is in arbitrary units. MSE for the model for this set of measurements was 2.572

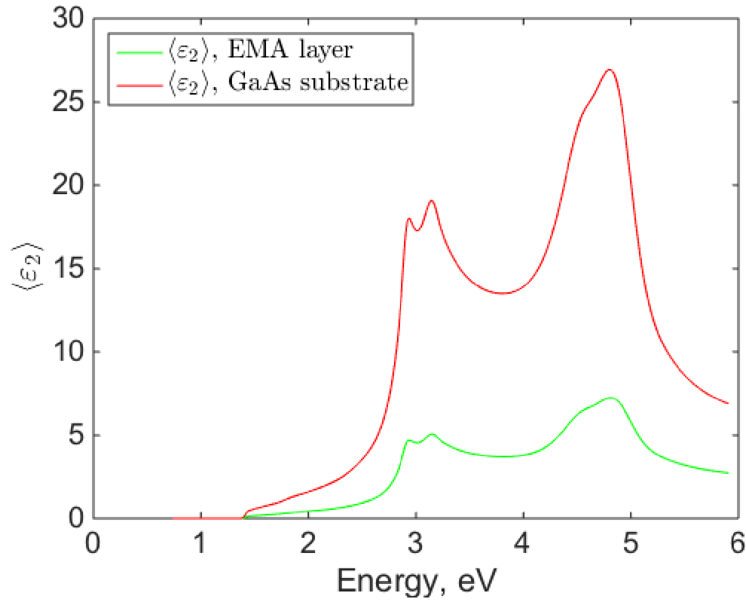

Figure 4.8: $\langle\varepsilon_2\rangle$ for each individual layer in the optical model used to model substrate sample B for the first 240 minutes after exposure to air. Green line is the EMA layer of 50% GaAs and 50% void, red line is the GaAs substrate. We see that $\langle\varepsilon_2\rangle$ for the EMA layer has the same shape as $\langle\varepsilon_2\rangle$ for GaAs, only lower and smoother. X-axis denotes the energy of the incident light in eV, and y-axis is in arbitrary units.

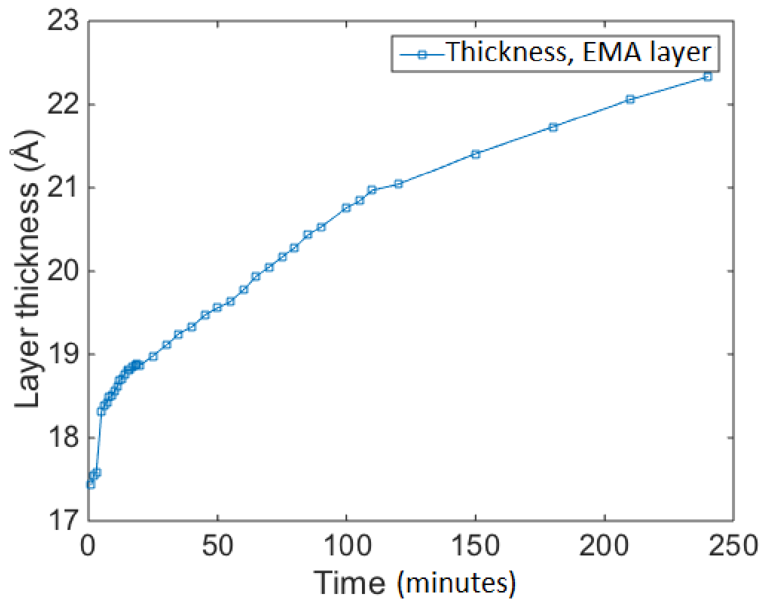

Figure 4.9: Evolution of the EMA layer thickness for substrate sample B for the first 240 minutes after exposure to air, calculated using Model 1 described in Section 3.5. The model consists of a GaAs substrate with an EMA overlayer of 50% GaAs and 50% void. X-axis denotes time after exposure to air in minutes, y-axis is the thickness of the EMA layer given in Å.

We see from Figure 4.7 that the model fits quite well with the measurements. The exception is around the peak at approximately 4.6 eV, and above 5 eV, where there is a slight difference between the model and the measurement. This is the energy range for which the measurements are most sensitive to the sample surface. Figure 4.8 shows that $\langle\varepsilon_2\rangle$ for the EMA layer that consists of 50% GaAs and 50% void has approximately the same shape as $\langle\varepsilon_2\rangle$ for GaAs, but it has been lowered in value, and smoothened. Figure 4.9 shows an increasing thickness of the EMA layer for the first 240 minutes after exposing the sample to air.

Figure 4.10 shows the measured and modelled $\langle\varepsilon_2\rangle$ for the substrate sample, from 1 to 12 weeks after exposure to air. $\langle\varepsilon_2\rangle$ for GaAs is also plotted for comparison. The plot was obtained by using Model 6 described in Section 3.5 to model the measurements. The model is a GaAs substrate with two overlayers: first a GaAs oxide layer, and then an EMA layer consisting of 50% GaAs oxide and 50% void. This model was chosen based on it having the lowest MSE of the attempted models, see Appendix B. The MSE for this model for this set of measurements was 4.253. Figure 4.11 shows $\langle\varepsilon_2\rangle$ for the three layers in Model 6: the GaAs substrate, the GaAs oxide layer, and the EMA layer. Figure 4.12 shows the evolution of the thicknesses of the two overlayers as a function of time.

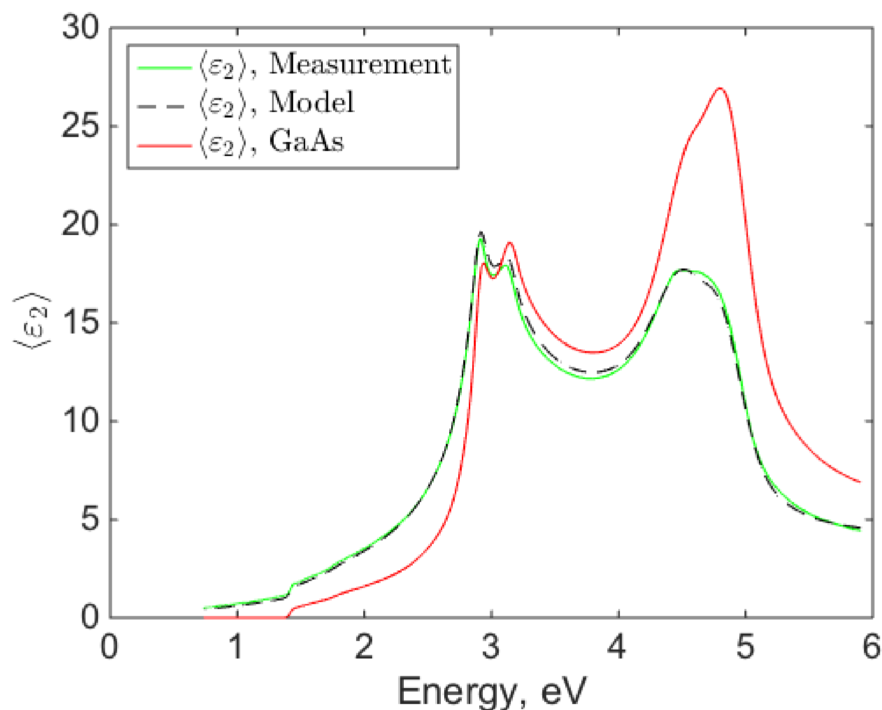

Figure 4.10: Imaginary part of the pseudo dielectric function, $\langle\varepsilon_2\rangle$, at 65° angle of incidence for substrate sample B, 1-12 weeks after exposure to air. Green line is the measured $\langle\varepsilon_2\rangle$, the black dashed line is the modelled $\langle\varepsilon_2\rangle$, and the red line is $\langle\varepsilon_2\rangle$ for GaAs, plotted for comparison. The model is a GaAs substrate with two overlayers, a GaAs oxide layer and an EMA layer consisting of 50% GaAs oxide and 50% void. X-axis denotes the energy of the incident light in eV, and y-axis is in arbitrary units. MSE for the model for this set of measurements was 4.253.

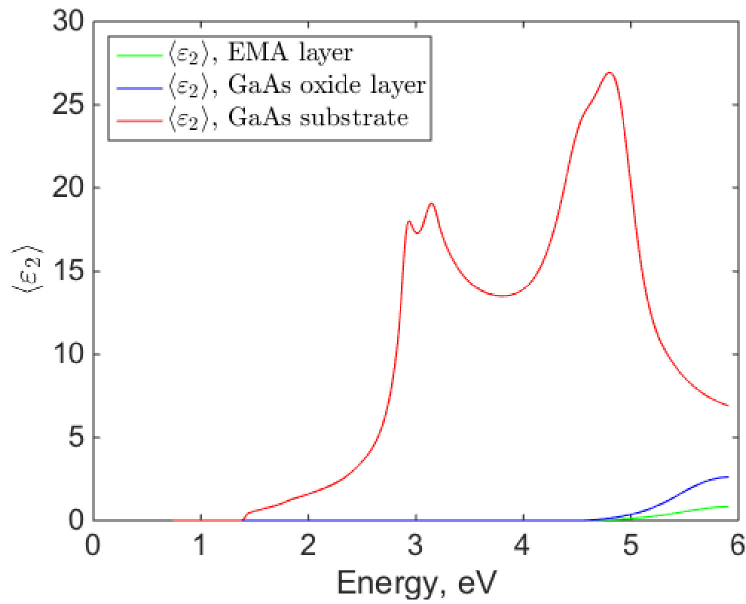

Figure 4.11: $\langle \varepsilon_2 \rangle$ for each individual layer in the optical model used to model substrate sample B, 1-12 weeks after exposure to air. Green line is the EMA layer consisting of 50% GaAs oxide and 50% void, blue line is the GaAs oxide layer, and the red line is the GaAs substrate. We see that $\langle \varepsilon_2 \rangle$ for the GaAs oxide and the EMA layer give contributions only at energies above 4.8 eV, which is the surface sensitive energy range. X-axis denotes the energy of the incident light in eV, and y-axis is in arbitrary units.

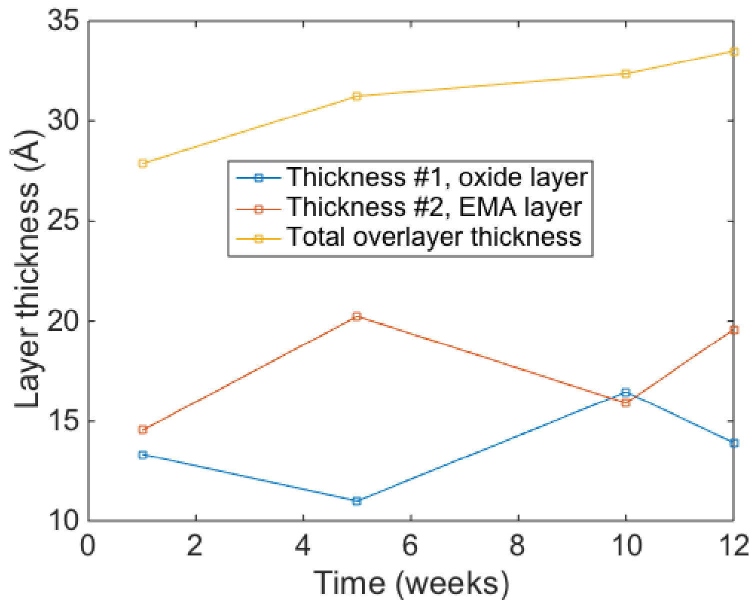

Figure 4.12: Evolution of layer thickness for substrate sample B from week 1 to week 12 after exposure to air, calculated using Model 6 described in Section 3.5, which consists of a GaAs substrate with two overlayers: a GaAs oxide layer and an EMA overlayer of 50% GaAs oxide and 50% void. Blue line is the thickness of the oxide layer, red line is the thickness of the EMA layer, and the yellow line is the sum of the thicknesses of the two overlayers. X-axis denotes time after exposure to air in weeks, y-axis is the thickness of the EMA and oxide layer given in Å.

Figure 4.10 indicates that the model fits fairly well with the measurements up to about 3 eV. Above 3 eV the fit is slightly poorer, and this is also indicated by the MSE of 4.253, which is relatively high compared to the MSE of 2.572 obtained for the first 240 minutes. Figure 4.11 shows that $\langle \varepsilon_2 \rangle$ for GaAs oxide and the EMA layer of 50% GaAs oxide and 50% void differs vastly from $\langle \varepsilon_2 \rangle$ for GaAs, and gives contribution to the total $\langle \varepsilon_2 \rangle$ only above 4.7 eV. This is the energy range where the measurements are most sensitive to the sample surface. Figure 4.12 indicates that the oxide layer and EMA layer have some inversely proportional behaviour, but that the total overlayer thickness increases over time.

4.4 Buffer sample

4.4.1 AFM

As mentioned, no AFM images were obtained during the first two days after the buffer sample was removed from the MBE machine. The sample stayed in the sample box during these two days, but we cannot be certain that the sample box is completely air tight, so I will refer to the days after removal from the MBE machine as ”days after exposure to air”. Figure 4.13 shows five images taken in the course of about one hour on day 3 after exposing buffer sample A to air. Table 4.4 shows the corresponding RMS roughness values obtained in Gwyddion for each of the images in Figure 4.13. As with the substrate sample, we also see a little bit of drift in the consecutive images shown in Figure 4.13, however it is not as prominent as shown in Figure 4.1. The measured surface roughness listed in Table 4.4 also stays somewhat consistent, only varying slightly around 0.35 nm.

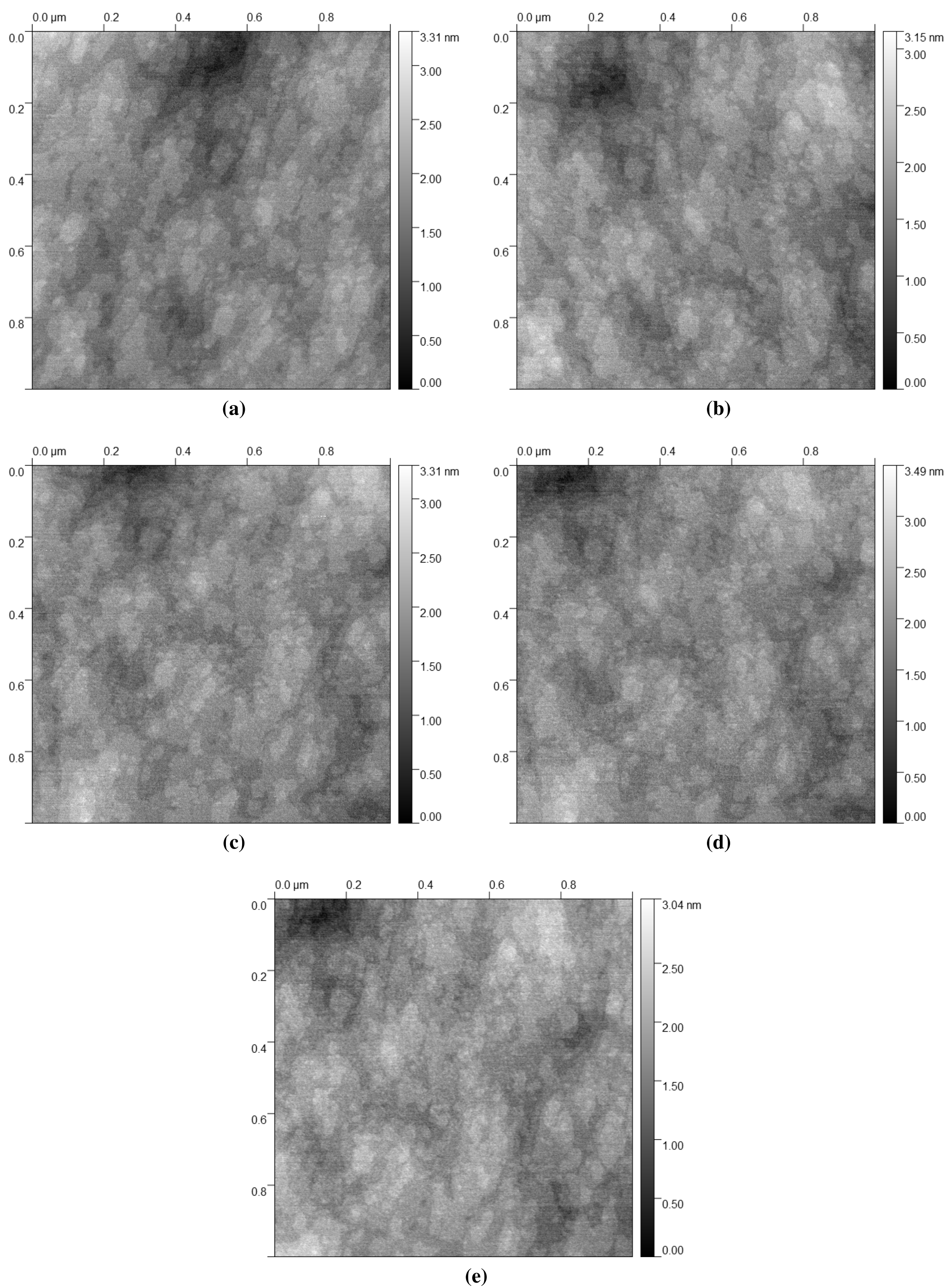

Figure 4.13: Consecutive 1 µm x 1 µm AFM images of buffer sample A taken over the course of one hour, three days after exposure to air. Note that there is some drift in the images. There is a slight variation in the grey scale.

Table 4.4: RMS surface roughness for images of buffer sample A obtained three days after exposure to air. Values correspond to the images in Figure 4.13.

Figure 4.13	**RMS surface roughness**
(a)	0.35 nm
(b)	0.35 nm
(c)	0.33 nm
(d)	0.37 nm
(e)	0.33 nm

Figure 4.14 shows AFM images of buffer sample A for the 8 weeks following the sample being exposed to air. Surface roughness for each image is shown in Table 4.5. The surface roughness has decreased slightly from day three, but remains relatively close to 0.30 nm for the eight weeks following exposure to air. The surface roughness is also significantly smaller for the buffer sample than it was for the substrate sample, and there are no deep and narrow pits in the image.

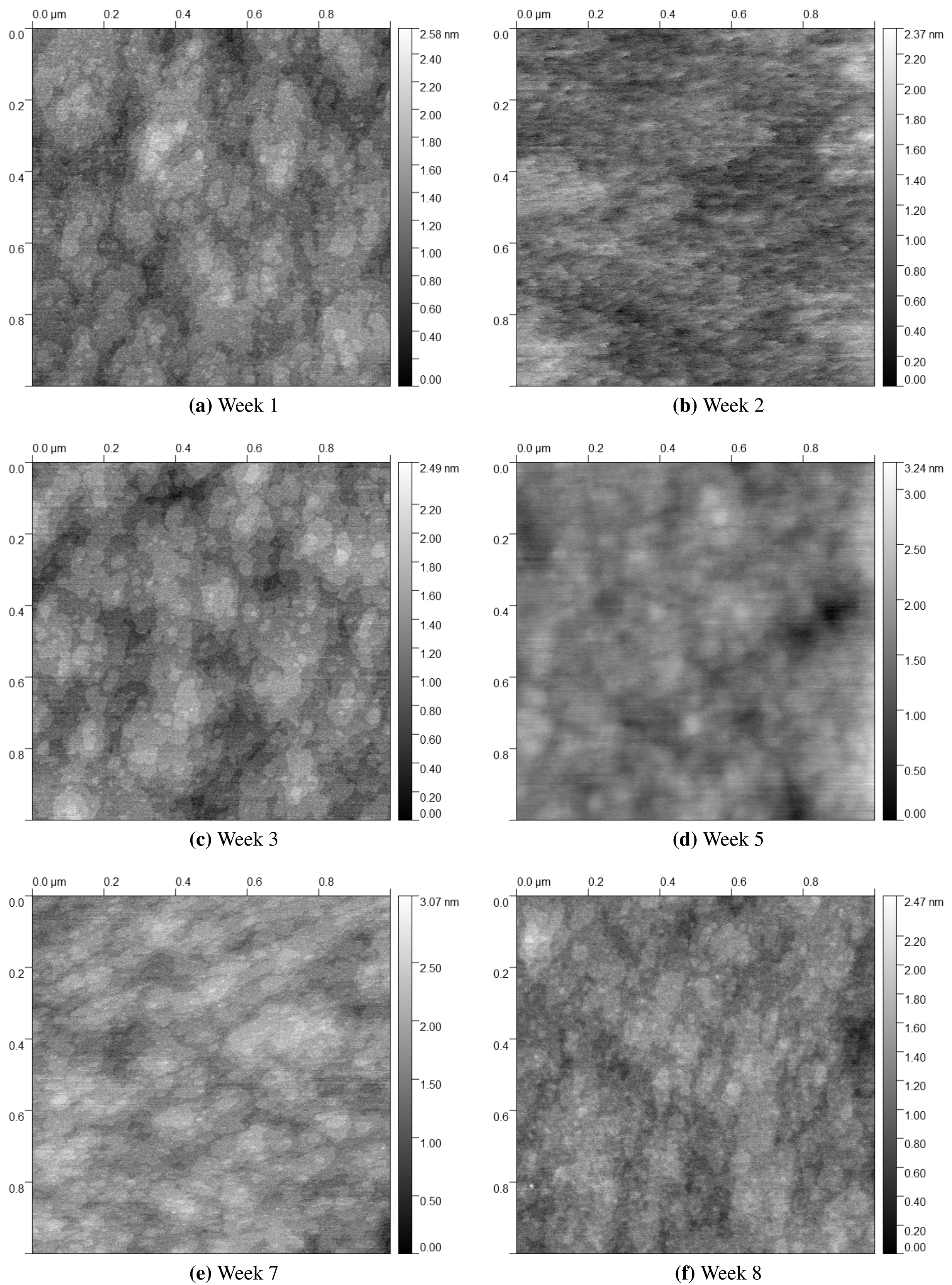

(a) Week 1 **(b)** Week 2

(c) Week 3 **(d)** Week 5

(e) Week 7 **(f)** Week 8

Figure 4.14: 1 µm x 1 µm AFM images of buffer sample A from the weeks following the sample being exposed to air. The images in (b) and (d) are visibly blurred, a result of the AFM probe tip being damaged. Note the variations in the grey scale.

Table 4.5: Surface roughness measurements obtained for buffer sample A in the weeks following exposure to air. Values are calculated from the set of images obtained during each laboratory session, and correspond to the images in Figure 4.14.

Figure 4.14	RMS roughness
(a) Week 1	0.28 ± 0.01 nm
(b) Week 2	0.29 ± 0.02 nm
(c) Week 3	0.28 ± 0.01 nm
(d) Week 5	0.33 ± 0.02 nm
(e) Week 7	0.31 ± 0.00 nm
(f) Week 8	0.26 ± 0.01 nm

Some of the images in Figure 4.14 appear to be blurred, but visible in the images both in Figure 4.13 and Figure 4.14 is a terrace-like structure. Figure 4.15 shows a 500 nm x 500 nm AFM image of buffer sample A, 3 weeks after exposure to air, along with the line profile for the line marked in the AFM image. The line profile has the step heights between neighbouring terraces marked in the image, and the values are calculated using the average values for the terraces. Figure 4.16 also shows an AFM image of buffer sample A and a line profile, from 3 weeks after exposure to air, but this is a 1 µm x 1 µm scan, and the line profile stretches over a much longer distance. The step height between some of the neighbouring terraces is noted in Figure 4.16b, and these steps are also calculated using the average height for the terraces.

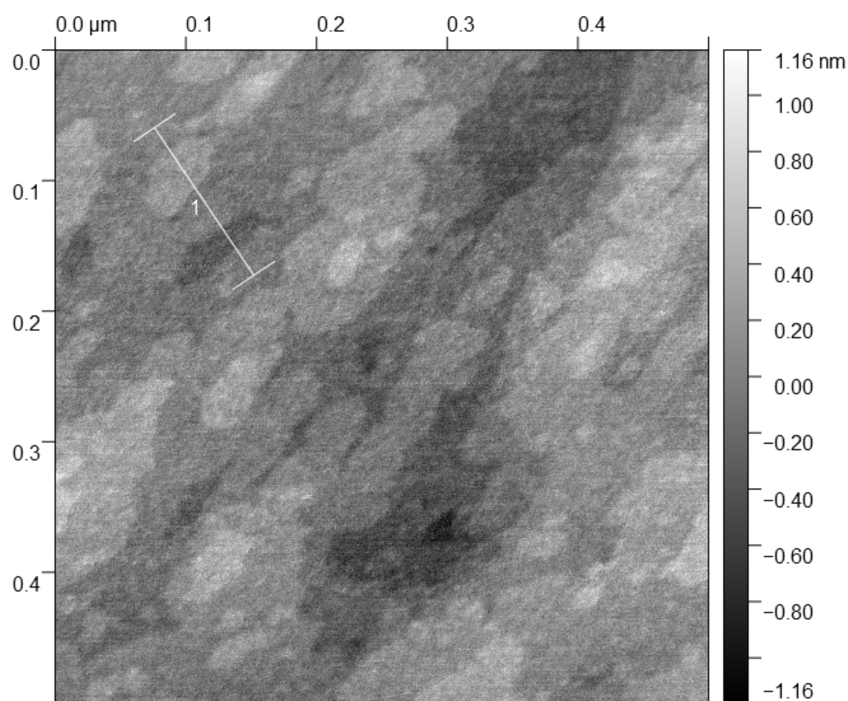

(a)

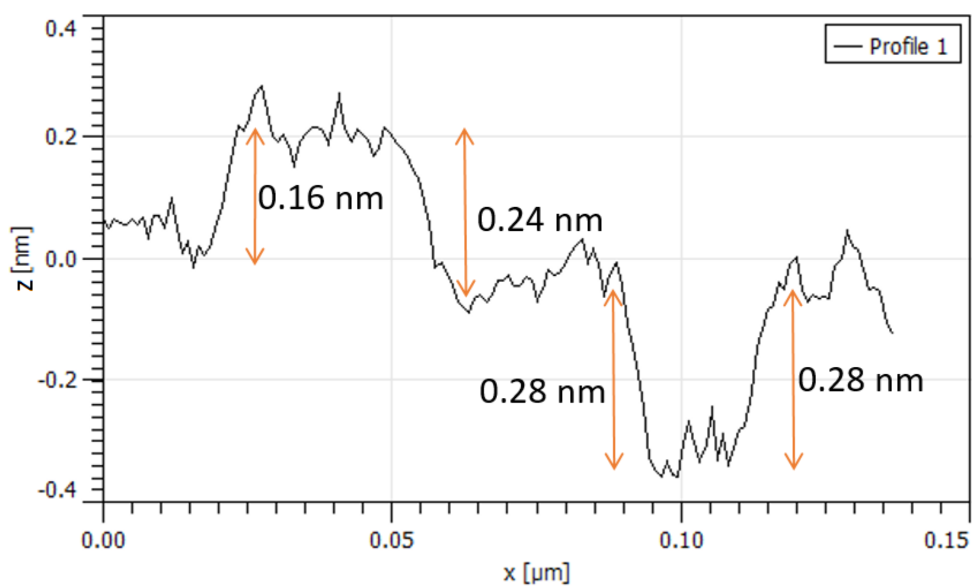

(b)

Figure 4.15: (a) 500 nm x 500 nm AFM image of buffer sample A with a line profile marked in the image. The image grey scale has been adjusted for better contrast. (b) The line profile with the step values between neighbouring terraces noted in the image. Step heights are calculated using the average height of the terraces. Z-axis is the height profile, and x-axis is the length of the line profile.

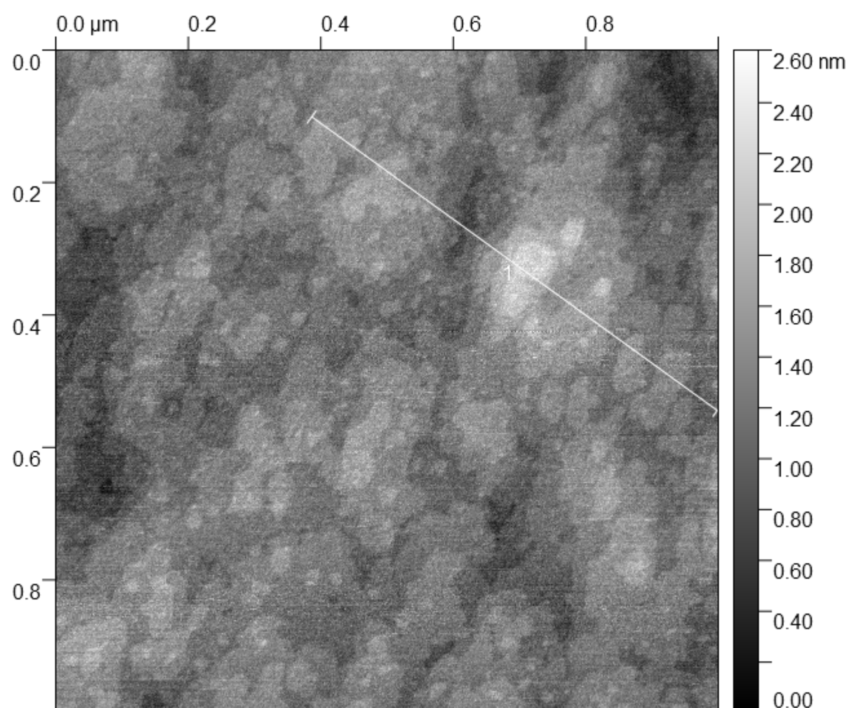

(a)

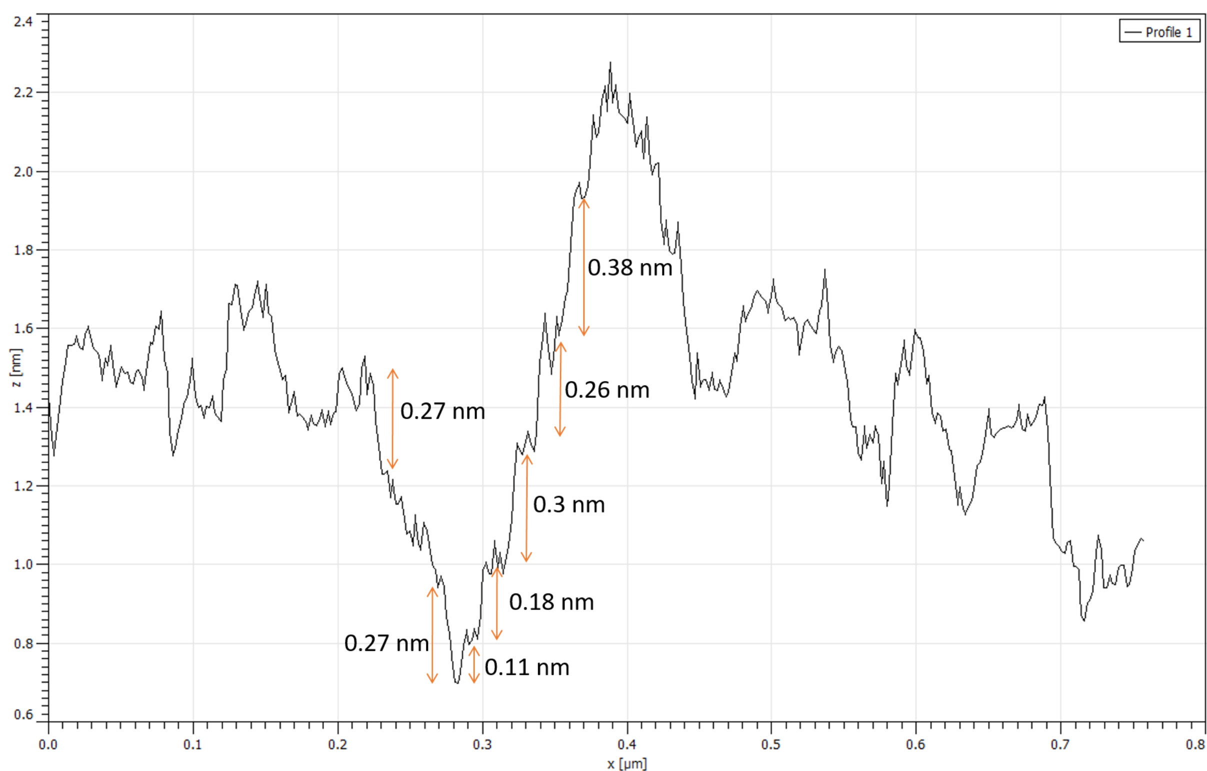

(b)

Figure 4.16: (a) 1 µm x 1 µm AFM image of buffer sample A with a line profile marked in the image. (b) The line profile with the step values between some of the neighbouring terraces noted in the image. Step heights are calculated using the average height of the terraces. Z-axis is the height profile, and x-axis is the length of the line profile.

4.4.2 Optical profilometer

For the buffer sample, some scans were also performed using the optical profiler. Figure 4.17 and Figure 4.18 show 3D images from the optical profiler of buffer sample A and B from 9 weeks after exposure to air.

The measured RMS roughness using the optical profiler was 0.39 nm for buffer sample A in Figure 4.17, and 0.36 nm for buffer sample B in Figure 4.18. These values are slightly higher than the surface roughness obtained from the AFM images of the buffer sample.

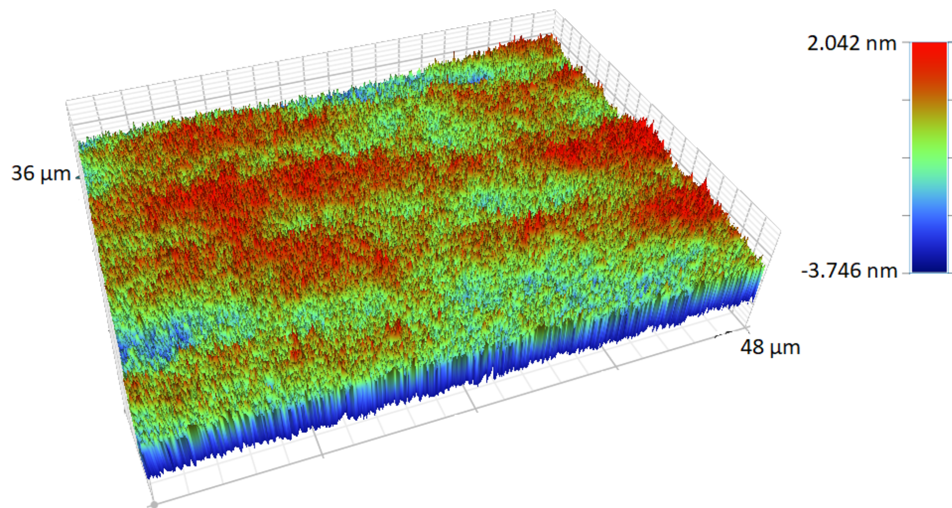

Figure 4.17: 3D view of the optical profilometer image for buffer sample A, the AFM sample, 9 weeks after exposure to air. Calculated RMS surface roughness for this scan was 0.39 nm.

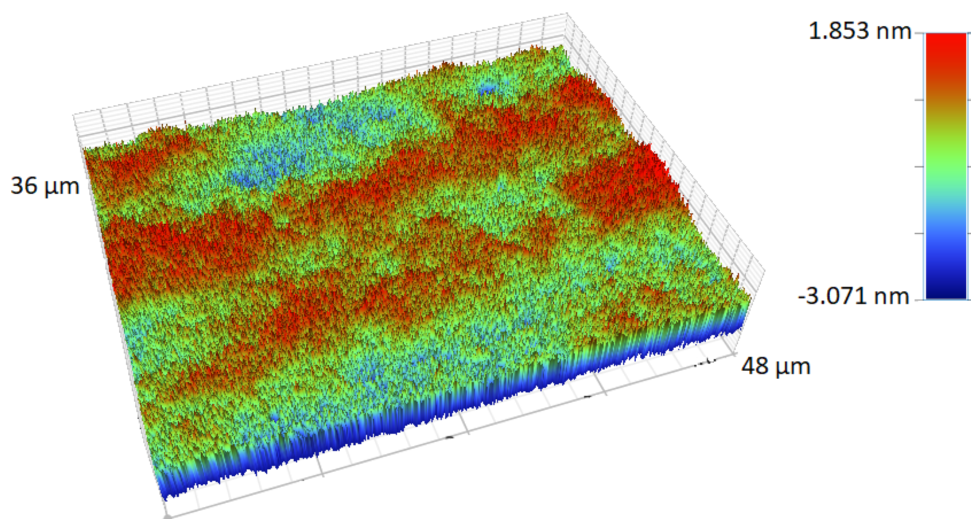

Figure 4.18: 3D view of the optical profilometer image for buffer sample B, the VASE sample, 9 weeks after exposure to air. Calculated surface roughness for this scan was 0.36 nm.

4.4.3 VASE

Figure 4.19 shows the measured and modelled imaginary part of the pseudo dielectric function, $\langle\varepsilon_2\rangle$, for buffer sample B, 3-180 minutes after exposure to air. $\langle\varepsilon_2\rangle$ for GaAs is also plotted in the figure for comparison. The plot is obtained using Model 7 described in Section 3.5, which consists of a GaAs substrate with a GaAs oxide layer. The model was chosen due to it having the lowest MSE for this set of measurements, an MSE of 2.016. Figure 4.20 shows $\langle\varepsilon_2\rangle$ for each individual layer of Model 7, the GaAs substrate and the GaAs oxide layer. The evolution of the oxide layer thickness for this set of measurements was plotted as a function of time, and can be found in Figure 4.21.

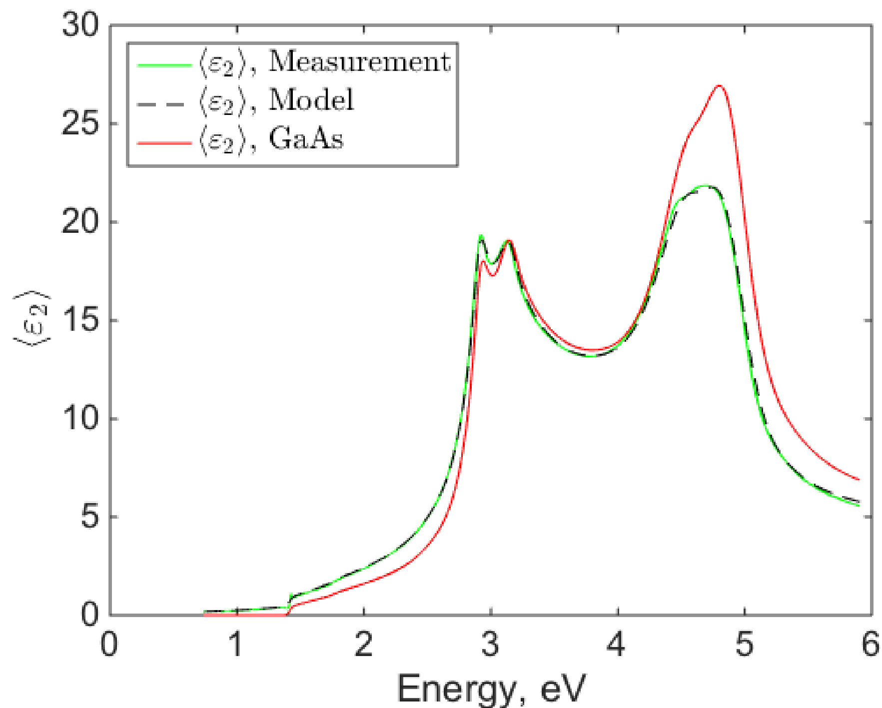

Figure 4.19: Imaginary part of the pseudo dielectric function, $\langle\varepsilon_2\rangle$, at 65° angle of incidence for buffer sample B, 3-180 minutes after exposure to air. Green line is the measured $\langle\varepsilon_2\rangle$, the black dashed line is the modelled $\langle\varepsilon_2\rangle$, and the red line is $\langle\varepsilon_2\rangle$ for GaAs, plotted for comparison. The model is a GaAs substrate with a GaAs oxide layer. X-axis denotes the energy of the incident light in eV, and y-axis is in arbitrary units. MSE for the model for this set of measurements was 2.016.

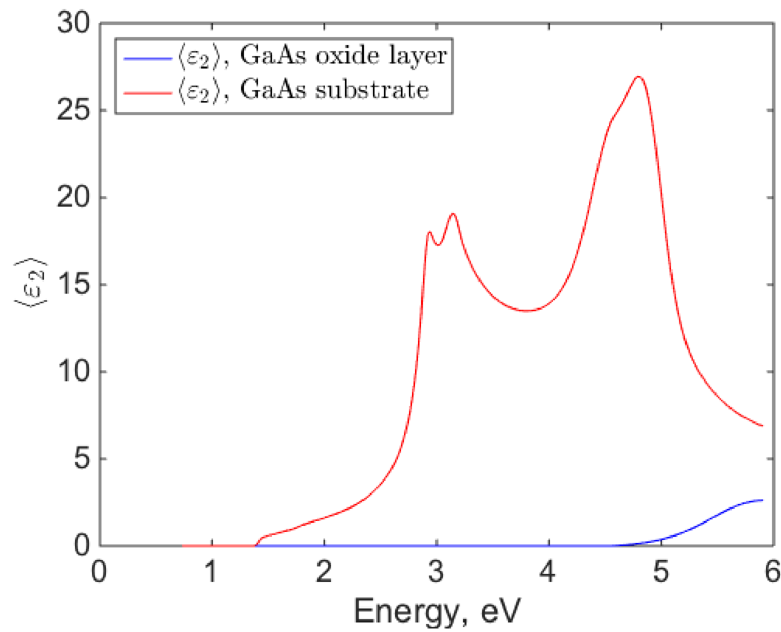

Figure 4.20: $\langle \varepsilon_2 \rangle$ for the two individual layers in the optical model used to model buffer sample B, 3-180 minutes after exposure to air. The blue line is $\langle \varepsilon_2 \rangle$ for the GaAs oxide layer, the red line is $\langle \varepsilon_2 \rangle$ for the GaAs substrate. GaAs oxide contributes to $\langle \varepsilon_2 \rangle$ only at energies above 4.8 eV, which is the surface sensitive energy range. X-axis denotes the energy of the incident light in eV, and y-axis is in arbitrary units.

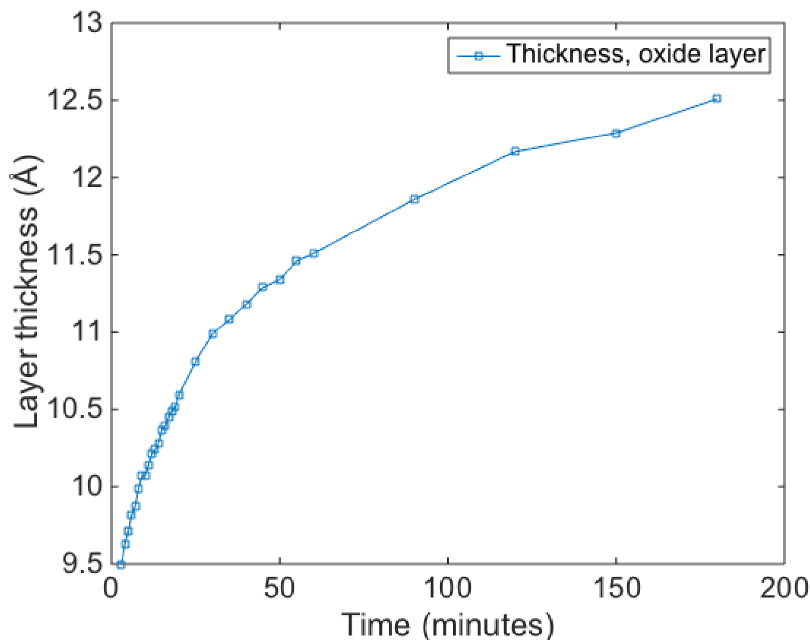

Figure 4.21: Evolution of the oxide layer thickness of buffer sample B, for the first 180 minutes after exposure to air, obtained by using Model 7 described in Section 3.5. The x-axis denotes time in minutes, and the y-axis denotes layer thickness in Å.

Figure 4.22 shows the measured and modelled $\langle\varepsilon_2\rangle$ for buffer sample B, from 26 hours to 4 weeks after exposure to air, as well as $\langle\varepsilon_2\rangle$ for GaAs. The plot is obtained using Model 6 described in Section 3.5, which consists of a GaAs substrate with two overlayers: a GaAs oxide layer and an EMA layer of 50% GaAs oxide and 50% void. The model was chosen due to it having the lowest MSE for this set of measurements, an MSE of 2.281. Figure 4.23 shows $\langle\varepsilon_2\rangle$ for each individual layer in Model 6, the GaAs substrate, the GaAs oxide layer, and the EMA layer. The evolution of the layer thicknesses for this set of measurements can be found in Figure 4.24

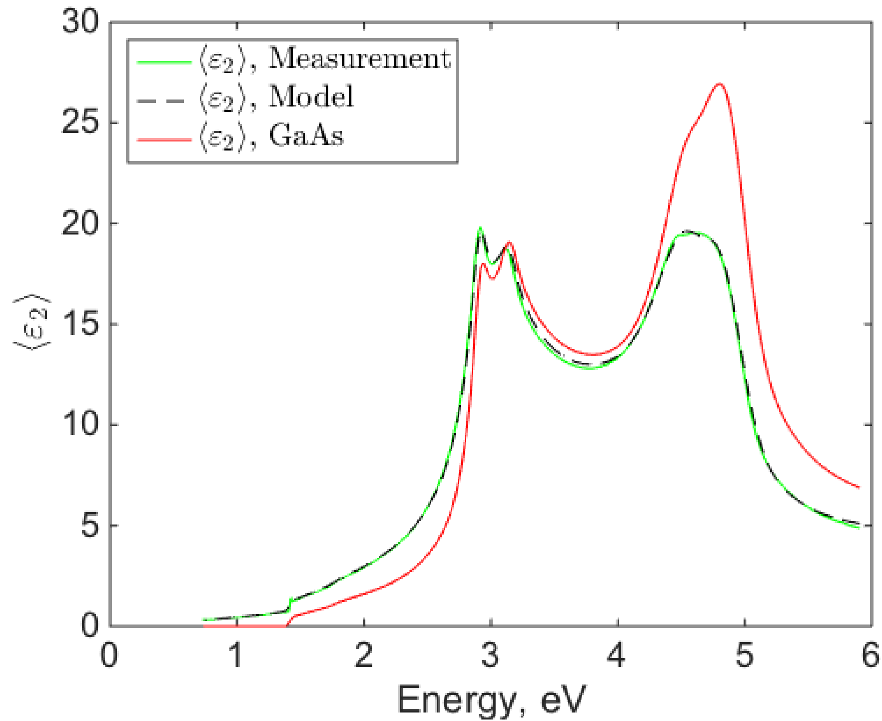

Figure 4.22: Imaginary part of the pseudo dielectric function, $\langle\varepsilon_2\rangle$, at 65° angle of incidence for buffer sample B, 26 hours to 4 weeks after exposure to air. Green line is the measured $\langle\varepsilon_2\rangle$, the black dashed line is the modelled $\langle\varepsilon_2\rangle$, and the red line is $\langle\varepsilon_2\rangle$ for GaAs, plotted for comparison. X-axis denotes the energy of the incident light in eV, and y-axis is in arbitrary units. MSE for this model for this set of measurements was 2.281.

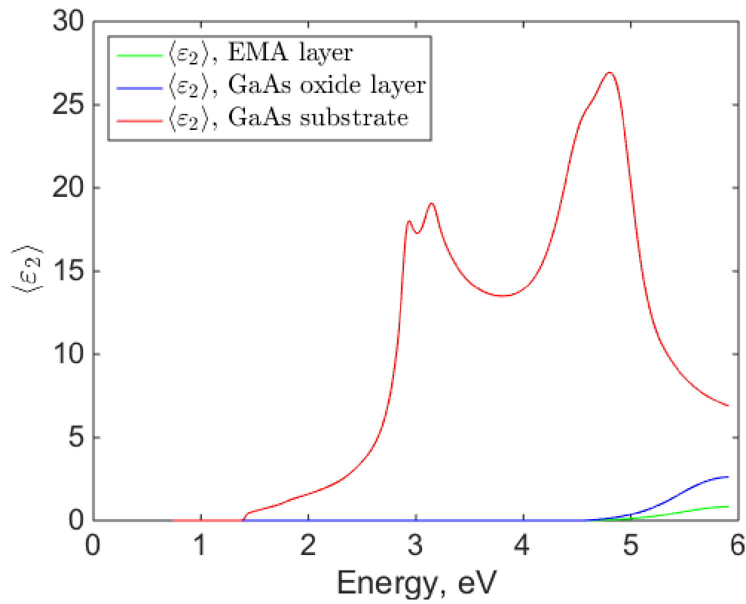

Figure 4.23: $\langle\varepsilon_2\rangle$ for each individual layer in the optical model used to model buffer sample B, 26 hours to 4 weeks after exposure to air. Green line is the EMA layer consisting of 50% GaAs oxide and 50% void, blue line is the GaAs oxide layer, and the red line is the GaAs substrate. We see that $\langle\varepsilon_2\rangle$ for the GaAs oxide and the EMA layer give contributions only at energies above 4.8 eV, which is the surface sensitive energy range. X-axis denotes the energy of the incident light in eV, and y-axis is in arbitrary units. Note that this plot is identical to Figure 4.11, since the models are the same.

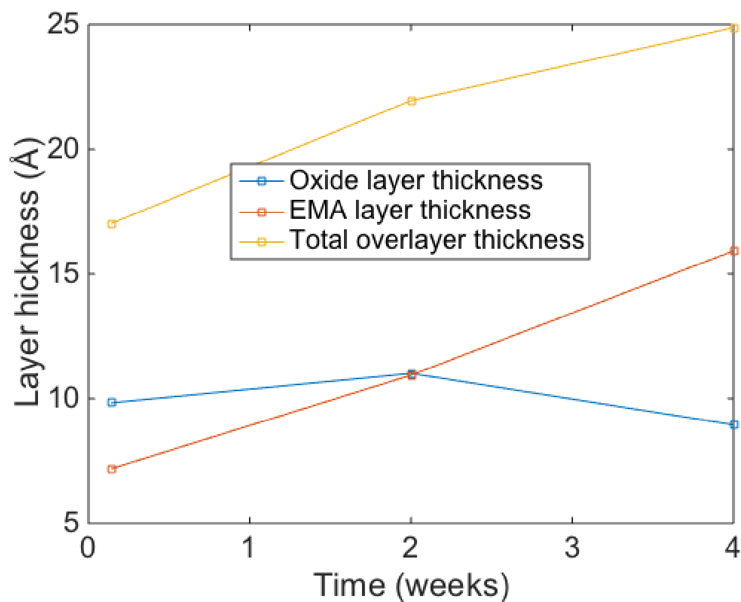

Figure 4.24: Evolution of the layer thicknesses of buffer sample B from 26 hours to 4 weeks after exposure to air, obtained by using Model 6 described in Section 3.5. Blue line is the oxide layer thickness, red line is the EMA layer thickness, and the yellow line is the sum of the thicknesses of the two overlayers. The x-axis denotes time in weeks, and the y-axis denotes layer thickness in Å.

4.5 Comparison of AFM instruments

It has proven quite difficult to estimate how much the drift we experienced with the Bruker Multimode AFM instrument affects the numerical values for surface roughness. In an attempt to gain some idea of the effect of the drift, we did some AFM measurements using the Cypher instrument from Asylum Research. This instrument is newer than the Multimode, does not have problems with any significant drift, and should in theory be a better instrument. Figure 4.25 shows two sets of images. Figure 4.25a is substrate sample C, imaged with the Bruker Multimode instrument that has been used throughout this thesis. Figure 4.25b is also substrate sample C, imaged using the Cypher instrument. Figure 4.25c and Figure 4.25d are buffer sample A imaged by the Multimode and Cypher respectively. The corresponding images are not from the same areas on the samples, and the experiment was only meant to give an indication of how certain the numerical values obtained from the Multimode instrument were. The images from the Multimode and the Cypher were taken one day apart. At this point, the substrate samples had been exposed to air for 15 weeks, and the buffer samples had been exposed to air for 7 weeks.

To get an idea of the shape and size of the two probes used for the two instruments, the ”Blind tip estimation” function in Gwyddion was applied to the images in Figure 4.25. The results are shown in Figure 4.26.

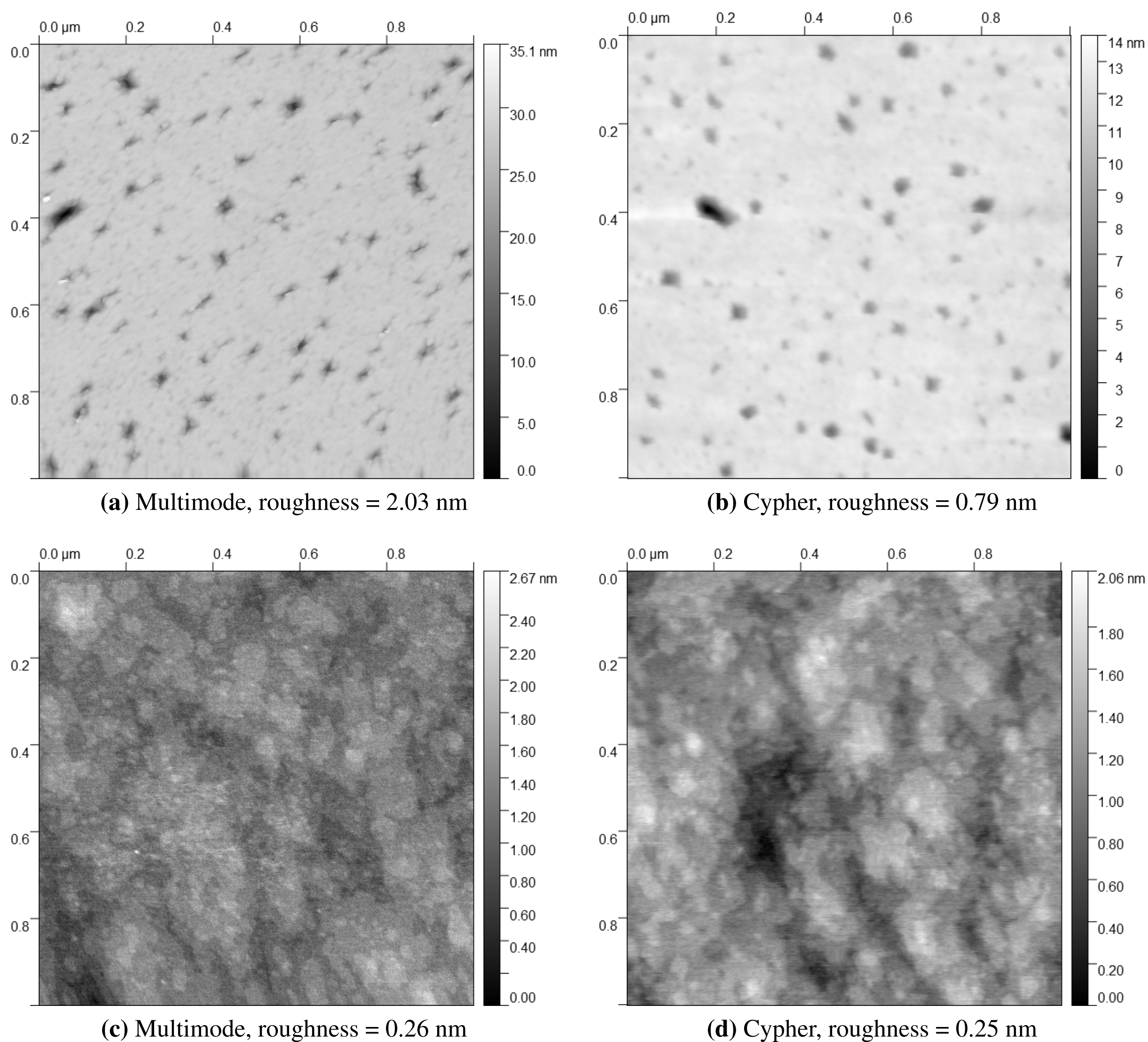

(a) Multimode, roughness = 2.03 nm

(b) Cypher, roughness = 0.79 nm

(c) Multimode, roughness = 0.26 nm

(d) Cypher, roughness = 0.25 nm

Figure 4.25: 1 µm x 1 µm AFM images captured using two different AFM instruments. (a) Substrate sample C imaged with the Multimode, (b) substrate sample C imaged with the Cypher, (c) buffer sample A imaged with the Multimode, (d) buffer sample A imaged with the Cypher. RMS roughness is given for each image. Substrate samples have been exposed to air for 15 weeks, buffer samples have been exposed to air for 7 weeks.

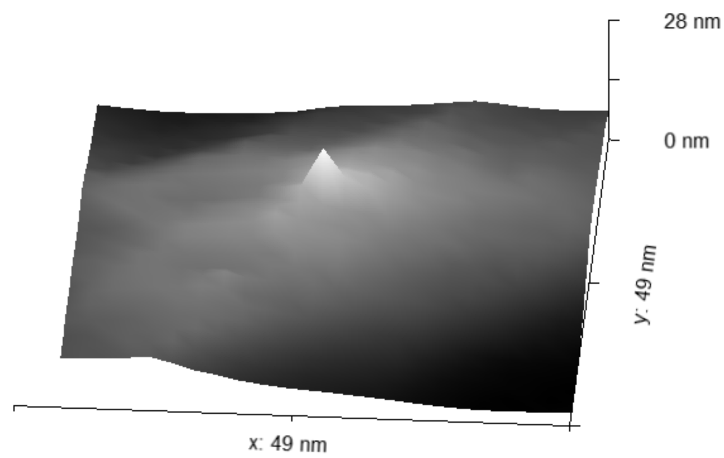

(a) Tip estimation, Multimode scan

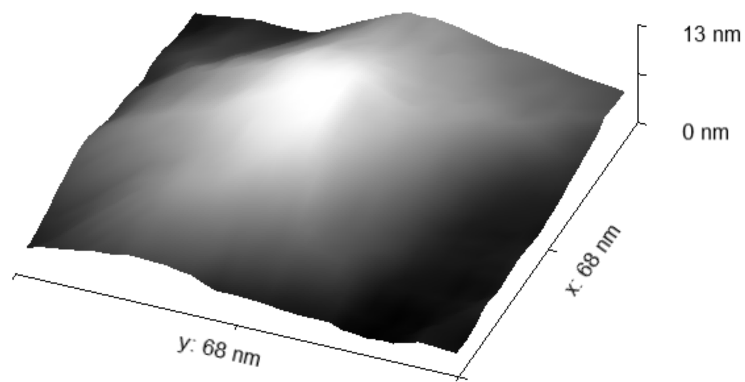

(b) Tip estimation, Cypher scan

(c) Close-up of tip, Multimode scan

Figure 4.26: Blind tip estimation function in Gwyddion applied to the images in Figure 4.25. (a) Tip estimation obtained from the Multimode scan in Figure 4.25a, (b) Tip estimation obtained from the Cypher scan in Figure 4.25b. (c) Close-up of the tip in (a). Note the difference between (a) and (b) in length, width, and height of the image.

Chapter 5

Discussion

In this chapter, the results presented in Chapter 4 will be discussed. The drift and distortion, as well as the tip-related artefacts of the AFM images will be discussed first, as they may have affected the numerical values obtained from the AFM images. Next, the results from AFM and VASE for the substrate sample will be discussed. Thereafter, the results from AFM, optical profilometry, and VASE for the buffer sample will be discussed. A discussion on the comparison of the two AFM instruments will close this chapter.

5.1 AFM drift and distortion

According to Bruker, the drift seen in Figure 4.1 is common in open loop systems, as all piezo scanners have some intrinsic piezo drift [14]. If there is also some thermal drift in the system from temperature changes due to i.e. changes in air flow on the probe/surface area, or the light from the laser or the optical microscope, the drift can get quite complicated. Although Bruker states that some drift is to be expected, the drift in Figure 4.1 is quite substantial, and makes me question the validity of the numerical values obtained from these measurements. As we can see from Table 4.1, the values for surface roughness vary noticeably from image to image in Figure 4.1. This could be due to the fact that the same area is not scanned every time, as is obviously the case in Figure 4.1. For example, the grey scales indicate that Figure 4.1a has deeper pits and higher peaks than Figure 4.1f has, which would explain why the former has a larger surface roughness than the latter. This variation in surface roughness also implies that the measurements are sensitive to local variations on the surface, at least on the substrate sample. If thermal drift is part of the problem, one could try to leave the system scanning for several hours, in hopes that the system will stabilize. Another reason for this variation in surface roughness might be the stretching of the images that was mentioned in Section 4.1. This stretch is difficult to quantify, and it is not certain whether the stretch would smooth the scan, and cause the roughness to decrease, or if it would roughen the scan, and cause the roughness to increase. This stretching resembles hysteresis, which is also intrinsic to any piezo scanner, but should theoretically be corrected for by the AFM instrument. In any case, we should expect some variation in the surface roughness measurements obtained from the Multimode AFM, at least if the sample surface is subject to significant local variations. If we observe large variations in the surface roughness, we should view the numerical values as rough estimates, rather than exact measurements.

5.2 AFM tip-related artefacts and challenges

As previously mentioned, and shown in Figure 2.3, the resolution of the sample surface topography is directly tied to the geometry of the AFM probe tip. Some of the line profiles in Figure 4.2 and Figure 4.3 show that the pits on the substrate sample have a triangular shape, with a very narrow bottom. This is an indication that the shape of the pit is affected by the shape of the probe, as the probe is supposedly triangular in shape, with a very sharp tip. The probe has probably not been able to reach all the way to the bottom of the pit, and interaction between the pit and the probe tip and sides result in a tip-shaped pit. From this, we can assume that the depths of the pits are underestimated, which in turn will cause the measured surface roughness to be lower than what it actually is. Combining this with the drift and distortion, we can assume that the AFM measured surface roughness is not only a rough estimate, it is also an underestimation.

5.3 Substrate sample

5.3.1 AFM

Previous studies that have been done on epi-ready GaAs wafers that have been thermally desorbed and then exposed to air, have found the same pitted surface as we did on the substrate sample. According to the findings of Ref. [33], thermal desorption of GaAs wafers at 620°C for 30 minutes results in a pitted surface, with vertical range (or peak-to-peak roughness) of about 4 nm. In addition to this, the study showed that the roughness increased as the desorption time increased, and as the desorption temperature increased, see Figure 5.1. The AFM images obtained in Ref. [33] for the GaAs substrates that had been thermally treated at various temperatures for various lengths of time is shown in Figure 5.2.

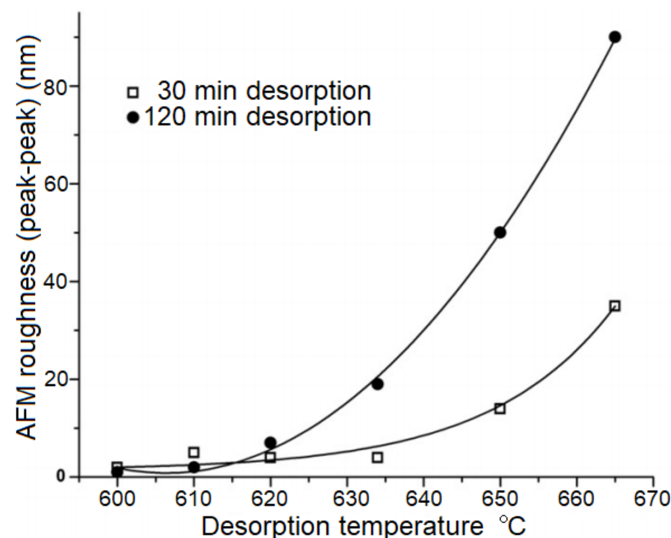

Figure 5.1: Dependence of surface morphology of (100) GaAs wafer on desorption temperature and time according to the findings of Ref. [33]. The surface morphology becomes rougher as the desorption temperature and/or desorption time is increased. Figure taken from Ref. [33].

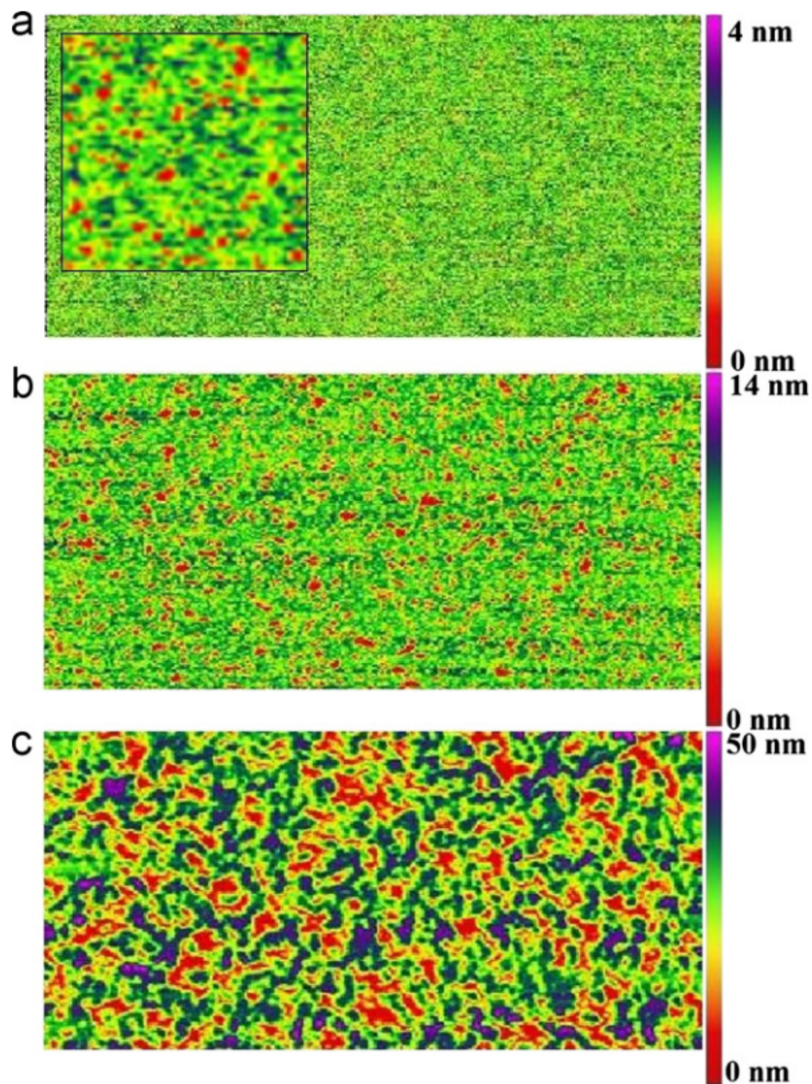

Figure 5.2: 5 µm x 10 µm AFM images of thermally desorbed GaAs wafers from the study in Ref. [33]. (a) 30 min thermal desorption at 620°C, 4 nm vertical scale (inset shows 0.5 µm x 0.5 µm scan), (b) 30 min thermal desorption at 650°C, 14 nm vertical scale, (c) 120 min thermal desorption at 650°C, 50 nm vertical scale. Images taken from Ref. [33].

The substrate samples in the re-oxidation experiments in this thesis were thermally treated at 630°C for 10 minutes. Considering Figure 5.1, this should have resulted in a vertical range, or peak-to-peak roughness, of less than 10 nm. However, as seen in Figure 4.4 and Figure 4.5, the vertical range for the AFM images of the substrate sample is never less than 23 nm, and often closer to 30 nm. Keep in mind, these ranges are obtained from 1 μm^2 AFM images. Figure 5.3 shows the same 50 μm x 50 μm AFM image as in Figure 4.6; substrate sample C from 9 weeks after exposing the sample to air. For this AFM image, the vertical range is 10.4 nm, significantly lowered compared to the 1 μm^2 images. A 5 μm x 10 μm area is marked in the AFM image in Figure 5.3. The vertical range for this area is 4.6 nm, which is much closer to the findings of Ref. [33]. This seems to indicate that a larger scan area produces a smaller vertical range, so perhaps the reason we obtain a much larger vertical range for our images than Ref. [33], is that our scan size is much smaller than theirs. The reason the 50 μm x 50 μm AFM image has a lower vertical range and surface roughness could also be because of the flattening procedure in Gwyddion that has been applied to the image. Larger images are subject to large image bow, which needs to be corrected for in the image processing.

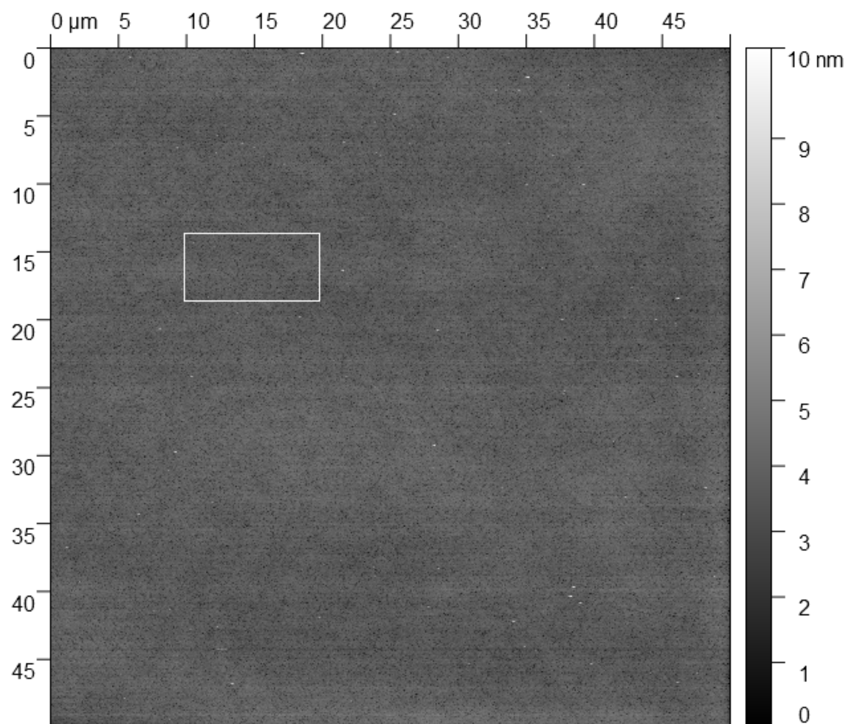

Figure 5.3: 50 μm x 50 μm AFM image of substrate sample C from 9 weeks after exposure to air. The vertical range for this image is 10.4 nm, which is significantly lower than the 25-30 nm vertical ranges for the 1 μm^2 AFM images of the substrate sample. This indicates that increasing the scan area lowers the vertical range, and the surface roughness. A 5 μm x 10 μm area is marked in the AFM image. This area has a vertical range of 4.6 nm.

It might have been easier to compare the results from Ref. [33] to our own result if they had also provided the RMS roughness for their samples, which is the roughness parameter that has been used in this thesis. The study in Ref. [33] however, only specifies the vertical range, or peak-to-peak roughness, of the AFM images. The qualitative results from our re-oxidation experiments do, however, match the results in Ref. [33]; the pits that we observed on the sub-

strate sample are to be expected, as they occur when thermally desorbing an epi-ready GaAs wafer. The 0.5 µm x 0.5 µm inset in Figure 5.2 looks similar to the 1 $µm^2$ AFM images of the substrate sample. There was an average of 45 pits per $µm^2$ in the images in Figure 4.5. The images in Figure 4.5 are from different samples, and the ones that are from the same sample are likely from different locations on the sample surface. We can therefore assume that the average of 45 pits per $µm^2$ is a representative number for the entire sample surface. This indicates an average of $4.5 \cdot 10^8$ pits/cm^2 on the substrate sample surface. This is also supported by the 50 µm x 50 µm image in Figure 4.6, which shows tiny black dots all over the sample surface.

It is interesting to examine the cause of these deep pits. The study in Ref. [33] also looked into the roughening mechanisms during thermal desorption, and they suspected that carbon that had been incorporated into the native oxide before the desorption might be responsible for the severe roughening of the surface. A series of sub-experiments, including secondary ion mass spectroscopy of various samples, confirmed that residual carbon atoms on a GaAs surface can induce severe roughening of the surface during thermal desorption. Moreover, carbon and oxygen appeared to have a synergistic effect towards surface roughening. Carbon without the company of oxygen caused a significant roughening of the sample, but with residual oxygen on the sample, only 10% of that carbon amount was needed to induce the same roughening on the sample.

There was a noticeable increase in the surface roughness for the first hour of exposing the substrate sample to air, see Table 4.2. We have previously discussed drift as possibly being the cause for such a variation in the roughness. Let us now compare the drift and change in surface roughness for the substrate sample after one hour of exposure to air (Figure 4.4 and Table 4.2) to the drift and change in surface roughness after five weeks (Figure 4.1 and Table 4.1). The drift in Figure 4.4 is not as pronounced as in Figure 4.1, but the change in surface roughness for the images in Figure 4.4 is larger than in Figure 4.1. In other words, the drift alone might not be responsible for the change in surface roughness during the first hour of exposure to air. This could be an indication that there is a formation of a native oxide that roughens the sample surface. According to Ref. [33], it takes about 20 minutes of exposure to air before a $\sim$ 3 nm oxide layer has formed on the surface. It is also assumed that "this oxide is sufficiently thin and uniform so as not to affect our roughness results" [33]. If this assumption is true, that would imply that the reason for the increase in surface roughness that we observe in Figure 4.4 is not due to the formation of the native oxide layer, but to something else. If it is not due to the oxide layer, and not entirely due to the drift, I do not know what is causing this variation in the surface roughness.
As opposed to the assumption made in Ref. [33], that a $\sim$ 3 nm thick native oxide layer forms within 20 minutes of exposure to air, a study carried out by Ref. [23] found that a GaAs substrate that had its native oxide removed by chemical etching would need about a year of exposure to ambient air in order to form a $\sim$ 2 nm thick native oxide layer. This estimation was done by use of XPS. Another study, Ref. [34], used grazing incidence X-ray reflectivity and surface photoabsorption to determine the oxide layer thickness over time, and found that it grew from $\sim$ 2 nm on day 0 to $\sim$ 3 nm on day 426. From all these studies we can assume that a stable native oxide layer is between 2-3 nm thick, but it is not obvious how quickly the oxide forms on the surface. This is what we attempted to determine with the use of VASE.

The variation in surface roughness for the follow up scans done in the weeks after exposing

the substrate samples to air (Figure 4.5 and Table 4.3) are more difficult to interpret. The measurements vary significantly for the different samples, and measurements done on the same samples are inconsistent: decrease on substrate sample A from week 3 to 5, increase on substrate sample C from week 9 to week 15, large roughness for substrate sample B.

If we accept the assumptions made in Ref. [33], that a stable native oxide layer with thickness ~ 3 nm forms in under 30 minutes, then the variation in surface roughness for the follow-up scans are likely only due to drift, local variations within samples, and possibly some difference between the three samples being imaged. Although they all come from the same wafer, they have been stored in separate laboratories. It has been shown that humidity in the air affects the growth of oxide on GaAs; more humidity yields a thicker oxide layer [35]. The AFM samples, substrate samples A and C, have been kept in the same laboratory throughout the process, and the laboratory where the AFM instrument is kept is a so-called *cleanroom*, where the air humidity is controlled. Substrate sample B, the VASE sample, has been kept in a different laboratory from the AFM buffer samples A and C, a laboratory that does not have air humidity control. This could have affected the growth of the oxide layer on the VASE sample, and if the thickness of the oxide layer does actually affect the surface roughness, that could explain why the surface roughness of substrate sample B differs so significantly from substrate sample A and C in Table 4.3. We will come back to this hypothesis on humidity in a later section. Whether or not humidity could be a factor in the variation in surface roughness, I will once again point out that these values must be viewed as rough estimates for the surface roughness, as there are just too many factors that have an undetermined effect on the measurements.

5.3.2 VASE

As seen in Figure 4.7, the model consisting of an EMA layer of 50% GaAs and 50% void on a GaAs substrate fits very well with the measurements made during the first 240 minutes for substrate sample B. This is also confirmed by the low MSE of 2.572. This model does not include any GaAs oxide, which might seem strange, as we have previously discussed that according to Ref. [33], a fairly thick oxide layer should form on a fresh GaAs surface within minutes of being exposed to air. A possible explanation can be found in a weakness of the VASE modelling. One of the main findings in my specialization project report, Ref. [7], was that it is very difficult to separate the effect of surface roughness from an oxide layer when doing ellipsometry. This is especially true when the roughness or oxide layer thickness is small, below 2 nm. This result was also found by my predecessor Maja Drøyli in her master's thesis [6]. In other words, the fact that the model we have used does not include an oxide component does not mean that there is none. It might simply be that the software interprets the growing oxide layer as roughness, and therefore the model with an EMA of GaAs and void is the best fit.
Another possible explanation might be that the oxide layer does not actually form as quickly as assumed in Ref. [33]. It is possible that there is simply not enough of an oxide layer forming during those initial 240 minutes for the ellipsometer to detect it as oxide, it just detects it as *something*. Regardless of the explanation, if we compare $\langle \varepsilon_2 \rangle$ from the measurements to $\langle \varepsilon_2 \rangle$ of plain GaAs in Figure 4.7, we see that there is clearly something more than just plain GaAs on our sample. Even though our model does not actually include anything other than GaAs and void, adding the EMA layer to the substrate clearly affects the pseudo dielectric function of the model as a whole, and provides a good fit with the measured sample. The model deviates slightly from the measurements in Figure 4.7 for energies above 4.6 eV, which is the surface

sensitive energy range. This supports the assumption that we are not properly modelling the surface of the sample.

We see from Figure 4.9 that the EMA layer thickness increases from around 1.75 nm in the very first minutes after exposure to air, to around 2 nm after about one hour. We have previously stated that the EMA layer is a good approximation for surface roughness on a sample, and this is backed up by the findings of Ref. [36]. Figure 5.4 shows the linear correlation between AFM measured roughness and VASE deduced EMA layer thickness found in the study in Ref. [36]. Figure 5.5 shows the VASE deduced EMA layer thickness and AFM measured roughness for the substrate sample plotted in the same figure. As we can see from Figure 5.5, the EMA layer thickness and AFM measured surface roughness seem to correlate fairly well. The exception is the dip in AFM roughness at 14 minutes, which seems to be a random stray value compared to the rest of the AFM measurements, which are steadily increasing. If we exclude this value from the data set, and plot the EMA layer thickness versus the AFM measured roughness, we obtain the plot shown in Figure 5.6. This plot indicates that we have a similar linear correlation between the EMA layer thickness and AFM roughness in this thesis as obtained in the study in Ref. [36].

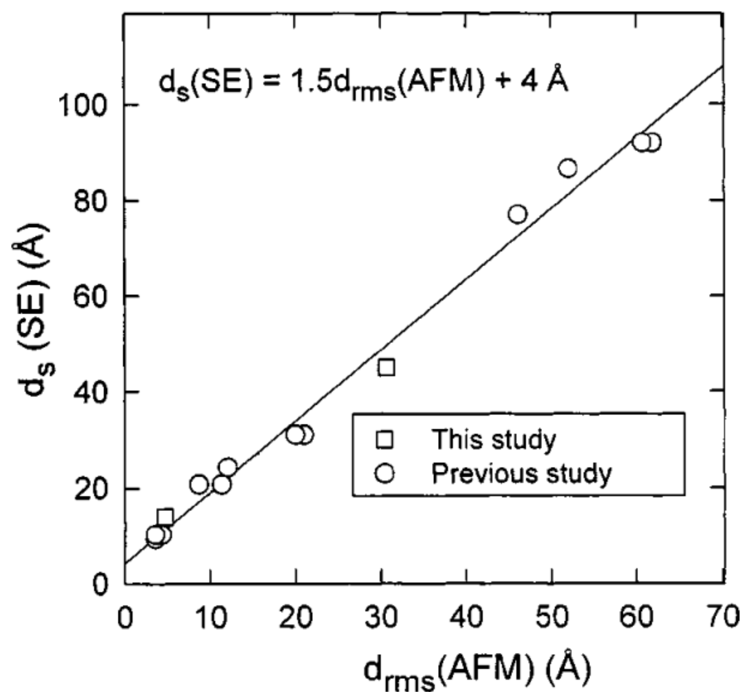

Figure 5.4: Plot of the linear relationship between AFM measured roughness and the VASE deduced EMA layer for amorphous silicon samples from the findings of Ref. [36]. The square data points were obtained in the study in Ref. [36], whereas the open circles were obtained in a previous study of different amorphous semiconductor films. Figure shows that VASE deduced EMA layer has a good correlation with AFM measured surface roughness, indicating that EMA is a suitable way of modelling surface roughness. Figure taken from [36].

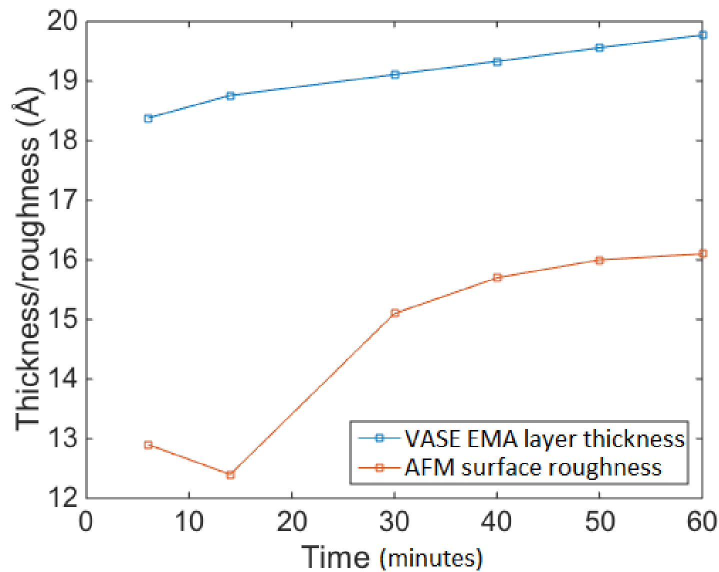

Figure 5.5: AFM measured surface roughness and VASE deduced EMA layer thickness for the substrate sample for the first hour after exposure to air. X-axis denotes time after exposure to air in minutes, y-axis denotes layer thickness/surface roughness in Å. The dip in surface roughness could be either a false value, or an indication that the AFM roughness values are varying due to drift. The EMA layer thickness is around 0.5 nm larger than the AFM measured roughness, which could indicate that the EMA layer is not equivalent to just the surface roughness, but also accounts for the oxide.

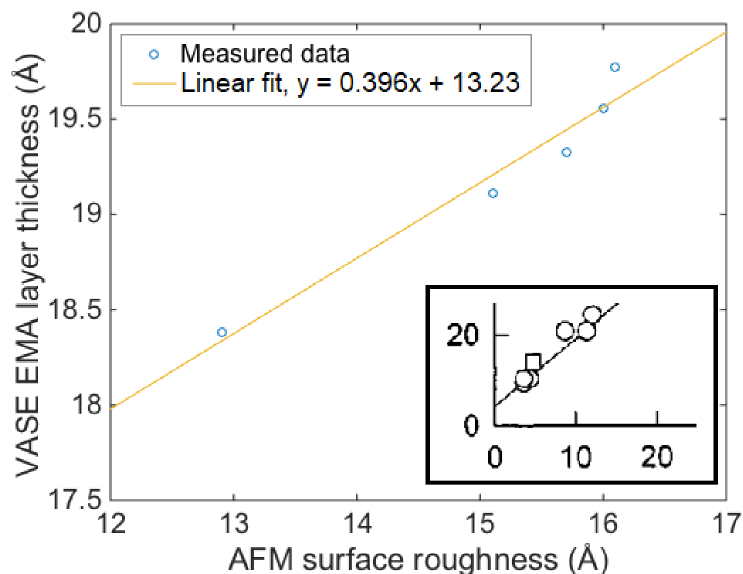

Figure 5.6: Plot of the linear relationship between AFM measured roughness and the VASE deduced EMA layer for the substrate sample in the first hour of exposure to air. The circles show the same data points as in Figure 5.5, excluding the data point at 14 minutes, and the yellow line is the linear fit of the data. The plot shows that the VASE deduced EMA layer has a good correlation with the AFM measured surface roughness for the substrate sample in the first hour after exposure to air, indicating that EMA is a suitable way of modelling surface roughness. In the bottom right corner of the figure parts of Figure 5.4 is shown for comparison.

Although the linear correlation in Figure 5.6 is good, the non-zero y-intercept indicates that the VASE deduced EMA layer is accounting for something more than just the surface roughness, namely the oxide that is forming on the sample surface. This assumption is supported by the main findings in my specialization project report, Ref. [7], that the ellipsometer has difficulty separating surface roughness from oxide when one or both of the layers are thin.

If we assume that the difference between the AFM measured roughness and the EMA layer thickness is caused by the oxide layer, we could make a simple estimation of the oxide layer thickness from either Figure 5.5 or Figure 5.6. The EMA layer is approximately 0.5 nm larger than the AFM measured surface roughness for the first hour after exposure to air, implying that a 0.5 nm oxide layer forms right after the sample is exposed to air, and then remains more or less constant for at least the next hour. This contradicts the assumptions made in the study in Ref. [33], that a 3 nm oxide layer forms on the substrate surface within 20 minutes of exposure to air. It does, however, resemble the findings of Ref. [23], where they found the oxide layer to be 0.44 nm right after removal of the native oxide by chemical etching. In that study, the oxide grew to 1.55 nm after half a year, and then to 1.82 nm after a year, where it stabilized. Assuming that the oxide layer grew at a constant rate over that year, the growth per hour would have been practically impossible to detect. The study in Ref. [23] did not do continuous measurements after exposing their sample to air, they did one measurement right after exposure, and then again at 6 months, one year, and two years. Therefore, we cannot tell from that study whether or not the oxide layer went from 0.44 nm to 1.55 nm slowly and continuously over the first 6 months, or if most of it formed in a short time, and then the oxide layer growth slowed down. If we assume that the oxide on the substrate sample forms slowly and steadily over time, it does not explain why the surface roughness of the substrate sample increases as much as it does for the first hour, if the oxide layer barely grows. Another possible explanation could be that the oxide layer thickness cannot be estimated by simply considering the difference between the EMA layer thickness and AFM measured roughness when the layers are thin and their effects are difficult for the ellipsometer to separate. A final possible explanation could be that the AFM measured surface roughness values are varying due to the image drift, and just happened to increase for this specific time period, leading me to assume that the formation of the oxide was affecting the surface roughness. The one odd value for the AFM roughness at 14 minutes in Table 4.2 and Figure 5.5, which I previously assumed to be a false value, might actually be an indication that the seemingly increasing roughness value is just a coincidence. In any case, I am not able to estimate the oxide layer thickness based on this data alone, as I do not know if I can trust the AFM data, and the ellipsometer does not do well with separating oxide from roughness.

The model that was best suited for 1-12 weeks after exposure includes all the ”expected” layers: GaAs substrate, GaAs oxide layer, and an EMA layer of GaAs oxide and void, to simulate the surface roughness. From this, we know that a significantly thick oxide layer must have formed on the surface since the first few hours of exposure to air, since the best fitting model now includes an oxide layer. The fit is, however, not as good for this model as it was for the one used to model the first 240 minutes of exposure to air. This is illustrated by the differences between model and measurement that we saw in Figure 4.10, and the relatively high MSE of 4.253. From Figure 4.12, we see that the oxide layer and EMA layer display some inversely proportional behaviour. Since the beam from the light source of the ellipsometer is comparable in size to the substrate sample, and the sample has a specific way of being mounted, we can safely assume that the ellipsometry measurements are not affected by local variations on the sample surface. This behaviour of the EMA and oxide layer is therefore not physical, but

rather a result of the ellipsometry software CompleteEASE trying to make the best fit for the measurements. It is perhaps more illustrative to look at the total overlayer thickness in Figure 4.12, which increases by about 0.5 nm (from 2.7 nm to 3.2 nm) from week 1 to week 12 after exposing substrate sample B to air. It is a slow change, but this is an indication that something is happening on the sample surface during these 12 weeks. No matter if we assume that the oxide layer growth affects the surface roughness, or that the oxide layer grows uniformly and does not affect the surface roughness, there is some formation of oxide over the 12 weeks following the exposure of substrate sample B to air. This again contradicts the assumption made in Ref. [33], that a stable $\sim$ 3 nm oxide forms on the surface within 20 minutes of exposing the sample to air. It seems to rather support the theory of a slowly growing oxide. Since we do not know if or how the oxide growth affects the roughness, and the variation in the measured AFM surface roughness is so large and unsystematic, I will not attempt to give a precise estimate of the oxide layer thickness. I will rather point out that if we consider the total overlayer thickness plotted in Figure 4.12, and we assume that that the surface roughness does not exceed 2 nm, we can roughly estimate the oxide layer thickness to be at least 1 nm thick after 12 weeks of exposure to air. This again assumes that the oxide layer can be estimated by considering the difference between the overlayer thickness and the AFM measured surface roughness, and attributing this difference to the oxide layer.

5.4 Buffer sample

5.4.1 AFM

It is clear from the AFM images of the buffer sample that the buffer layer has significantly flattened the substrate, as is to be expected. For the consecutive images shown in Figure 4.13 we see that there is a noticeable drift, but the corresponding values in Table 4.4 show that the surface roughness remains close to 0.35 nm for these images. The surface roughness decreases a little after this, but remains more or less within a range of 0.30 ± 0.05 nm throughout the weeks following exposure to air, as we can see from Table 4.5. Even the images that were visibly blurred due to problems with the AFM tip, see Figure 4.14b and -d, had a surface roughness that was still within a close range of 0.30 nm. This might be an indication that the buffer sample is not as sensitive to tip geometry, drift, and local variations on the sample surface as the substrate sample seemed to be. Table 4.5 showed that there was an increase of 0.05 nm in surface roughness from week three to week five, and a similar decrease of 0.05 nm from week seven to week eight. A variation of 0.05 nm for this sample is not insignificant, but it is small enough that we can put some trust into these results, at least more than we put into the AFM results for the substrate sample.

Although the buffer sample was expected to be atomically flat, there is a terrace-like structure visible in the AFM images for buffer sample A. This is also shown by the line profiles in Figure 4.15 and Figure 4.16. If we look at the step heights between neighbouring terraces in both Figure 4.15 and Figure 4.16, we see several steps in the range of 0.26-0.30 nm. This is roughly equivalent to half the lattice constant for GaAs, which is 0.56 nm, and would indicate that the terrace structure stems from plateaus of half-grown GaAs unit cells on the substrate surface. Whether this terrace structure occurred during the thermal desorption, and the buffer layer was then grown so uniformly that the structure remained intact through the 300 nm buffer layer, or whether the structure is a result of the buffer layer growth, is not certain. However, if the buffer layer was grown so uniformly that it preserved the underlying structure, we would perhaps have seen something resembling the pits that we see on the substrate sample. As there are no traces of such pits on the buffer sample, it seems likely that this layered structure was not there after the thermal desorption of the oxide, but is a result of the growth of the GaAs buffer layer. From the line profiles in Figure 4.15 and Figure 4.16, we also see that each terrace does not actually have a clearly defined height, there is some variation or noise in the line profile. The height of the terraces are calculated based on an average value for the terrace, which might be the explanation for why the step heights are not exactly half the lattice constant of GaAs, 0.28 nm. Figure 5.7 shows the AFM image and line profile from Figure 4.16, along with an illustration of the GaAs unit cell. In Figure 5.7c, an average step height from multiple steps has been calculated to be 0.28 nm. This is exactly half the lattice constant, or one monolayer, of GaAs. This terrace-like surface is present throughout the weeks following exposure to air, indicating that the oxide layer grows uniformly, and preserves the underlying structure.

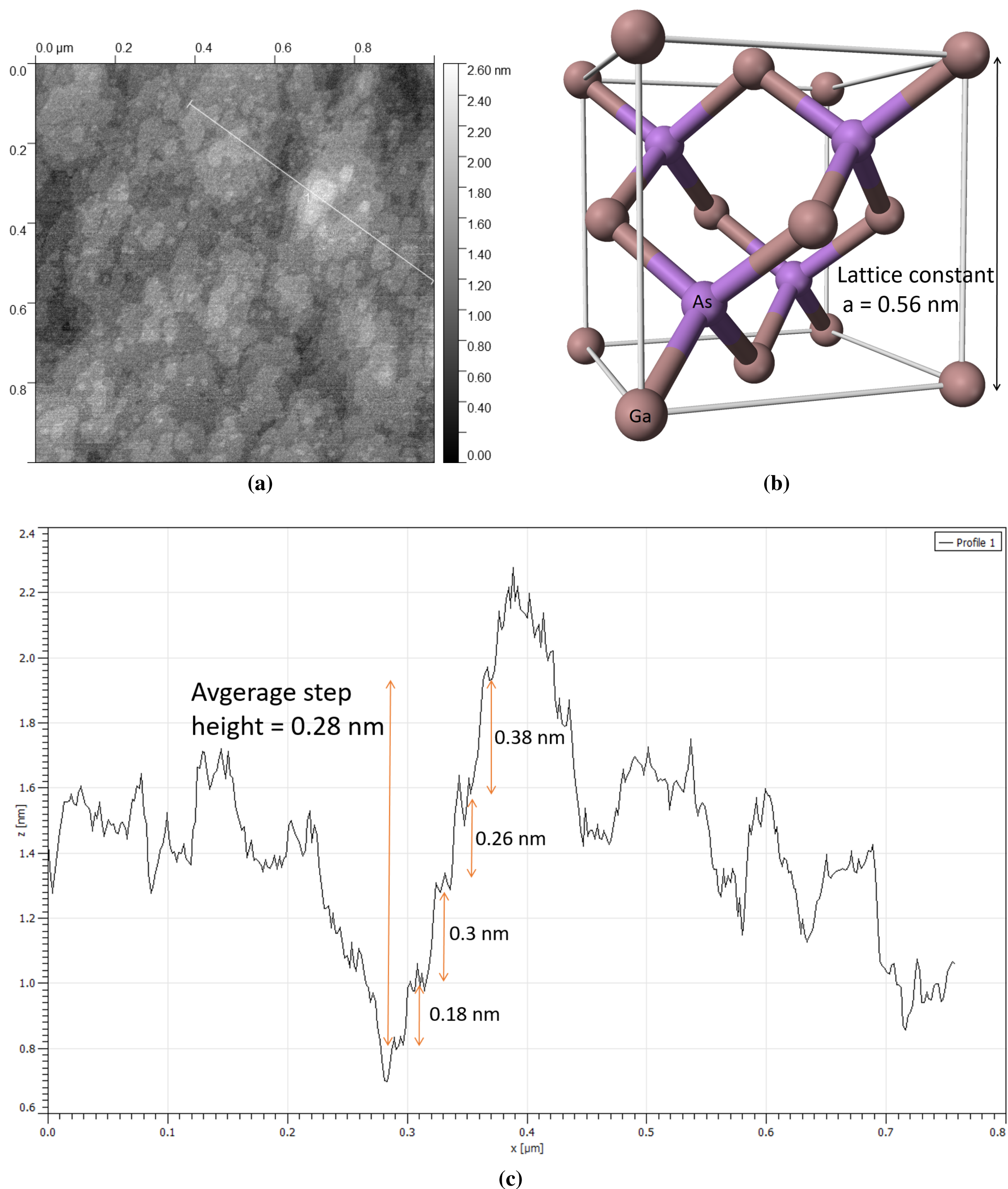

Figure 5.7: (a) 1 µm x 1 µm AFM image of buffer sample A from one week after exposure to air, with a line profile marked in the image. (b) Schematic of the GaAs crystal structure with the lattice constant indicated. (c) Line profile from (a) with the step values between some of the neighbouring terraces noted in the image, as well as an average step height calculated from several steps. The average step height is 0.28 nm, half of the lattice constant of GaAs, or one monolayer. This indicates an underlying terrace structure that stems from growth of GaAs monolayers.

5.4.2 Optical profiler

The intent of using the optical profiler was to see if we could obtain similar values for surface roughness as we did with the AFM. The 3D images of the buffer sample shown in Figure 4.17 and Figure 4.18 have slightly higher calculated RMS surface roughness than what was measured with the AFM. The AFM images are typically 1 μm x 1 μm in size, whereas the optical profiler images are 36 μm x 48 μm in size with the magnification used in these scans, which could be a factor in why the profiler differs from the AFM in surface roughness. Another factor could stem from an artefact of the scan method. In order to get a good measurement, the sample stage must be tilted to bring out a certain number of interference fringes on the sample. Figure 5.8a shows a screenshot from the user interface of the optical profilometer software, Vision64. This is a live-view from the microscope that is focused on the sample. As we can see, there are distinct fringes over the diagonal of the image, meaning that the microscope is correctly focused and ready to start the imaging. Sometimes, when doing optical profilometry, these fringes show up on the resulting image, as seen in Figure 5.8b. This causes the topographic image to become distorted and affects the height scale, which in turn will affect the surface roughness calculation. In Figure 4.17, there seems to be two or three ridges running across the diagonal of the surface, which might actually stem from the interference fringes. This could have resulted in a larger surface roughness than what is actually the case. Figure 4.18 also has some elevated areas, but it is not certain whether these stem from the fringes or not.

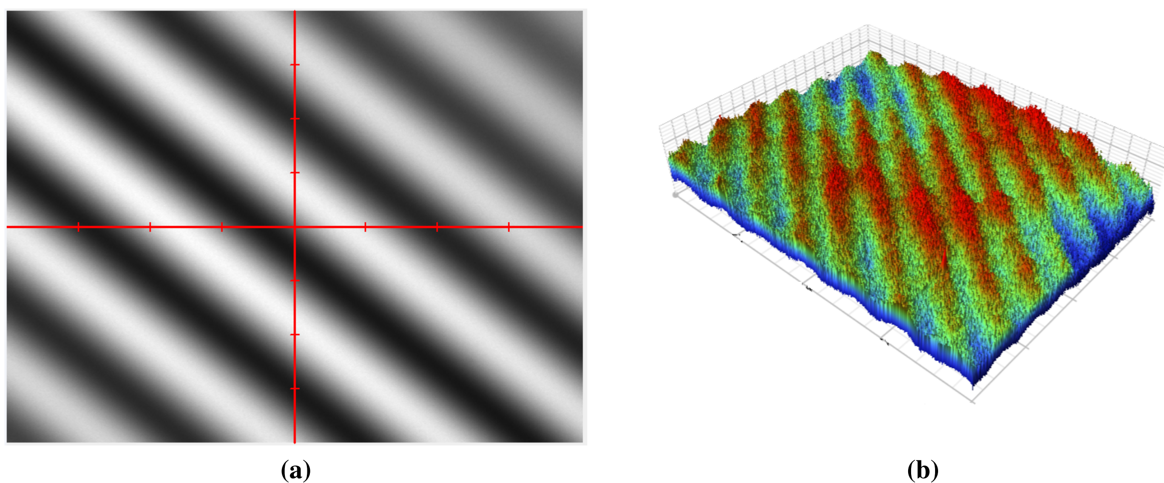

(a) **(b)**

Figure 5.8: (a) Screenshot from the user interface of the optical profilometer software, Vision64. To get a good measurement, one should tilt the sample stage until there are a suitable number of fringes covering the view of the sample. These fringes sometimes show up very clearly as an artefact in the resulting image, as shown in (b).

Although the profiler measured roughness is somewhat larger than the AFM roughness, they are still fairly similar, which is good for reliability of the AFM results. It also indicates that the profiler could be a suitable companion, if not alternative, to the AFM. The profiler does not have issues with drift, and it is much easier to operate than the AFM. A challenge with the optical profiler though, is that it struggles with abrupt changes in height on surfaces. The profiler does not, for example, handle the deep pits of the substrate sample too well. In addition to this, one needs to look out for the fringe artefact as seen in Figure 5.8.

I previously mentioned that I suspected differences in humidity in the air to be a cause of the large difference in AFM measured surface roughness between the VASE substrate sample and the AFM substrate samples, see Table 4.3. As the optical profiler does not do well with imaging the deep pits on the substrate samples, I tried to test my hypothesis on the buffer samples instead. Both the VASE and AFM buffer samples had been exposed to air for the same length of time, and the AFM buffer sample had not left the cleanroom, where the air humidity is controlled. If I had measured a higher surface roughness on buffer sample B than on buffer sample A, that would support what I discussed on this hypothesis in Section 5.3.1. However, the roughness for buffer sample B turned out to be 0.03 nm lower than for buffer sample A. Although this is a very small difference, it does go against my original hypothesis. This could of course be caused by the fringe artefact that might have affected the scan of buffer sample A, but I do not know how large the effect of this artefact is. In any case, as I do not know the humidity of the air in the VASE lab in relation to the cleanroom, I do not actually know whether I should expect the VASE sample to be rougher or smoother than the AFM sample. This hypothesis also depends on the assumption that the oxide layer does have an effect on the surface roughness, which is the exact opposite to the assumption made in Ref. [33], that the oxide layer grows uniformly and preserves the roughness and underlying structure of the sample. This also goes against what we observed with the preserved terrace structure for the buffer sample.

5.4.3 VASE

Figure 4.19 indicates that the model consisting of a GaAs substrate with a GaAs oxide layer fits very well with the measurements done on the buffer sample for the first 180 minutes after exposure to air. This is also supported by the low MSE of 2.016. In the case of the buffer sample, as opposed to the substrate sample, this model does include a GaAs oxide layer, but no EMA layer to simulate the roughness. Again, this might be a consequence of the ellipsometer having difficulty separating the effects of oxide and surface roughness. We know from the AFM measurements that the surface roughness of this sample is very low, around 0.35 nm at this point in time, meaning that the oxide layer in the model might be accounting for both the oxide and the surface roughness. The fact that the model with the GaAs oxide layer provides a better fit than a model with an EMA layer might be an indication that the GaAs oxide is the dominating surface feature on this sample at this point in time, and not the surface roughness.

Figure 4.21 indicates that the oxide layer thickness on the buffer sample increases from around 0.95 nm to 1.15 nm during the first hour of exposure to air. The AFM measurements for buffer sample A (Table 4.4) indicate that the roughness is stable around 0.35 nm for the first few hours after exposing the sample to air. As mentioned previously, buffer sample A was in a sample box for two days before I could do AFM measurements on it, and as we cannot be certain that the sample box was completely air tight, some oxidation of the buffer sample may have occurred during those two days. However, as the roughness measurements were relatively stable around 0.30 nm throughout the weeks after exposing the sample to air, I choose to trust that these values hold for the first hour of exposure as well. If we assume that the GaAs oxide in the VASE model is actually a sum of oxide thickness and surface roughness, and we assume that the AFM measured surface roughness of 0.35 nm is correct, we can estimate the oxide layer thickness to be around 0.80 nm after one hour of exposure to air.

For the time interval between 26 hours and 4 weeks after buffer sample B was exposed to air,

the best suited model changes from Model 7 to Model 6, meaning that we add an EMA overlayer of 50% GaAs oxide and 50% void to the GaAs oxide and GaAs substrate. The fit of the model is good, with an MSE of 2.281. However, as the AFM measured surface roughness stays almost constant throughout the weeks following exposure of the buffer sample to air, it is unclear why adding an EMA layer to the model produces a better fit. Figure 4.24 indicates that the oxide layer decreases from week 2 to week 4, which is a non-physical behaviour, and obviously a result of CompleteEASE trying to make the best fit possible. In addition, the EMA layer that we usually consider as the surface roughness is in the range 1.0-1.5 nm thick, which does not match at all with the AFM measured roughness. It is important to remember that the EMA layer is not 100% equivalent to surface roughness, and as we have seen previously both in Ref. [36] and for the substrate sample, the EMA layer seems to tend to overshoot compared to the AFM measured surface roughness (see Figure 5.6). Since the AFM results indicated that the surface roughness is low for this sample, the ellipsometer could be having difficulty with separating the oxide and the roughness. We therefore choose to consider the total overlayer thickness instead of the oxide and EMA layers separately. Supplementing the plot in Figure 4.24 with the AFM measured roughness, we roughly estimate the surface roughness to be around 1.9 nm after 2 weeks, and around 2.2 nm after 4 weeks. The analysis of the AFM and VASE results for the substrate sample indicated that the oxide grew slowly and steadily. The analysis of the AFM and VASE results for the buffer sample, on the other hand, seems to point to a much faster oxide layer growth.

5.5 Comparison of AFM instruments

As seen in Figure 4.25, the Cypher images seem blurry compared to their Multimode image counterparts. For buffer sample A, the difference in surface roughness between the two images in Figure 4.25 is very small, practically non-existent. For substrate sample C on the other hand, there is a very large difference in the RMS roughness obtained from the two AFM instruments. Looking at the height scales of the two images in Figure 4.25a and Figure 4.25b, we see that the pits on the Multimode image are measured as being significantly deeper than the pits on the Cypher image. This is obviously why the roughness is so much lower for the Cypher image than for the Multimode image, but we are more interested in the cause of this difference in imaging. One could suspect differences in the size and geometry between the probes that were used for the two AFM instruments. As previously mentioned, the Multimode instrument has been operated using a triangular ScanAsyst probe from Bruker, with a nominal tip radius of 2 nm, and a maximum radius of 12 nm. The probe used in the Cypher instrument is a triangular PPP-NCH probe from Nanosensors, with a typical tip radius of about 7 nm. Considering the dimensions of the PPP-NCH probe compared to the ScanAsyst probe, and to the dimensions of the pits on the substrate sample (as shown in Section 4.2), the PPP-NCH probe should be just as able as the ScanAsyst probe to image the pits on the substrate sample surface. However, it is not impossible that the PPP-NCH probe has been damaged, worn, or contaminated, and therefore has not been able to detect the true depth of the pits. A possible way of checking this hypothesis is to consider the tip images obtained from the blind tip estimation.

As we see from Figure 4.26, the estimation of the ScanAsyst tip used in the Multimode AFM reveals a quite sharp, narrow, and long tip, whereas the estimation of the PPP-NCH tip used in the Cypher AFM is blunt, extends several nanometers in each direction, and is not as long. This could explain the difference between the Multimode and Cypher images shown in Figure 4.26a and Figure 4.26b. The PPP-NCH tip is just not sharp enough to reach into the pits of the substrate sample, and the resulting image is blurred, has a shortened height scale, and a lower surface roughness. The blunt PPP-NCH tip could also have caused buffer sample A to appear even smoother, and lowered the surface roughness. A PPP-NCH tip with the dimensions intended by the manufacturer would probably have produced a much sharper image, similar to the ones obtained by the Multimode AFM.

Chapter 6

Conclusions and Further Work

6.1 Conclusions

In this master's thesis, two GaAs substrates had their native oxides removed by thermal desorption in an MBE machine, and were then re-oxidised by exposure to air. One sample, the buffer sample, had a 300 nm GaAs buffer layer grown by MBE before being exposed to air. The other sample, the substrate sample, received no further treatment after having the oxide removed before being exposed to air. The samples were studied regularly with AFM and VASE, and the buffer sample was also measured using optical profilometry. The goal was to determine the surface roughness of the samples, as well as the manner of which the surface re-oxidises.

There was some unexpected drift and distortion of the AFM images, probably caused by a combination of the intrinsic piezo drift in the scanner, hysteresis, and thermal drift due to changes in air flow on the sample/probe area and the laser spot on the cantilever. This has likely had an effect on the values for surface roughness measured with AFM, and the effect seemed to be much larger on the substrate sample than on the buffer sample. Therefore, the AFM measured values for surface roughness for the substrate sample should be viewed as rough estimates. A look at the shape of the pits on the substrate sample indicated that the probe tip had not been able to reach the full depth of the pits, causing the pits to appear shallower than they actually were. This in turn would imply that the calculated surface roughness for the substrate sample was an underestimation of the true value.

The AFM measurements of the substrate sample revealed deep pits all over the surface, which was likely caused by residual carbon from the native oxide on the surface of the sample during the thermal desorption. It was estimated that there were approximately $4.5 \cdot 10^8$ pits/cm^2 on the sample surface. The surface roughness increased from around 1.3 nm after being exposed to air for a few minutes, to around 1.6 nm after an hour, and to around 2.0 nm after 15 weeks, but the values varied quite a bit during these 15 weeks. Due to the unexpected drift and distortion of the images, as well as the pits being too deep and narrow for the AFM probe tip to reach all the way into, the values for surface roughness are quite uncertain, and probably underestimated. Three different samples were measured in this part of the re-oxidation experiment. The values for surface roughness varied significantly from sample to sample, which could be due to local variations on the samples, or the samples could be subject to variations due to varying air humidity where they were being stored. An attempt at testing this hypothesis about air

humidity was made, but the results were inconclusive.
The model that best suited the VASE measurements of the substrate sample for the first four hours of exposure to air was a GaAs substrate with an EMA layer consisting of 50% GaAs and 50% void. This model included no GaAs oxide, but previous studies have shown that the effects of surface roughness and surface oxide are difficult to separate in VASE measurements, especially when the layers are thin. This means that the EMA layer can be interpreted as a combination of both oxide and surface roughness. Due to the uncertainty of the AFM measured surface roughness for this period of time, they were not used as input for the VASE measurements, and therefore no estimation of the oxide layer thickness for the first four hours were done.
The model best suited for the VASE measurements for the substrate sample done in the 12 weeks following exposure to air consisted of a GaAs substrate with both a GaAs oxide layer and an EMA layer consisting of 50% GaAs oxide and 50% void. Also here the AFM measured surface roughness was too uncertain to be used as input for the VASE measurements, and the results of the VASE modelling were affected by CompleteEASE trying to make the best fit, thereby displaying some non-physical behaviour. The VASE measurements did, however, indicate that something is happening on the substrate sample surface during the 12 weeks following exposure to air, which could indicate that the oxide forms slowly and continuously over time. No exact calculation of the oxide layer was made, but the oxide layer was roughly estimated to be at least 1 nm thick after 12 weeks of exposure to air.

The AFM images of the buffer sample showed a very smooth surface, with a terrace-like structure. The step heights between neighbouring terraces were on average 0.28 nm, exactly half of the lattice constant of GaAs. This is an indication that there existed a layered structure on the sample surface, probably as a result of GaAs forming in half-layers of the unit cell. This structure of GaAs monolayers was likely a result of the growth of the GaAs buffer layer. This terrace structure remained present throughout the weeks following exposure of the buffer sample to air, indicating that the oxide grows uniformly and preserves the underlying structure.
The surface roughness for this sample was measured to be around 0.35 nm a few days after exposure to air. The roughness then decreased slightly, to 0.3 ± 0.05 nm, in the following 8 weeks. Although there were some variations in the surface roughness, all measurements stayed within a 0.05 nm range of 0.30 nm in the weeks after exposure, indicating that the buffer sample was not as sensitive to changes in scan area as the substrate sample seemed to be. This also supports the assumption that the oxide layer grows uniformly on the surface, and that the oxide does not affect the surface roughness.
Measurements done with the optical profilometer on buffer samples A and B gave a surface roughness of 0.36 nm for buffer sample A, and 0.39 nm for buffer sample B, which is higher than the AFM measured values for surface roughness. Fringe artefacts may have affected the profilometer results and the scan area is significantly larger for the optical profiler than for the AFM, which could also be the cause of the difference in surface roughness.
The model best suited for the VASE measurements of the buffer sample for the first 180 minutes after exposure to air was a GaAs substrate with a GaAs oxide layer. This model did not include an EMA layer to simulate the surface roughness, but this could be caused by the surface roughness being so small that the ellipsometer had difficulty separating it from the oxide. Since the AFM results for the buffer sample were deemed far more trustworthy than those of the substrate sample, they were used as input for the VASE measurements. Combining the VASE model with the AFM roughness measurements gave an estimated oxide layer thickness of 0.80 nm after one

hour of exposure to air.
The model best suited for the buffer sample in the weeks following exposure to air was a GaAs substrate with a GaAs oxide layer, and an EMA layer of 50% GaAs oxide and 50% void. The EMA layer thickness and oxide layer thicknesses displayed some non-physical behaviour, probably as a result of the modelling software trying to find the best fit. We instead considered the total overlayer thickness, supplemented the AFM measured roughness, and estimated the oxide layer thickness to be around 1.9 nm after 2 weeks, and 2.2 nm after 4 weeks. This result suggest a much faster oxide layer growth than what was estimated for the substrate sample, but since the AFM results for the substrate samples were not used as input for the VASE measurements, the results may not be comparable.

All the estimates for oxide layer thickness in this thesis are calculated using a very simple interpretation of the oxide layer and EMA layer. The CompleteEASE modelling software has difficulty separating the effect of roughness and oxide, making the VASE measurements very dependent on complementary information from other characterization methods when the roughness is low or the oxide layer is thin. The information from the AFM measurements for the substrate sample were inconsistent and unreliable, which in turn made it difficult to estimate the oxide layer thickness based on the results from VASE and AFM alone.

Some of the speculation on why there is such a large variation in the AFM surface roughness hinges on whether one can assume that the oxide layer grows uniformly, and therefore does not affect the surface roughness. For the substrate sample, the variation in surface roughness was large and unsystematic, and and the measurements seemed to be very sensitive to the drift. This could be an indication that there were large local variations. Whether these variations originated from a non-uniform oxide layer, or a uniform oxide layer on a non-uniform underlying structure is not known. For the first hour after exposure to air, the surface roughness on the substrate sample increased steadily, presumably along with increasing oxide layer thickness. This supports the assumption that the oxide layer does indeed have an effect on the surface roughness. On the other hand, this increase in surface roughness along with the oxide layer might have been coincidental, and actually just a consequence of the image drift. For the buffer sample, the terrace-like structure was preserved throughout the weeks following exposure to air, supporting the assumption that the oxide layer does not affect the underlying structure, and therefore not the surface roughness. It is perhaps possible that the uniformity of the oxide layer depends on the initial conditions of the sample surface; uniform growth on smooth surfaces, and non-uniform growth on rough surfaces.

The AFM comparison study was stunted by the Cypher instrument probe tip being contaminated, and producing blurred and smoothened images. The buffer sample was not as sensitive to the damage of the tip, and produced a similar surface roughness to the Multimode instrument, although perhaps slightly underestimated. The substrate sample on the other hand was visibly affected by the blunt tip, as illustrated by the blurred image, and the lowered surface roughness. With a non-damaged tip, this study would have produced more informative results.

6.2 Further work

This thesis has taken a few steps towards making a good optical model for intermediate band solar cells, by looking into the manner of which a thermally desorbed GaAs substrate re-oxidises when exposed to air.

The AFM used in this thesis turned to be very unreliable. Since the VASE measurements will benefit greatly from accurate input from AFM on the surface roughness, it could be useful to repeat the re-oxidation experiments. The next time, however, a better AFM instrument should be used, one that is not subject to large and non-systematic drifts. This would yield more accurate and trustworthy results. Using an AFM instrument that does not have such a large user base would also be advantageous, as there would likely be fewer problems with the equipment than what was experienced with the Multimode instrument. It is also an advantage if the user is experienced with AFM. Now that we know what to expect from each of the samples, special care could also be taken to use AFM probe tips and operating modes that are better suited for the surface features on each sample. A less automated AFM setup could give the user more control of i.e. tip-surface interaction, and allow the user to measure tip-sample forces more accurately. As a complementary technique, the optical profilometer does have a lot of unexplored functionality that might prove useful for accurate determination of surface roughness.

A step towards accurately determining the oxide layer thickness at various stages after exposure to air would be to do ARXPS and/or sputtering with XPS. Doing this on both the substrate sample and the buffer sample, and at various locations on the samples, could be a way to determine whether the oxide layer grows uniformly on the surface or not. Accurate determination of the oxide layer thickness would also be valuable input for the VASE modelling.

A more thorough investigation into the effect of air humidity on re-oxidising wafers that are kept in different environments might be useful. That way, one can determine whether the assumption that the wafers will behave the same during the re-oxidation is justified. This is important if one wants to do parallel measurements with different characterization techniques and use results from one technique as input for another, as was done in this thesis.

A more detailed modelling of the VASE measurements could eliminate some of the modelling weaknesses. For example, limiting layer thicknesses to within a close range of measured values for surface roughness and oxide layer thickness from other techniques would provide a more accurate model, instead of just the ”best fit” model. This again depends on having reliable information from the other characterization techniques. As mentioned, and as shown in Appendix B, using the built-in roughness function produces the same MSE as when using the EMA layer to model the roughness, but it produces different thicknesses for the underlying layer. An investigation into how the built-in roughness function works, and into whether it is more suitable to use the EMA layer or the roughness function should be done.

It could also be interesting to do the same investigations as we have done on the buffer and substrate samples on an epi-ready wafer that has not undergone any thermal treatment. This would give insight into the starting point of the experiment, and perhaps provide useful information on whether the wafers need to be treated before being used in i.e a solar cell.

References

[1] W. Shockley and H.J. Queisser. "Detailed balance limit of efficiency of p-n junction solar cells". In: *Journal of Applied Physics* 32.3 (1961), pp. 510–519.

[2] S. Rühle. "Tabulated values of the Shockley-Queisser limit for single junction solar cells". In: *Solar Energy* 130 (2016), pp. 139–147.

[3] G. Conibeer. "Third-generation photovoltaics". In: *Materials Today* 10.11 (2007), pp. 42–50.

[4] A. Luque and A. Martí. "Increasing the efficiency of ideal solar cells by photon induced transitions at intermediate levels". In: *Physical Review Letters* 78.26 (1997), pp. 5014–5017.

[5] A. Martí et al. "Novel semiconductor solar cell structures: The quantum dot intermediate band solar cell". In: *Thin Solid Films* 511-512 (2006), pp. 638–644.

[6] M. B. Drøyli. "Spectroscopic Ellipsometry of InAs/(Al)GaAs Quantum Dots for Intermediate Band Solar Cells". MA thesis. Norwegian University of Science and Technology, 2017.

[7] A. Holst-Dyrnes. *Surface characterization of GaAs substrates*. Project report. 2017.

[8] P. Eaton and P. West. *Atomic Force Microscopy*. Oxford University Press, 2010.

[9] PSIA. *XE-100 High accuracy small sample SPM. User's Manual*. PSIA Corporation. 2002.

[10] Z.-H. Xu et al. "Drift and spatial distortion elimination in atomic force microscopy images by the digital image correlation technique". In: *Journal of Strain Analysis for Engineering Design* 43 (Aug. 2008), pp. 729–743.

[11] H.-Y. Nie, M. J. Walzak, and N. S. McIntyre. "Use of biaxially oriented polypropylene film for evaluating and cleaning contaminated atomic force microscopy probe tips: An application to blind tip reconstruction". In: *Review of Scientific Instruments* 73.11 (2002), pp. 3831–3836.

[12] P. Markiewicz and M. C. Goh. "Atomic force microscope tip deconvolution using calibration arrays". In: *Review of Scientific Instruments* 66.5 (1995), pp. 3186–3190.

[13] F. Golek et al. "AFM image artefacts". In: *Applied Surface Science* 304 (2014). Selected Papers from the 6th International Workshop on Surface Physics, Functional Materials, pp. 11–19.

[14] *E-mail exchange with Jörg Werner, service engineer at Bruker Nano Surfaces Division*. Apr. 2018.

[15] *A practical guide to SPM*. Veeco Instruments Inc. 2005.

[16] F. Marinello et al. “Error Sources in Atomic Force Microscopy for Dimensional Measurements: Taxonomy and Modeling”. In: *Journal of Manufacturing Science and Engineering* 132 (2010).

[17] *Guide to using WVASE32*. J.A. Woollam Co., Inc. 2011.

[18] *CompleteEASE Data Analysis Manual*. J.A. Woollam Co., Inc. 2011.

[19] D. Brune et al. *Surface Characterization. A user’s sourcebook*. WILEY-VHC, 1997, pp. 291–295.

[20] J.F. Watts and J. Wolstenholme. *An Introduction to Surface Analysis by XPS and AES*. John Wiley & Sons, Ltd., 2003, pp. 82–86.

[21] S. Tanuma, C.J. Powell, and D.R. Penn. “Calculations of electron inelastic mean free paths. III. Data for 15 inorganic compounds over the 50-2000 eV range”. In: *Surface and Interface Analysis* 17.13 (1991), pp. 927–939.

[22] “Chapter 2.5 - X-Ray Photoelectron Spectroscopy”. In: *Handbook of Clay Science*. Ed. by Faïza Bergaya and Gerhard Lagaly. Vol. 5. Developments in Clay Science. Elsevier, 2013, pp. 161–176.

[23] Feng Liu et al. “Characterization study of native oxides on GaAs(100) surface by XPS”. In: *Proceedings of SPIE* 8912 (2013).

[24] *Interferometry basics and phase shifting interferometry*. Bruker Corporation. 2016.

[25] P. de Groot. “Phase Shifting Interferometry”. In: *Optical Measurement of Surface Topography*. Springer Berlin Heidelberg, 2011, pp. 167–186.

[26] *Bruker Website*. 2018. URL: `https://www.brukerafmprobes.com/p-3726-scanasyst-air.aspx`.

[27] *Introduction to Bruker’s ScanAsyst and PeakForce Tapping AFM Technology*. Bruker Corporation. 2011.

[28] *Gwyddion.net*. 2018.

[29] *Nanosensors Website*. 2018. URL: `http://www.nanosensors.com/PointProbe-Plus-Non-Contact-Tapping-Mode-High-Resonance-Frequency-afm-tip-PPP-NCH`.

[30] *RC2 spectroscopic ellipsometer hardware manual, vertical sample mount goniometer*. J.A. Woollam. Co., Inc. 2017.

[31] *J.A. Woollam Co., Inc., RC2 ellipsometer*. 2017. URL: `https://www.jawoollam.com/products/rc2-ellipsometer`.

[32] S. Zollner. “Model dielectric functions for native oxides on compound semiconductors”. In: *Applied Physics Letters* 63.18 (1993), pp. 2523–2524.

[33] J.J.D. Lee et al. “Smoothness and cleanliness of the GaAs (100) surface after thermal desorption of the native oxide for the synthesis of high mobility structures using molecular beam epitaxy”. In: *Journal of Crystal Growth* 356 (2012), pp. 46–52.

[34] B.K. Tanner, D.A. Allwood, and N.J. Mason. "Kinetics of native oxide film growth on epiready GaAs". In: *Materials Science and Engineering: B* 80.1 (2001), pp. 99–103.

[35] H. Iwasaki et al. "Effects of Water Vapor and Oxygen Excitation on Oxidation of GaAs, GaP and InSb Surfaces Studied by X-Ray Photoemission Spectroscopy". In: *Japanese Journal of Applied Physics* 18.8 (1979), p. 1525.

[36] H. Fujiwara et al. "Assessment of effective-medium theories in the analysis of nucleation and microscopic surface roughness evolution for semiconductor thin films". In: *Phys. Rev. B* 61 (16 2000), pp. 10832–10844.

Appendix **A**

AFM image processing

Figure A.1 shows AFM images of buffer sample A at different steps of image processing in Gwyddion. The image is 1 µm x 1 µm in size, and has been processed using image operations 1, 2, and 3 described in Section 3.4. All 1 µm x 1 µm scans in this thesis were processed using these three operations.

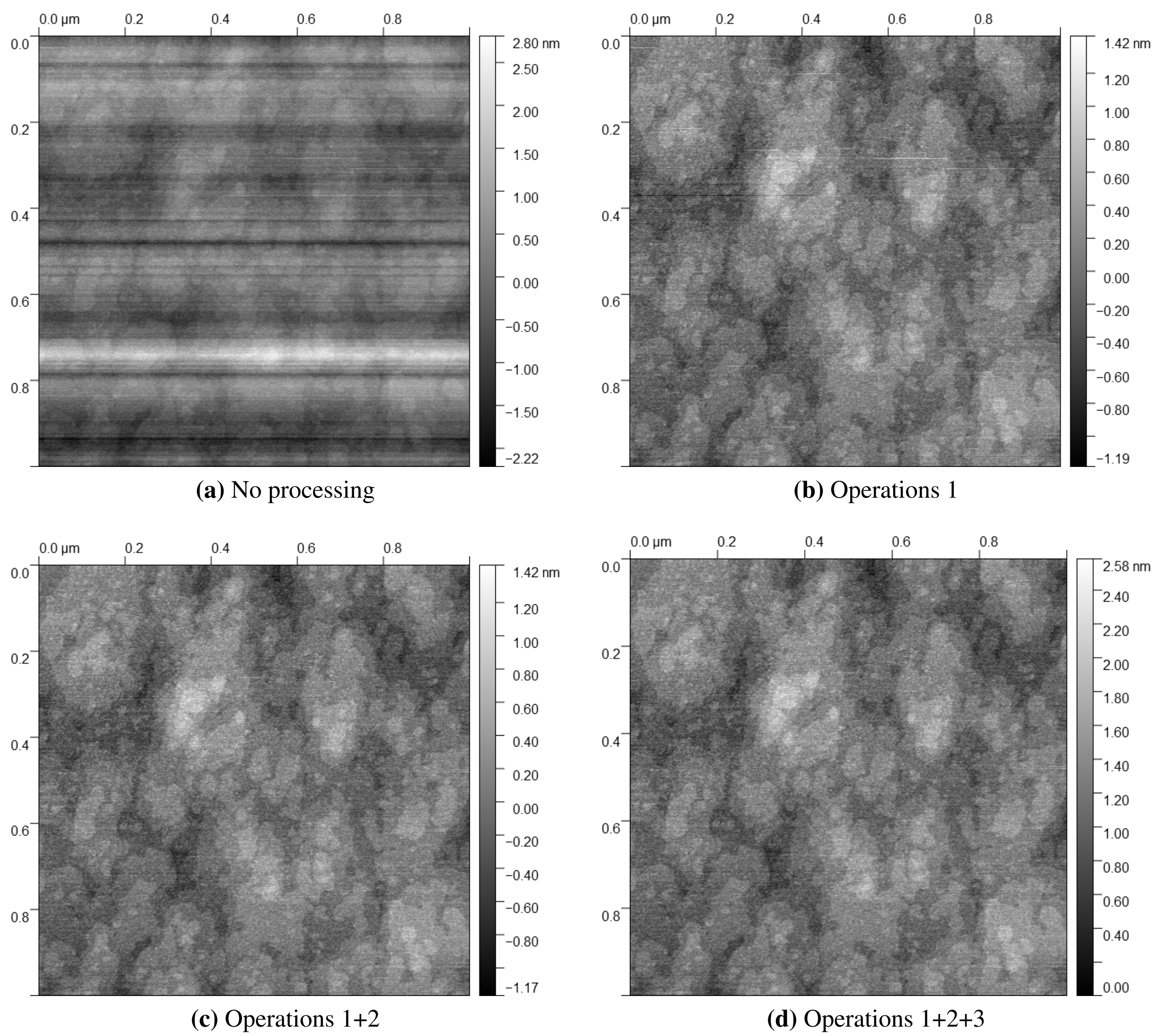

(a) No processing

(b) Operations 1

(c) Operations 1+2

(d) Operations 1+2+3

Figure A.1: 1 µm x 1 µm AFM images of buffer sample A during various stages of image processing as described in section 3.4.

Figure A.2 also shows AFM image scans of buffer sample A, but these scans are 50 µm x 50 µm scans, and require image operation 4 in addition to operations 1, 2, and 3, as there is a noticeable bow in the image that must be removed.

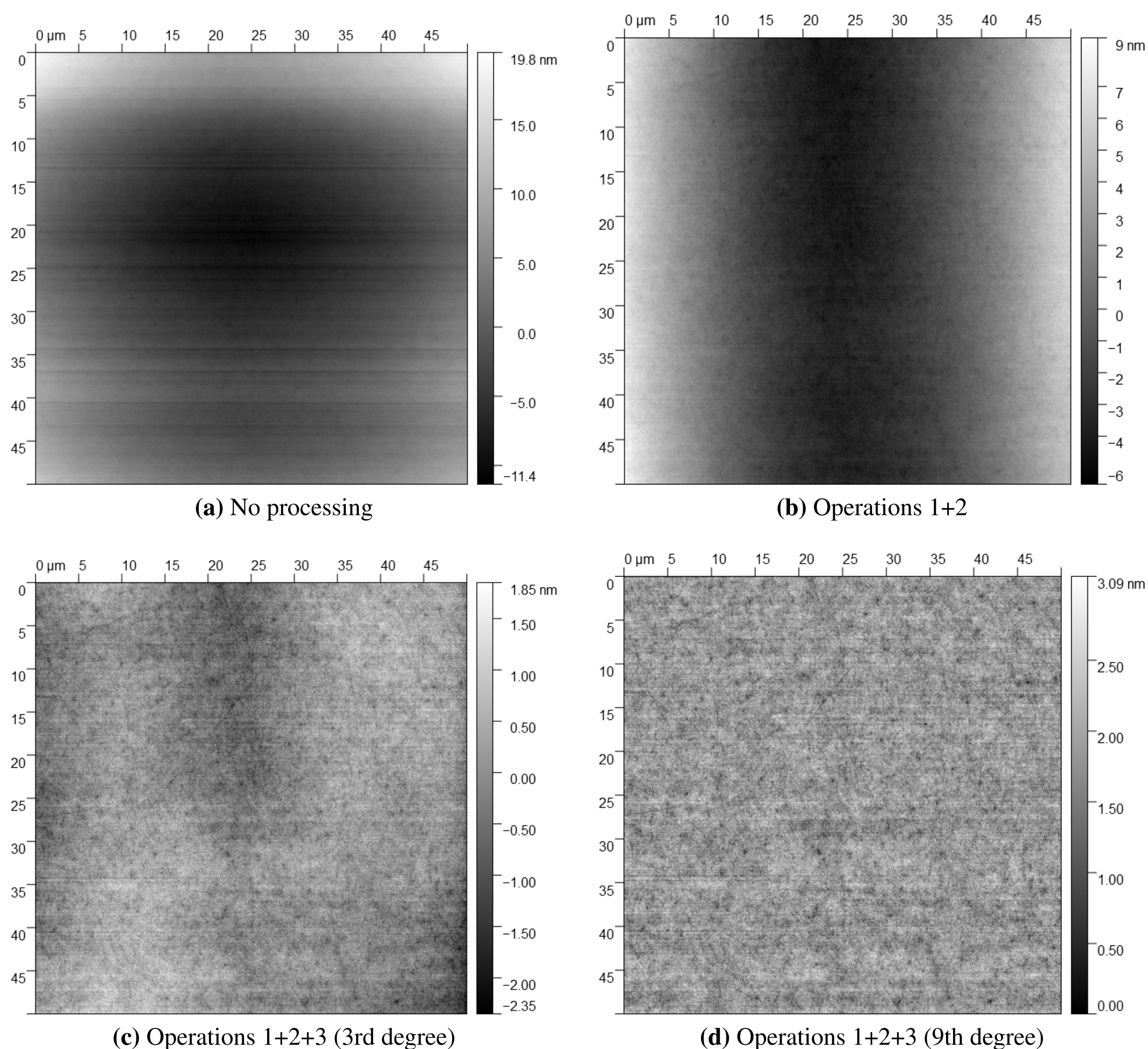

(a) No processing

(b) Operations 1+2

(c) Operations 1+2+3 (3rd degree)

(d) Operations 1+2+3 (9th degree)

Figure A.2: 50 µm x 50 µm AFM images of buffer sample A during various stages of image processing as described in section 3.4. (a) Unprocessed image. (b) Operations 1 and 2 have been applied. (c) Operation 4 has been applied with a 3rd degree horizontal polynomial background removed. (d) Operation 4 has been applied with a 9th degree horizontal and vertical polynomial background removed.

Appendix B

VASE modelling

Below is a list of the attempted models for the ellipsometry measurements. As various models might fit better at various stages of the re-oxidation, the measurements were divided into intervals of time, and the models were fitted to the data. Table B.1 and Table B.2 show the MSE for the various models applied to various time intervals for the two samples.

1. **Model 1:** GaAs substrate with an EMA overlayer composed of 50% GaAs and 50% void
2. **Model 2:** GaAs substrate with an EMA overlayer composed of 50% GaAs oxide and 50% void
3. **Model 3:** GaAs substrate with an EMA overlayer composed of 34% GaAs, 33% GaAs oxide, and 33% void.
4. **Model 4:** GaAs substrate with an EMA overlayer with various percentages for GaAs, GaAs oxide and void. Best model found was 50% GaAs, 10% GaAs oxide, and 40% void
5. **Model 5:** GaAs substrate with a GaAs oxide overlayer and the built-in roughness function turned on
6. **Model 6:** GaAs substrate with a GaAs oxide overlayer and an EMA layer on top of that consisting of 50% GaAs oxide and 50% void.
7. **Model 7:** GaAs substrate with a GaAs oxide overlayer

Table B.1: MSE for the various models at each time interval for the substrate sample, modelled for all angles of incidence. Not all the models were applied to all the time intervals, these fields are left blank.

	Substrate sample			
	1-10 min	10-20 min	30-90 min	1-12 weeks
Model 1	2.471	2.554	2.630	4.456
Model 2	4.569	4.702	4.843	4.828
Model 3	3.542	3.682	3.896	7.436
Model 4	2.783	2.923		
Model 5	3.580	3.705	3.804	4.253
Model 6		3.705	3.804	4.253
Model 7		3.705	3.804	4.912

Table B.2: MSE for the various models at each time interval for the buffer sample, modelled for all angles of incidence. Not all the models were applied to this sample, as shown by the fields left blank.

	Buffer sample			
	3-10 min	10-20 min	30-90 min	26 hours -4 weeks
Model 1	2.737	2.846	3.022	4.127
Model 2	2.555	2.514	2.421	2.711
Model 3	3.502	3.782	4.045	5.946
Model 4				
Model 5	1.966	1.999	2.015	2.236
Model 6	1.966	1.999	2.015	2.236
Model 7	1.970	2.018	2.067	2.731

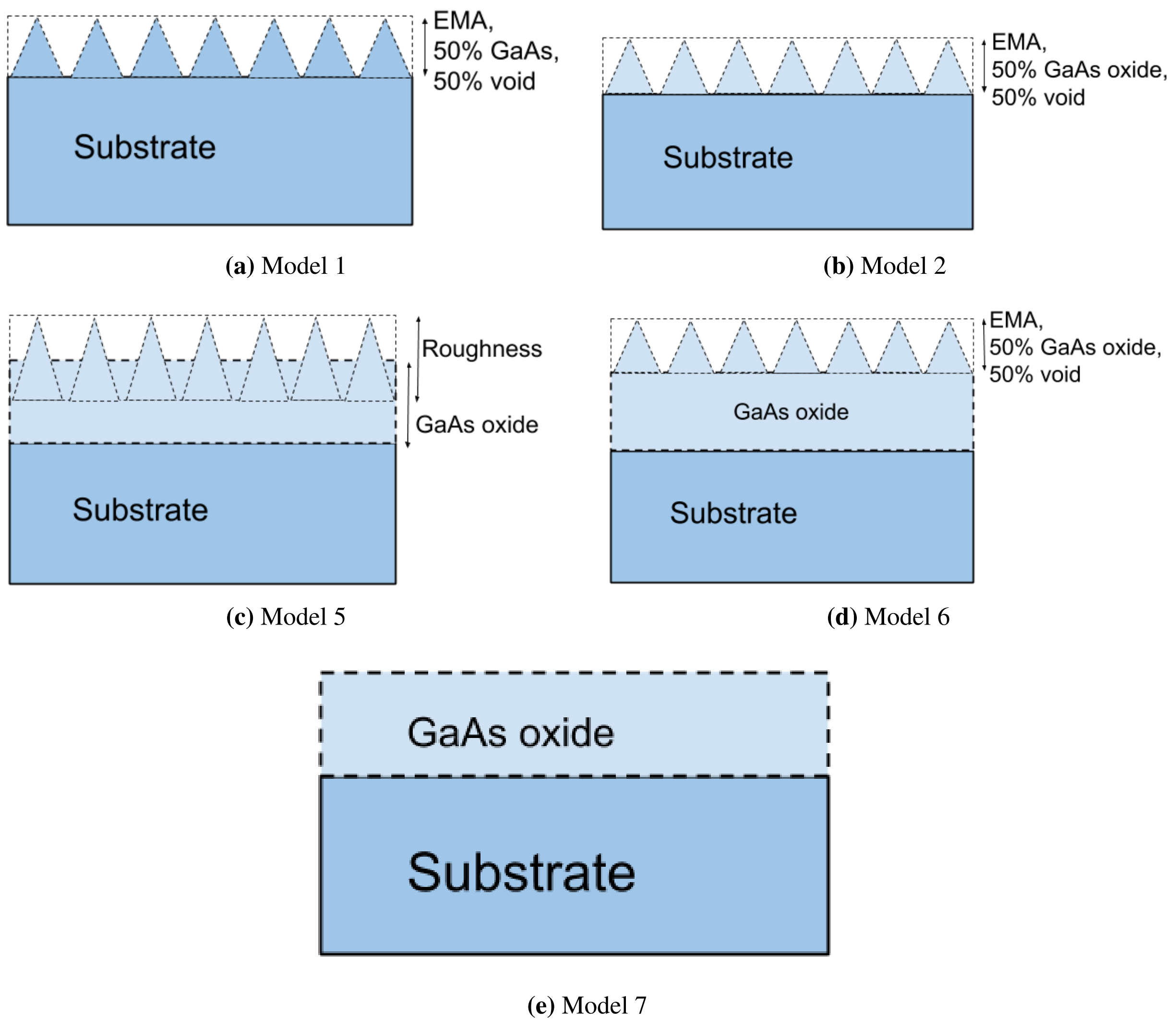

(a) Model 1

(b) Model 2

(c) Model 5

(d) Model 6

(e) Model 7

Figure B.1: Illustrations of Models 1, 2, 5, 6, and 7. Models 3 and 4 are not illustrated here.

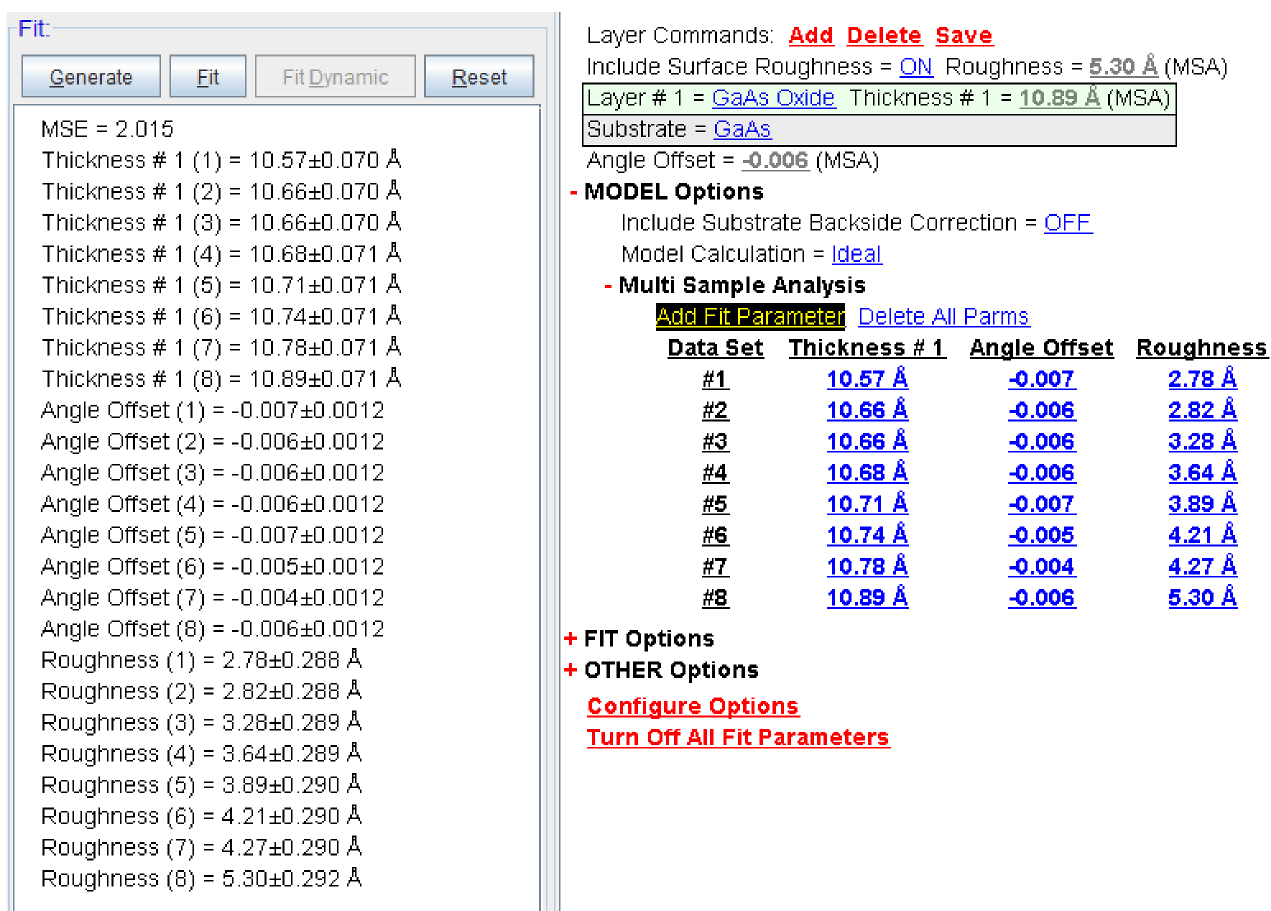

Figure B.2: Screenshot from VASE software CompleteEASE. A model of GaAs, GaAs oxide, and the built-in roughness function turned on has been constructed. Image shows MSE for the model, layer thickness for the GaAs oxide, and values for surface roughness. Comparing this image to Figure B.3, we see that the GaAs oxide layer thickness is higher for this model with the built-in roughness function turned on than it is for the model with EMA layer, even though the values for the built-in roughness and the EMA layer are the same.

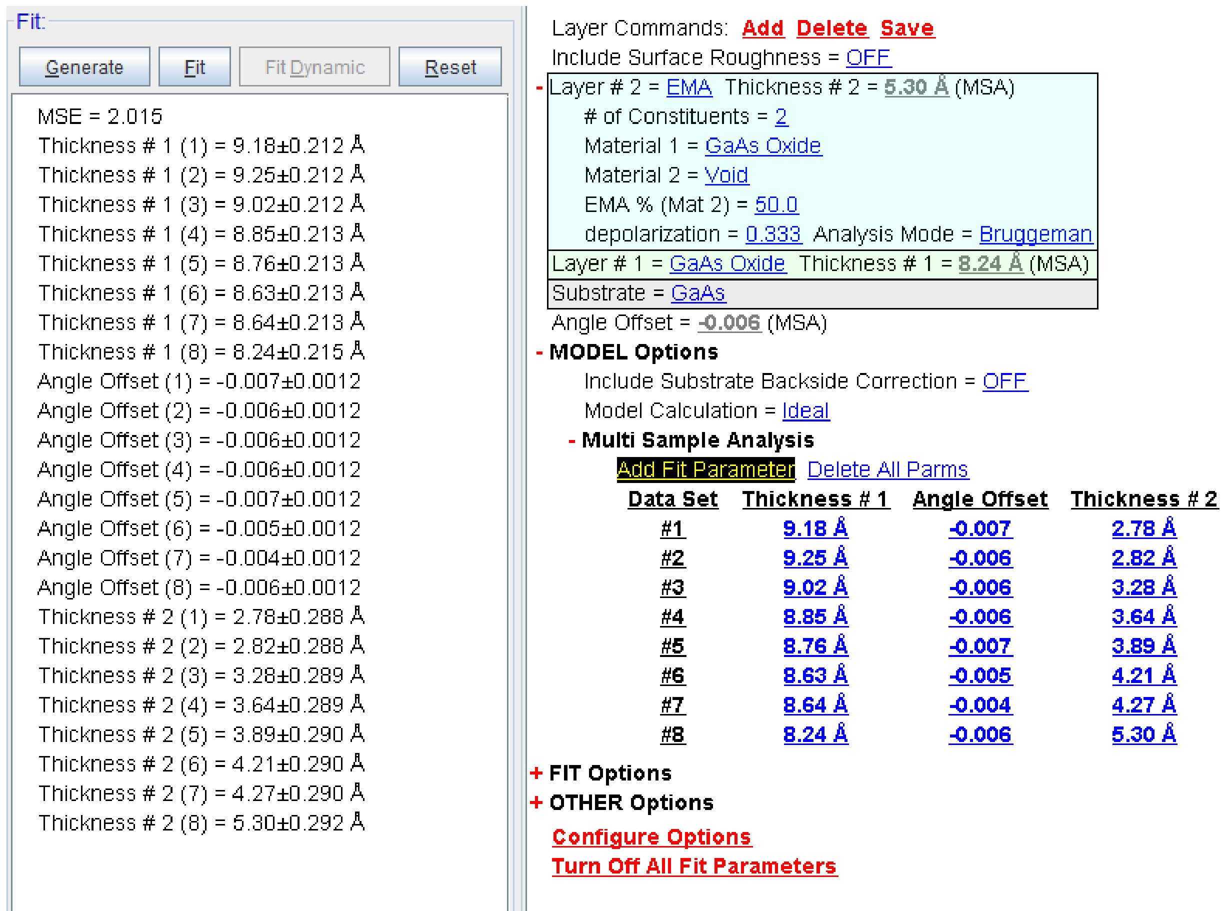

Figure B.3: Screenshot from VASE software CompleteEASE. A model of GaAs, GaAs oxide, and an EMA layer of 50% GaAs oxide and 50% void to simulate the roughness has been constructed. Image shows MSE for the model, layer thickness for the GaAs oxide and EMA layer that simulates the roughness. Comparing this image to Figure B.2, we see that the GaAs oxide layer thickness is lower for this model with EMA than it is for the model with the built-in roughness, even though the values for the built-in roughness and the EMA layer are the same.